UNIVERSITY OF MESSINA

Department of Chemical, Biological, Pharmaceutical and Environmental Science

PhD Course in Advanced Catalytic Processes for using Renewable Energy Sources (ACCESS)

XXXVI CYCLE

S.S.D. FIS/01

Boosting photo(electro)catalytic reactions: solvent organization and electrode design

PhD Thesis of:

Rosaria Verduci

Coordinator: Supervisor:

Prof. Gabriele Centi   **Prof. Giovanna D'Angelo**

Co-Supervisor:

Prof. José Ramón Galán-Mascarós

Academic Year 2022-2023

INDEX

General introduction

In the last decades, the rapid growth of global population and the industrialization have led to an ever-increasing consumption of energy. Currently, our energy infrastructure is still predominantly based on fossil fuels, including coal, petroleum, natural gas and uranium. However the reserves of fossil fuels are finite (*i.e.,* they are exhaustible and not renewable) and therefore they are not sufficient to meet the long-term energy world demand. Moreover, the depletion of fossil fuels results in the increase of their extraction and transportation costs which in turn has negative impacts in several sectors of everyday life (economical, social and political). Most importantly, the widespread utilization of fossil fuels releases greenhouse gases, especially carbon dioxide (CO_2), in the atmosphere. As a result, the human population is facing detrimental environmental issues including global warming, climatic change and environmental pollution. Thus the transition to an energy system based on sustainable and renewable sources is one of the biggest challenge for the development of a green energy future. Among the renewable energy sources, solar energy with an energy potential of 23000 TWy per year is the main environmental friendly energy source able to meet the current and future energy demands[1]. However, sunlight has a variable and intermittent nature[2]. Consequently, in addition to photovoltaic (PV) devices that transform solar energy into electricity, various methods, including photocatalytic (PC), photoelectrochemical (PEC), and integrated photovoltaic-electrochemical (PV/EC) systems, have been developed to enhance the utilization of solar energy. [3] These approaches aim to produce solar fuels and high-value added chemicals by directly harnessing sunlight, thus offering promising solutions to produce clean energy, reduce our dependence on fossil fuels, and mitigate the climate change.

It is within this general context, that this thesis deals with two different projects tackled during my PhD program. The goal of both projects is to shed light on the specific aspects involved into the improvement of the performances of two distinct energy-related processes, *i.e.,* the hydrogen production from water and the ethanol oxidation reaction (EOR).

Namely, the first project is a combined theoretical and experimental research work and is related to the hydrogen production process by photocatalytic water splitting. Concerning this topic, most of the studies reported in literature are focused on the development of strategies for controlling the photocatalyst's properties in order to obtain the best performing material.

By contrast, limited attention was given to the role of the reaction medium. The main result of this project is that water can not be simply considered a passive medium, but rather the water molecules, acting as proton donor or acceptor, can boost the reaction itself. In particular, it is investigated how the structure of water at the water-semiconductor interface influences the rate of water-splitting. This first part of this PhD thesis is divided in two chapters. Chapter 1 focuses on the experimental study, specifically we have:

1. Synthetized two photocatalysts (an undoped TiO_2 and a B-doped TiO_2) exhibiting a different rate of H_2 production, but no significant differences in the physical chemical properties.
2. Demonstrated, by performing Fourier Transform Infrared (FTIR) spectroscopic measurements under controlled relative humidity (RH) conditions, that the main responsible of the different photocatalytic activity is the structure of the interfacial water.

These experimental activities were carried out in Laboratory of Catalysis for Sustainable Production and Energy (CASPE/INSTM) of the Department Chemical, Biological, Pharmaceutical and Environmental Science (ChiBioFarAm) and in the Optical Spectroscopic Laboratory of the Department of Mathematical and Computer Sciences, Physical Sciences and Earth Sciences (MIFT) of the University of Messina.

Chapter 2 deals with the computational results. Indeed, density functional theory molecular dynamic (DFT-MD) simulations were performed in order to better understand how the structural organization of water at the interface with a photocatalyst determines the water splitting performances. To the best of our knowledge, in most of the computational literature published works concerning the water splitting on TiO_2, the water is at the best represented as an implicit solvent or using just a single layer of explicit water molecules. In our work, the innovative element that allows to give a more realistic description of the interaction of water with the TiO_2 surface is the consideration of an entire liquid water slab (132 water molecules) in direct contact with the photocatalyst, *i.e.,* an explicit solvent scheme.

This computational study was conducted in collaboration with Dr. Fabrizio Marco Creazzo (Department of Chemistry, University of Zürich, Zürich, Switzerland) and Dr. Giuseppe Cassone (Institute for Chemical-Physical Processes, National Research Council of Italy (IPCF-CNR), Messina, Italy).

The second research project was developed during my abroad research period at the Institut Català d'Investigació Quimìca (ICIQ, Tarragona, Spain) under the supervision of Professor José Ramón Galán-Mascarós in the framework of the European Project DECADE (DistributEd Chemicals And fuels production from CO_2 in photoelectrocatalytic DEvices). With respect to the previous project, this one is more applicative and relies on the design, fabrication and testing of an highly performing and stable electrocatalyst for realizing the ethanol oxidation reaction (EOR) under extreme conditions (concentrated ethanol 96%). The final goal is to use this catalyst in a new kind of PEC cell that provides an effective way to harness the solar energy for catalyzing the CO_2 reduction and the EOR on the cathodic and anodic sides respectively, to selectively produce the same product (*i.e.,* ethyl acetate).

PROJECT 1

EXPERIMENTAL RESULTS

Structuring of water at the TiO₂ interface boosts solar-driven water splitting performances

Summary

This chapter deals with the experimental results of the first project developed during my PhD program. The focus is on the critical role that the solvent (*i.e.,* water) plays in determining the water splitting performances, a topic that is often overlooked in literature. It is emphasized how water cannot be considered a passive medium where the reaction occurs, but it has an active role in catalysing the reaction itself. Indeed, the water structure at the interface with a solid surface deeply influences the electron transfer and thus the reaction rate.

1.1 <u>Introduction</u>

Photocatalytic water splitting is a promising method to produce green hydrogen (H_2) using directly solar energy[3], but several technological improvements are still required to enhance the performance of this process and make it competitive on a large scale. In principle, the solar-to-hydrogen (STH) conversion efficiency of this reaction depends on three main factors: [4-6] i) the light-harvesting ability of a semiconductor, ii) the charge separation/transfer efficiency, and iii) the surface reactions for the H_2 and O_2 generation.

Since the pioneering activities of Fujishima and Honda[7], titanium dioxide (TiO_2), also known as titania, is still a favourite semiconductor for H_2 production due to its availability, non-toxicity, high chemical stability and low cost[8, 9]. However, two factors are responsible for the unsatisfactory performance of titania: i) the activation under ultraviolet light, which accounts for a minor fraction of solar spectrum (about 4% of the sunlight) due its large bandgap (3.2 eV for the anatase phase) [10] and ii) the fast recombination of the photogenerated charge carriers involved in the reaction[11]. Thus, several strategies including doping[12, 13], control of the nanomorphology[14] or the formation of heterojunctions[15, 16] have been proposed to overcome the aforementioned issues and develop a suitable photocatalyst for hydrogen and oxygen evolution reactions (HER and OER, respectively). In this context, doping with a non metallic element (cheaper and more stable during photocatalytic processes than metallic elements) is one of the most feasible pathway to boost the photocatalytic activity of TiO_2. [17] Among all the non metallic elements, recently boron emerged as one of the most promising. [18, 19] However a mechanistic comprehension of the role of boron as dopant and of its concentration in the improvement of the photocatalytic behaviour of TiO_2 is still lacking. For example, Zhao et al. [20] observed a red shift in the band edge of TiO_2 after boron doping while a blue shift is reported by Chen et al. [21]. In other works, Zaleska et al. [22], Niu et al. [23] and Feng et al. [24] found that TiO_2 exhibits the highest photoactivity after boron doping with different loading (2%, 6% and 10%, respectively). Moreover, these results are often achieved in presence of a sacrificial agent (such as ethanol or methanol in aqueous solution). [24] In addition, the slow kinetics of the OER, which involves the transfer of four electrons[6], hampers the overall efficiency of water splitting. In this regard, surface engineering of semiconductors through the incorporation of co-catalysts (metal nanoparticles), has emerged as a promising approach to enhance photocatalytic activity[25]. Indeed, the inclusion of

appropriate co-catalysts improves electrochemical parameters, such as the exchange-current density and the charge/electron transfer coefficient[6]. More specifically, the electron transfer processes can occur via inner-sphere or outer-sphere mechanism[26, 27]. In the former mechanism, water molecules are strongly chemisorbed on the catalyst surface forming direct chemical bonds[26, 27]. In the second mechanism, the aqueous ions retain their hydration shell of coordinated water molecules and interact with the catalysts surface trough weak electrostatic forces[26, 27]. In agreement with the Marcus-Hush theory, the reorganization of water molecules plays a critical role in determining the electron transfer rate, in particular in the outer-sphere mechanism that is the initially dominant process[28, 29]. Therefore, gaining a fundamental understanding of how the water structure on semiconductor surfaces influences the reactivity of the water splitting reaction is essential.

In this context, it is worth noting that several experimental[30, 31] and theoretical[32-37] observations indicate that the behaviour and properties of water near a surface are typically different from those of water in its bulk state. Specifically, water molecules are more ordered and less mobile in close proximity to a solid surface (within 10 Å) than in the bulk region. Simultaneously, the dielectric constant of interfacial water is 10 times lower than its value in the bulk ($\varepsilon \sim 80$) [38, 39]. Most importantly, the structure of the interfacial water and thus the water splitting behaviour are strongly affected by the geometric constraints of the solid surface.

However, the direct understanding of the interfacial water organization is not trivial because many experimental methods are bulk sensitive techniques[40]. Consequently, the signal arising from the interface is overshadowed by the signal originating from the bulk water. Thus, it is not surprising that determining the peculiar linkage between the different surface features and the observed change in the water-splitting activity is still elusive. In this thesis, we endeavour to examine whether the water's structure at the water-semiconductor interface differs from that found in the electric double layer (EDL) and bulk electrolytes and ascertain its potential impact on the kinetics of water splitting. To answer to this challenging question, we synthetized two TiO_2 anatase photocatalysts (without and with small amounts of boron (B)) that exhibit different water-splitting activities. It is mandatory to emphasize that the aim of the project is not the synthesis of the best performing photocatalyst but the investigation of the influence of the structural organization of water at the interface with TiO_2 in the water splitting activity. For these reasons, in this project: i) we avoided the addition of noble metal

nanoparticles as cocatalyst, ii) the concentration of B was intentionally chosen low (1%) in order to avoid structural modifications responsible of an enhanced water splitting behaviour and iii) the photocatalytic tests were performed in pure distilled water at neutral pH. Interestingly, the different photocatalytic activity does not rely upon significant differences in the physical-chemical properties of the photocatalysts itself or in the charge carrier separation and recombination, but on a measurably diverse hydrogen (H)-bond network of water molecules at the investigated interfacial surfaces. Specifically, the presence of B atoms at the surface leads to a change of the local electric field, which affects the structure of the interfacial water layer[41-44]. The changes in the water structure have been experimentally demonstrated by Fourier Transform Infrared (FTIR) measurements at different controlled relative humidity (RH) conditions. Indeed, probing the OH stretching vibrations yields information about the H-bond network and thus on the water organization[45]. At the same time, low RH values, *i.e.,* low water content, provide insights into the interfacial water[46]. While, a bulk-like water behaviour is observed for high RH conditions[46].

1.2 Results and Discussion

1.2.1 Water splitting photobehaviour

The amount of H_2 released during the water splitting reaction was measured in order to assess the activity of the undoped and B-doped TiO_2 powders. **Figure 1a** shows the cumulative H_2 production (in micromoles per gram of catalyst) as a function of the irradiation time (about 2 h) for both TiO_2 and B- TiO_2 samples. There is an initial induction time related to the establishment of an equilibrium condition inside the photoreactor. Later, the formation of H_2 displays a linear dependence on the irradiation time, evidencing the absence of photocatalysts deactivation effects during the experiments. It is worth remarking that the amount of photoproduced H_2 and O_2 is in agreement with the expected stoichiometric ratio of 2:1, due solely to the water splitting process.

As depicted in **Figure 1b**, the doping of TiO_2 with boron atoms enhances the H_2 production rate. Specifically, the B-TiO_2 exhibits a H_2 production rate of 20.1 μmol g^{-1} h^{-1} which is 4.6 times higher than the one of TiO_2 (1.4 μmol g^{-1} h^{-1}).
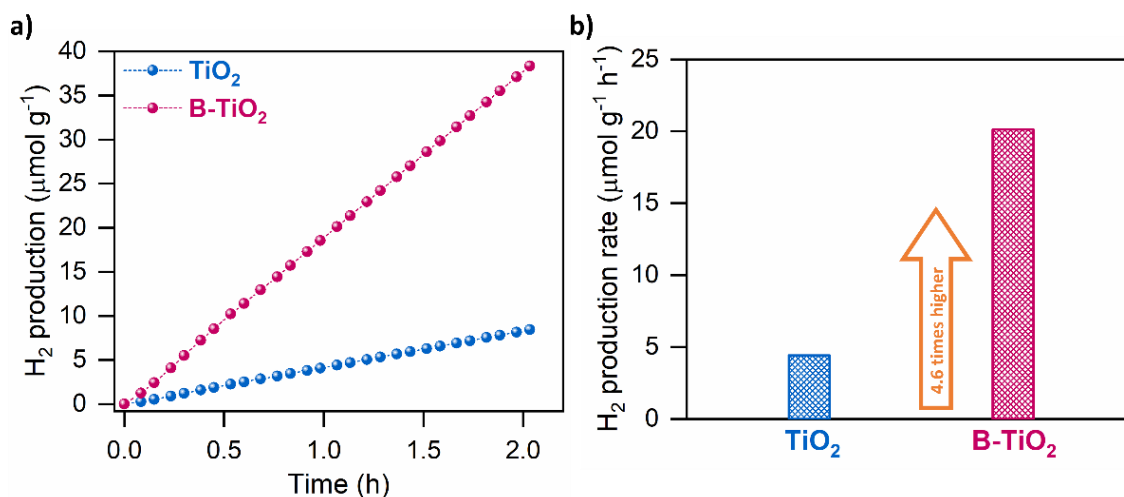
Figure 1| a) Cumulative hydrogen production (in μmol per gram of catalyst) using the synthetized TiO_2 ad B-doped TiO_2 photocatalysts under irradiation for 2 h. **b)** Comparative hydrogen photoproduction rates.

In order to find an explanation of the enhanced photocatalytic behaviour exhibited by the B-TiO_2 photocatalyst, several physicochemical characterizations of both samples have been carried out. The results of UV-vis diffuse reflectance spectroscopy, XRD, Raman, XPS and SEM-EDX analysis rule out that bandgap changes, creation of heterojunctions or heterophases, and alterations in crystal facets, nanomorphology or nanodimensions are responsible of the improved ability towards water splitting of B-TiO_2. Moreover, additional investigations including photoelectrochemical and steady-state PL studies, were conducted on both photocatalysts to exclude that other effects such as an improved charge separation and stabilization or the creation of intermediate states are responsible of the boosted photocatalytic activity of B-TiO_2. These aspects and related results will be discussed in the next paragraphs.

1.2.2 Physical-chemical characterization

1.2.2.1 UV-vis diffuse reflectance spectroscopy

The optical absorption properties of the photocatalysts were investigate by Uv-vis Diffuse Reflectance spectroscopy. **Figure 2** shows the Uv-vis absorption spectra of undoped and B-doped TiO_2.
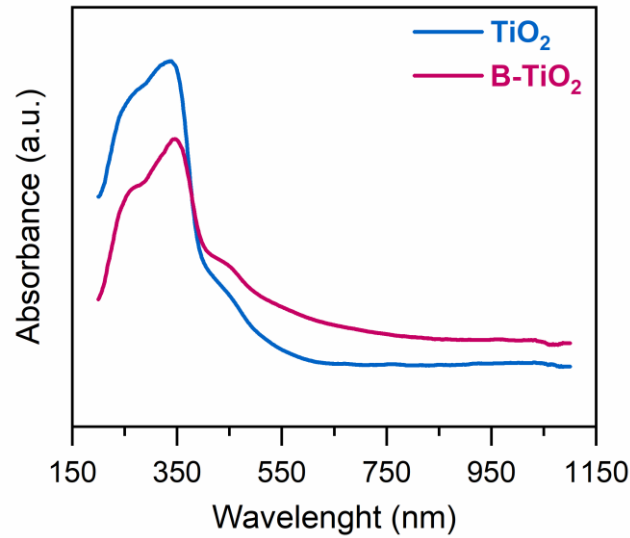
Figure 2| UV-visible diffuse reflectance spectra of TiO$_2$ and B)-TiO$_2$ samples.

Both samples display a similar absorption band profile with an intense peak in the wavelength range between 300 and 380 nm associated with the O^{2-} → Ti^{4+} electronic transitions. The main peak at about 370 nm (3.35 eV) and the shoulder at around 400 nm (3.1 eV) are ascribed to a predominant anatase and a minor rutile TiO$_2$ phases[47], respectively. It is worth nothing that the doping of TiO$_2$ with B atoms does not significantly change the relative amount of rutile phase. The UV-vis diffuse reflectance analysis indicates that the absorption behaviour of titania is not affected by B incorporation, ruling out the possibility that B doping improves visible light absorption and, consequently, the activity of TiO$_2$. Indeed, probably due to the low content of B doping, the B-doped TiO$_2$ sample does not exhibit a red shift in the absorption edge (typically, induced by the creation of gap states close to the bottom of the conduction band when B atoms replace O ones) [48].

A slight increase in the long tail in the visible region can be observed for B-TiO$_2$ compared to TiO$_2$ due to the very low formation of defect states. [49] Note, however, that the light absorption above around 2eV is nearly zero. By contrast, when a significant amount of oxygen defects and Ti^{3+} ions would be present (in oxygen-deficient anatase TiO$_2$), an increase of the absorption to the infrared region starting from ~620 nm (~2 eV) is expected[50]. The energy bandgap of the TiO$_2$-based materials was determined from the diffuse reflectance spectra using the Tauc's plot method (**Figures 3a,b**) [48].
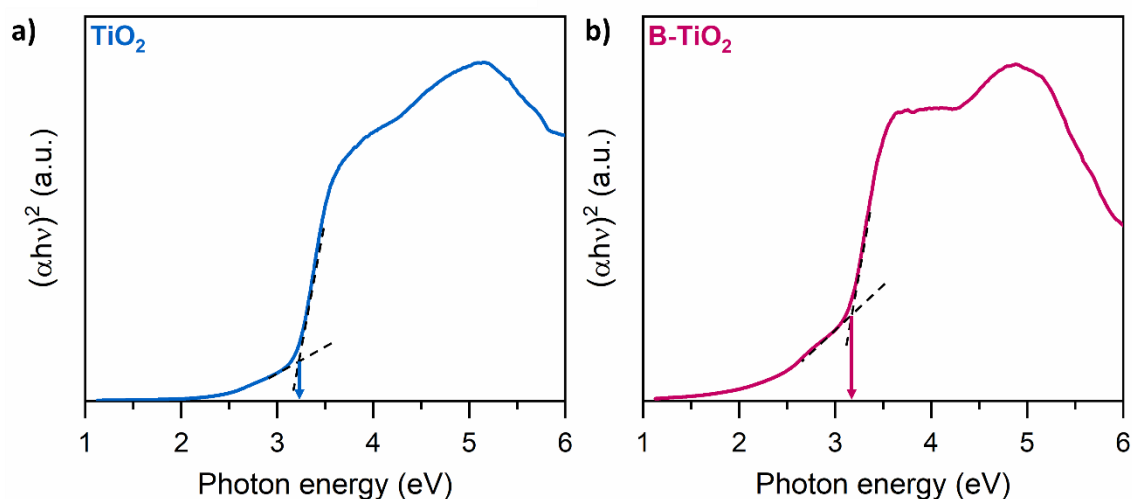
Figure 3| Tauc plot of **a)** TiO$_2$ powder and **b)** B-TiO$_2$ powder.

Both the TiO$_2$-based photocatalysts have an E$_g$ of ~3.2, with only minor differences that cannot be related to the significant improved photocatalytic behaviour of the B-TiO$_2$ catalyst.

1.2.2.2 <u>X-ray diffraction</u>

The crystalline structure of the undoped and B-doped TiO$_2$ was investigated through x-ray diffraction (XRD) analysis. The X-ray diffraction (XRD) patterns (**Figure 4**) suggest that both powders exhibit only characteristic peaks associated with the anatase phase (according to JCPDS card no. 21-1272). No crystalline rutile or brookite phases were detected indicating the high purity of the synthetized samples. Thus, there is evidence of the alteration of the preferentially exposed crystalline facets eventually induced by doping with B atoms, as also confirmed by micro-Raman spectroscopy (see **Section 1.2.2.3**) and scanning electron microscopy (see **Section 1.2.2.5**). Specifically, the peak with the highest intensity is associated to the reflection (110) located at 2θ=25.28°, other important signals are present at 37.8°, 48.05°, 53.89°, 55.06° and 62.69°. Remarkably, in the XRD spectrum of the B-TiO$_2$ sample, the minor shift of the main diffraction peak (2θ = 25.3°) to a lower angle (inset of **Figure 4**) indicates the expansion of the TiO$_2$ crystal lattice due to the incorporation of B atoms into interstitial sites[19, 51, 52].
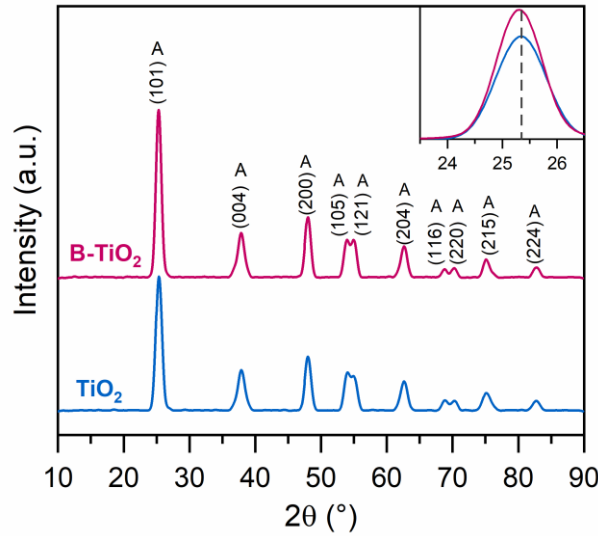
Figure 4| XRD pattern undoped and B-doped TiO$_2$ powders.

We can observe that in the XRD pattern of the B-doped TiO$_2$ there is no trace of an additional at 2θ=28.1° corresponding to boron oxide (B$_2$O$_3$, possibly coming from thermal decomposition at ~150 °C of boric acid) [18] surface nanoparticles, which could have an impact on the photocatalytic behaviour, as confirmed by micro-Raman spectroscopic results.

1.2.2.3 <u>Micro-Raman spectroscopy</u>

The structural properties of the undoped and B-doped TiO$_2$ were further examined by micro-Raman spectroscopic measurements. The spectra of TiO$_2$ and B-TiO$_2$ (**Figure 5**) show five peaks associated to E$_g$ (144cm^{-1}), E$_g$ (197 cm^{-1}), B$_{1g}$ (399 cm^{-1}), A$_{1g}$+B$_{1g}$ (516 cm^{-1}) and E$_g$ (639 cm^{-1}) Raman modes of the anatase phase, in agreement with the results of he XRD diffraction patterns. These modes are the results of the symmetric stretching (E$_g$), symmetric bending (B$_{1g}$) and antisymmetric bending (A$_{1g}$) vibrations of O-Ti-O bonds in TiO$_2$, respectively.
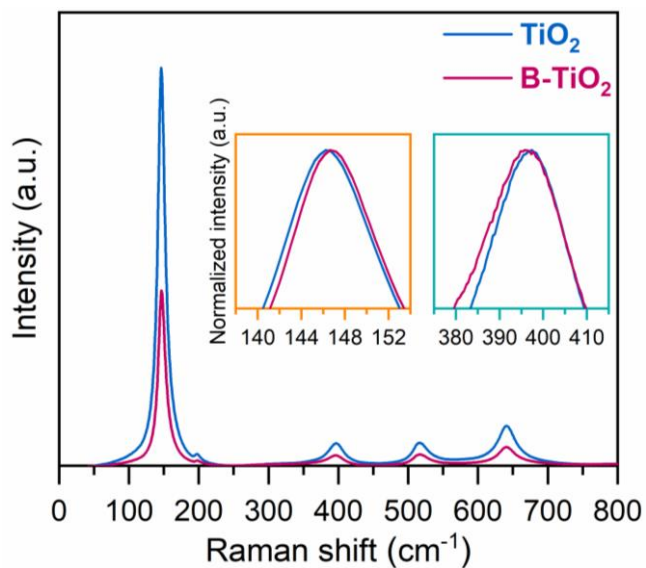
Figure 5| Raman spectra of undoped and B-doped TiO_2 samples.

Moreover, the micro-Raman spectra do not suggest the presence of oxygen vacancies in TiO_2, which should generate two additional Raman modes at 155 and 171 cm$^-$.[50, 53] As shown in the insets of **Figure 5**, the B-doped sample is characterised by a blueshift (~ 0.5 cm^{-1}) of the $E_g(1)$ mode and a redshift (~ 1 cm^{-1}) of the B_{1g}. These Raman modes are due to the Ti-atom vibrations (the system's symmetry does not allow the motion of the O atoms). [54] Thus this result can be related to B in Ti substitutional positions.

1.2.2.4 <u>X-ray photoelectron spectroscopy</u>

The surface composition and the chemical state of each element in the synthetized photocatalysts were examined by X-ray photoelectron spectroscopy (XPS). **Figures 6a-c** reports the XPS spectra of the O 1s, Ti 2p and B 1s peaks for undoped ad B-doped TiO_2, respectively. The corresponding binding energy (BE) values are summarised in **Table 1**.
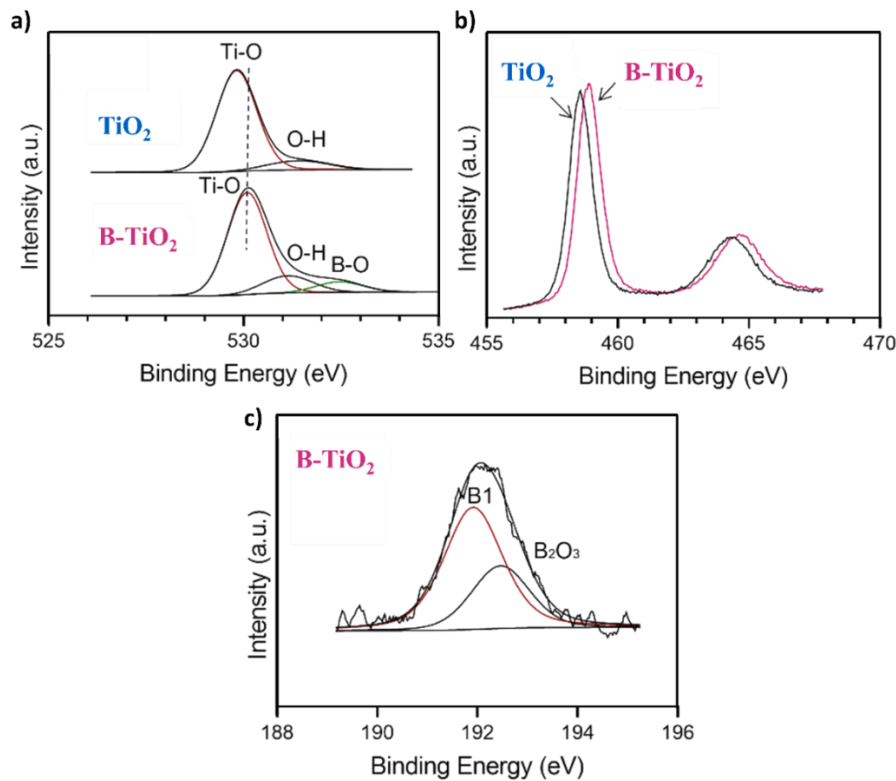
Figure 6| XPS spectra of **a)** O1s, **b)** Ti2p and **c)** B1s regions for both pure TiO_2 and B-TiO_2 samples.

From the top panel in **Figure 6a**, the O1s peak of the TiO_2 sample can be deconvoluted in two components at 529.82 and 531.41 eV (indicated as O 1s (I) and O 1s (II)), corresponding to the lattice oxygen (Ti-O) species and the oxygen of the surface hydroxyl (Ti-OH) group, respectively. In the B-doped TiO_2 (bottom panel in **Figure 6a**), after deconvolution, in addition to the main peak at 530.09 eV related to Ti-O species and the second peak at 531.13 eV attributed to the Ti-OH groups, a third component at 532.46 eV (labelled as O 1s (III)) associated to B-O bonds is present. [18] Thus, this first result is a prove of the presence of B atoms in the doped sample.

The XPS spectrum of the Ti 2p peak for TiO_2 (black line in **Figure 6b**) exhibits the doublet Ti $2p_{3/2}$ at 458.58 eV and Ti $2p_{1/2}$ at 464.12 eV with a splitting energy (*i.e.,* separation of the peaks) of 5.54 eV, which is typical the presence of Ti^{4+} in TiO_2 lattice. [55] For the B-TiO_2 sample (red line in **Figure 6b**), the Ti 2p peaks show a positive shift of 0.27 eV (BE values of 458.85 an 464.39 eV for Ti $2p_{3/2}$ and Ti $2p_{1/2}$, respectively). This displacement is indicative of a reduction of the electron density of Ti 2p after the incorporation of B in the TiO_2 lattice. [56] This is probably due to the presence of B atoms (more electronegative than Ti) in interstitial sites that leads to the electron transfer from Ti to B.

Based on the XPS data, the boron content on the surface of the B-TiO$_2$ sample is 3.6%. Regarding the chemical environment of boron in the B-TiO$_2$ samples, the assignments of XPS peaks is controversial because B atoms can occupy interstitial or substitutional (replacing Ti or O atoms) positions in the TiO$_2$ lattice. The B1s peak (**Figure 6c**) have been deconvoluted into two components. After a comparison with literature data, the main contribution (B 1s (I)) at 191 eV is ascribed to B incorporated into TiO$_2$ lattice in interstitial positions forming Ti-O-B species[24, 52, 57], while the second component (B 1s(II)) at 192.46 eV is assigned to B$_2$O$_3$[52, 58, 59]. DFT studies indicate that the occupation of interstitial sites or O substitution is energetically preferable to substituting Ti with B atoms. [60]

In conclusion, our B-doped TiO$_2$ was successfully synthetized by sol-gel method which generally leads to interstitial B-doping, together with the formation of B$_2$O$_3$ on the surface of the TiO$_2$ particles. [61, 62] Moreover, boron doping introduces a residual charge, which results into an increase in the number of surface OH groups[59, 63] (which is evidenced by the increase of the intensity of the O 1s (II) component of the B-TiO$_2$ sample with respect to TiO$_2$, **Figure 6a**). The XPS results of our samples are thus consistent with the presence of (i) interstitial B sites (signal B 1s (I) in **Figure 6c**, and involving the shift in the BE of Ti 2p in **Figure 6b)** and (ii) surface B (signal B 2 in **Figure 6c**), which generates the B-O signal at 532.46 eV (**Figure 6a**).

	Binding energy (eV)						
	O 1s			**Ti 2p**		**B1s**	
Sample	**O 1s (I)**	**O 1s (II)**	**O 1s (III)**	**Ti 2p$_{3/2}$**	**Ti 2p$_{1/2}$**	**B 1s (I)**	**B 1s (II)**
TiO$_2$	529.82	531.41	-	458.58	464.12	-	-
B-TiO$_2$	530.09	531.13	532.46	458.85	464.39	191.91	192.46

Table 1| Binding energies (eV) of O 1s, Ti 2p and B 1s peaks present in the XPS spectra of undoped and B-doped TiO$_2$ samples.

1.2.2.5 <u>Morphological and elemental characterisation</u>

The morphological features and the elemental analysis of the samples were investigated by scanning electron microscopy (SEM) and energy dispersive X-ray (EDX) spectroscopy. As shown in SEM images (**Figures 7a,b),** the surface of both photocatalysts presents a homogenous distribution of particles with irregular shapes, without indications of a specific

morphology and crystal facets exposed. Additionally, there is no apparent effect of B doping on these aspects.
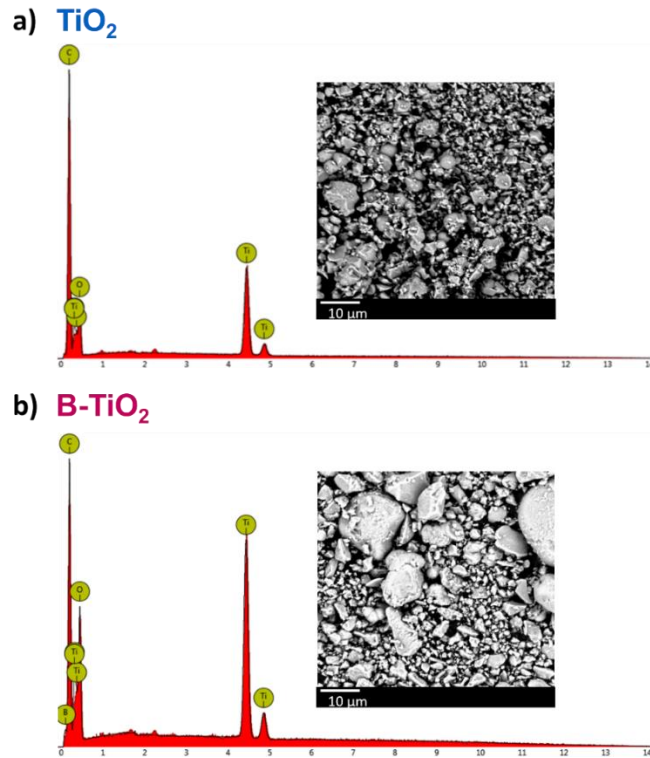
Figure 7| EDX spectra and SEM images (inset) of **a)** TiO_2 and **b)** B-TiO_2 powders.

The composition of both prepared photocatalysts is provided in **Table 2**.

Sample	Weight concentration (wt%)			
	Ti	**O**	**C**	**B**
TiO₂	33.3	53.3	13.5	-
B-TiO₂	34.4	57.5	6.7	1.3

Table 2| Composition of undoped TiO_2 and B-doped TiO_2 (based on EDX spectra).

The EDX results (acquired during SEM imaging) confirmed the presence of B atoms (with a weight concentration of 1.3%) in the doped photocatalyst. Moreover, in both undoped and doped TiO_2 powders, the weight percentage of Ti and O is almost the same, confirming the previous indications that doping with B does not creates significant oxygen vacancies.

1.2.2.6 <u>BET analysis</u>

Nitrogen (N_2) physical adsorption/desorption (on the surface of photocatalyst) technique was applied to gain insights on the textural properties of the sample including the specific surface area (SA_{BET}) the total pore volume (V_{pore}) and the pore diameter (D_{pore}). The N_2 adsorption-desorption curves and the corresponding pore size distributions are shown in **Figures 8a,b**, respectively.
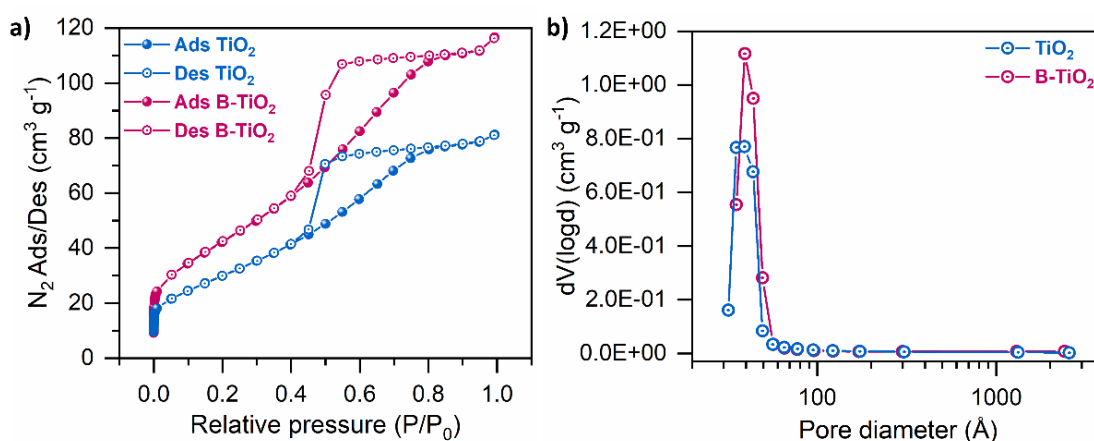
Figure 8| a) Nitrogen adsorption/desorption isotherms and **b)** pore size distribution curves of the undoped and B-doped TiO_2.

As shown in **Figure 8a**, according to the IUPAC classification; both photocatalysts present a type IV isotherm characteristic of mesoporous materials with an H2-type hysteresis loop that is typical of ink-bottle pores (i.e., a not well defined pore distribution in terms of size and shape). [64] The B-doped TiO_2 nanopowder has a slightly higher SA_{BET} value compared to that of TiO_2 (157.92 and 111.27 m^2 g^{-1}, respectively). Furthermore, the average pore diameter (D_{pore}) of each samples, determined from pore size's distribution curve (**Figure 8b**) is 33.83 and 39.46 nm for TiO_2 and B-doped TiO_2, respectively.

The textural properties of both samples are summarised in **Table 3**.

Sample	SA_{BET} (m^2 g^{-1})	V_{pore} (cm^3 g^{-1})	D_{pore} (nm)
TiO_2	111.27	0.12	33.83
B-TiO_2	157.92	0.17	39.46

Table 3| BET surface area and pore parameters of TiO_2 and B-TiO_2.

The differences are negligible (< 30%) suggesting a positive effect of the doping with B

atoms in reducing the sintering of titania. This result supports the previous findings that doping with B atoms does not generate oxygen vacancies at the surface. Indeed, on the contrary, the formation of surface oxygen defects in TiO_2 accelerates the sintering process, resulting in the reduction of SA_{BET} and porosity after an identical thermal treatment. [65]

1.2.3 <u>Photoelectrochemical characterization</u>

The electrochemical behaviour of TiO_2 and B-doped TiO_2 photocatalysts was evaluated by performing cyclic voltammetry (CV), chronoamperometry (CA) and electrochemical impedance spectroscopy (EIS) analysis.

1.2.3.1 <u>Cyclic voltammetry</u>

The CV curves were recorded without (**Figure 9a**) and with illumination (**Figure 9b**), from 0.036 to 2.036 V vs RHE at a scan rate of 10 mV s^{-1}. In the plots, only the latest CV profile (obtained after five stabilization cycles) was reported.
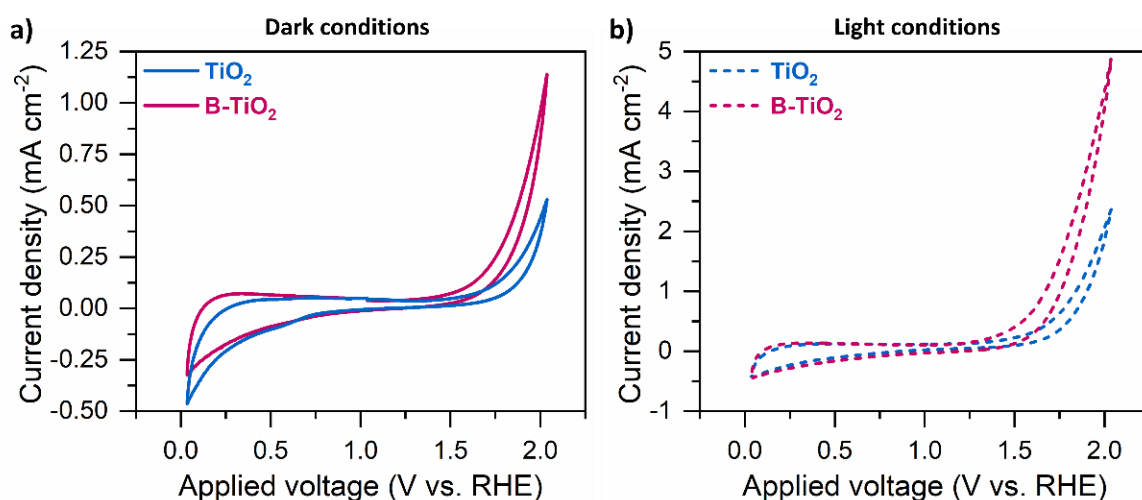
Figure 9| Comparison of cyclic voltammogram curves of TiO_2 and B-TiO_2 samples in 1 M KOH under **a)** dark conditions and **b)** light conditions.

While the CV profile (with or without illumination) of both samples shows a minor change in terms of the reduction current onset (related to H_2 generation, at an applied potential below 0.5 V compared to RHE), there is a marked difference in the oxidation region (related to O_2 generation, above 1.0 V compared to RHE). The illumination thus significantly promotes oxidation activity with respect to dark electrolysis only, and the effect is more pronounced in B-TiO_2 than TiO_2. The effect of light illumination is consistent with oxygen evolution,

which is the slow process in water electrolysis[66]. Regarding the reduction current, in dark electrolysis B-TiO_2 is less efficient than TiO_2, and therefore requires a larger onset overpotential (1.35 V vs 1.3 V for B-TiO_2 and TiO_2, respectively). Upon illumination, B-TiO_2 is also slightly less efficient than TiO_2, but needs a slightly lower onset overpotential to start the reduction process compared to TiO_2 (0.97 V vs 1.03, respectively). Note that the reduction of the potential is related to the photogenerated current upon illumination.

These results indicate that light promotes more water (photo)electrolysis at B-TiO_2 than at the TiO_2 surface, in agreement with photocatalytic data (**Figures 1a,b**). The effect could be due to either a more efficient stabilisation of holes at the surface, *e.g.* a more efficient charge separation[67] and thus a higher photocurrent generation, or (and) to the effect on water structure at the interface which enhances the coupled proton and hole transfer for water splitting[68].

1.2.3.2 Chronoamperometry

The CA profiles (**Figure 10**) were collected by performing six light ON/OFF cycles of 30 seconds for each at an applied potential of 1.136 V vs RHE. Moreover, three different filters (AM 1.5 G, UVC and UVB/C blocking filters) were applied to assess the response of the TiO_2-based photoelectrodes in specific wavelength regions.
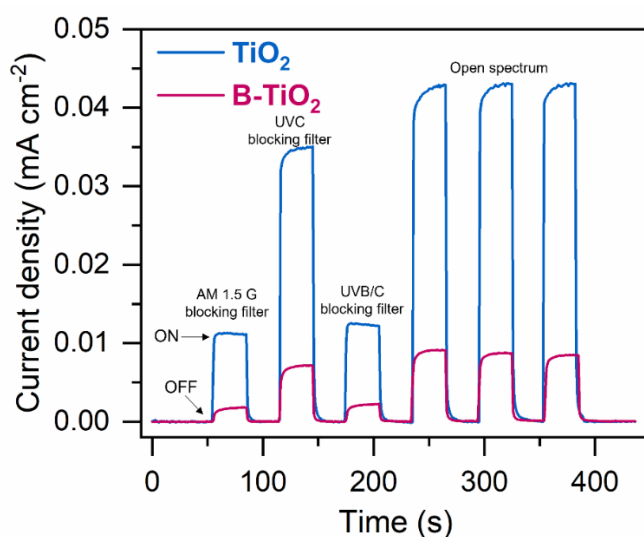
Figure 10| Chronoamperometric measurements for TiO_2 and B-TiO_2 samples (1.136 V vs RHE, 1 M KOH) using open UV-visible lamp spectrum (no light filter) and with light filter (AM1.5G, UVC, and UVB/C blocking filter). Data were normalised with respect to the surface area of the photocatalysts.

As can be seen from **Figure 10**, when the light is switched on, there is an initial rapid increase in the photocurrent followed by a slow rise until a constant value is reached. When the light is switched off a fast decay in the photocurrent which returns to its initial dark current value. The secondary slight increase in the photocurrent is due to the charge carriers diffusion time needed to reach a stable electric double layer (EDL). This observation is supported by the correlation between the photocurrent density and the stabilization time (higher photocurrent density requires more time to achieve a stable condition) and by the reproducibility of the photocurrent density behaviour in consecutive cycles. This result confirms that the photocurrent is not related to changes in the redox state of the semiconductor, as it may occur when activity is related, for example, to the presence of surface oxygen vacancies reacting with water.

Using the AM 1.5 G, UVC, and UVB/C filters, both TiO_2-based photoelectrodes are still active in the photocurrent generation, and as displayed in the last three ON/OFF cycles performed at open spectrum conditions the photocurrent behaviour is reproducible over several irradiation cycles. As expected, after cutting the UV light components (*i.e.,* by using AM 1.5 G, UVC and UVB/C filters) the photocurrent density of TiO_2 and $B-TiO_2$ decreases. For instance, under the AM 1.5 G filter, only ~ 20-25% of the open spectrum photocurrent remains.

Moreover, the decrease in the photocurrent density from open spectrum case to AM 1.5 G filtered irradiation is slightly more pronounced in $B-TiO_2$ than in TiO_2 (79% vs 74%). This indicates that, in our samples, doping with B does not improve the visible light response of TiO_2. In both open spectrum and filtered illumination conditions, TiO_2 has the highest photocurrent density compared to $B-TiO_2$. Therefore, these results indicate that doping with B does not enhance the charge separation, which induces a higher photocurrent density.

1.2.3.3 <u>Electrochemical impedance spectroscopy</u>

Additional information regarding the charge transfer phenomena that occur at the semiconductor/electrolyte interface were provided by EIS studies. The EIS measurements were carried out without and with light irradiation in the frequency range from 10^5 to 0.1 Hz with an amplitude of 0.01 V_{RMS} at applied potential ranging from 1.313 to 2.113 V vs RHE.

The Nyquist plots for both samples under dark and light conditions are shown in **Figures**

11a,d. The EIS data were fitted through a simple equivalent electric circuit (see **Appendix A 3.8** for more details).
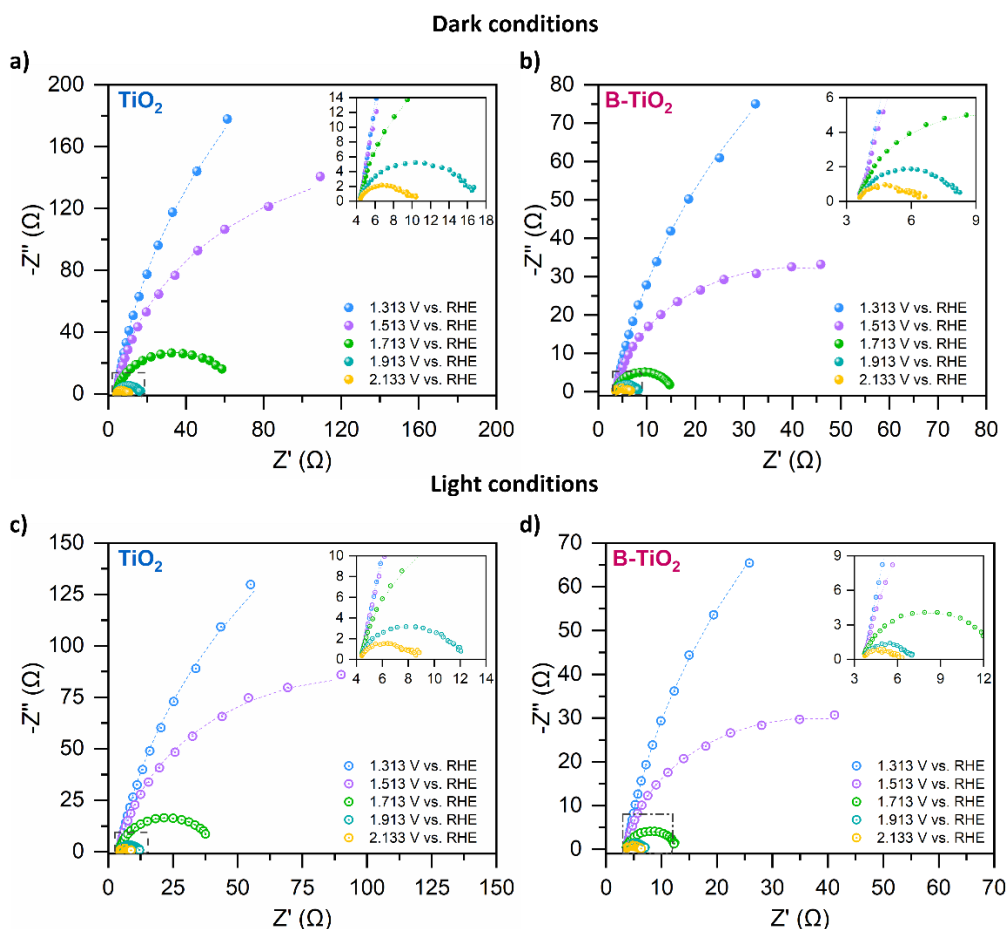
Figure 11 | Nyquist plots for TiO$_2$ and B-TiO$_2$ samples measured by varying the applied potential in **a,b)** dark and **c,d)** light conditions. Symbols represent the experimental impedance data while the dashed lines the fitting using the equivalent circuit model.

It is clear that, at all the applied potentials, the radius of semicircle for both photocatalysts is smaller under light conditions respect to dark conditions. This result is indicative of a lower R$_{ct}$ under illumination. Moreover, TiO$_2$ shows a higher R$_{ct}$ compared to B-TiO$_2$ (in both dark and light conditions). Therefore, the introduction of B atoms in TiO$_2$ promotes the electron transfer to water molecules. However, this effect is not related to a higher charge carrier generation rate (attributed to the surface stabilisation or to the reduction of thermal degradation paths), but to the promotion of the outer-shell electron transfer mechanism.

Table 4 lists the values of R$_{ct}$ resulting from the fitting of the EIS data (by using the Randles equivalent circuit) in dark and light conditions for TiO$_2$ and B-TiO$_2$.

	Dark conditions		Light conditions	
	TiO$_2$	(B)TiO$_2$	TiO$_2$	(B)TiO$_2$
Potential	R_{ct} (Ω)	R_{ct} (Ω)	R_{ct} (Ω)	R_{ct} (Ω)
1.313 V vs. RHE	838	345	534	345
1.513 V vs. RHE	315	73.6	189	66.9
1.713 V vs. RHE	60.2	11.8	37	9.21
1.913 V vs. RHE	12.6	4.85	7.8	3.48
2.133 V vs. RHE	5.80	2.32	3.97	2.81

Table 4 | Equivalent electric circuit parameters from EIS fitting data for TiO$_2$ and B-TiO$_2$ under dark and light conditions at different applied potentials.

1.2.4 **Steady-state photoluminescence**

As shown in **Figure 12**, both photocatalysts exhibit an emission peak at 460 nm, indicating that doping with B atoms does not introduce intermediates states between the valence and the conduction bands of TiO$_2$, as instead observed when the B doping is an order of magnitude higher[18, 69].
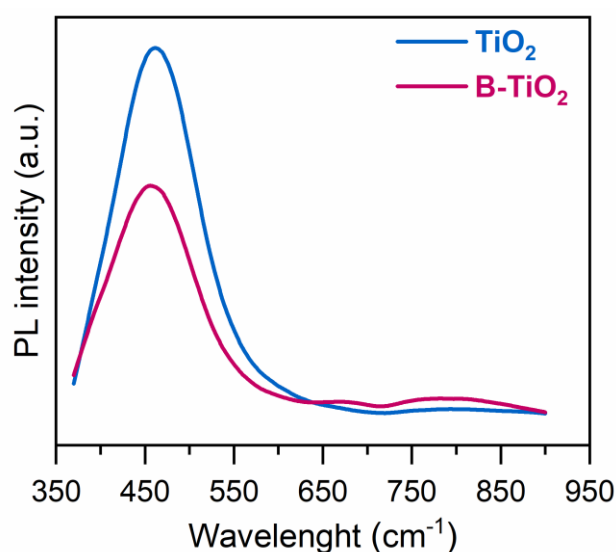
Figure 12| Photoluminescence spectra of TiO$_2$ and (B)TiO$_2$ samples.

Although PL spectra are not quantitative, the intensity of the PL emission in B-doped TiO$_2$ is lower than at TiO$_2$, giving an indication of a suppressed charge carrier recombination rate, in agreement with CA results (**Figure 9**).

1.2.5 FTIR measurements

Information on the structure and the arrangement of water at the interface with TiO_2 and B-TiO_2 have been gained by analysing the changes of the OH stretching band (in 2800-3600 cm^{-1} wavenumber region) at varying the surface hydration levels of the samples (see appendix A for experimental details). Indeed, the OH stretching band is a complex and broad structure resulting from the presence of different OH groups which vibrational frequencies provide important insights into the H-bond donor (D) and acceptor (A) status of the water molecules as well as of the strength of the H-bond network[70, 71]. As illustrated in **Figures 13a,b** the IR spectrum in the OH stretching region for the two investigated systems appears significantly different (a normalised representation is also shown to highlight the shape variations, **Figures 13c,d**). From this observation it turns out that a different H-bond organisation at the interface with the two titania photocatalysts takes place.
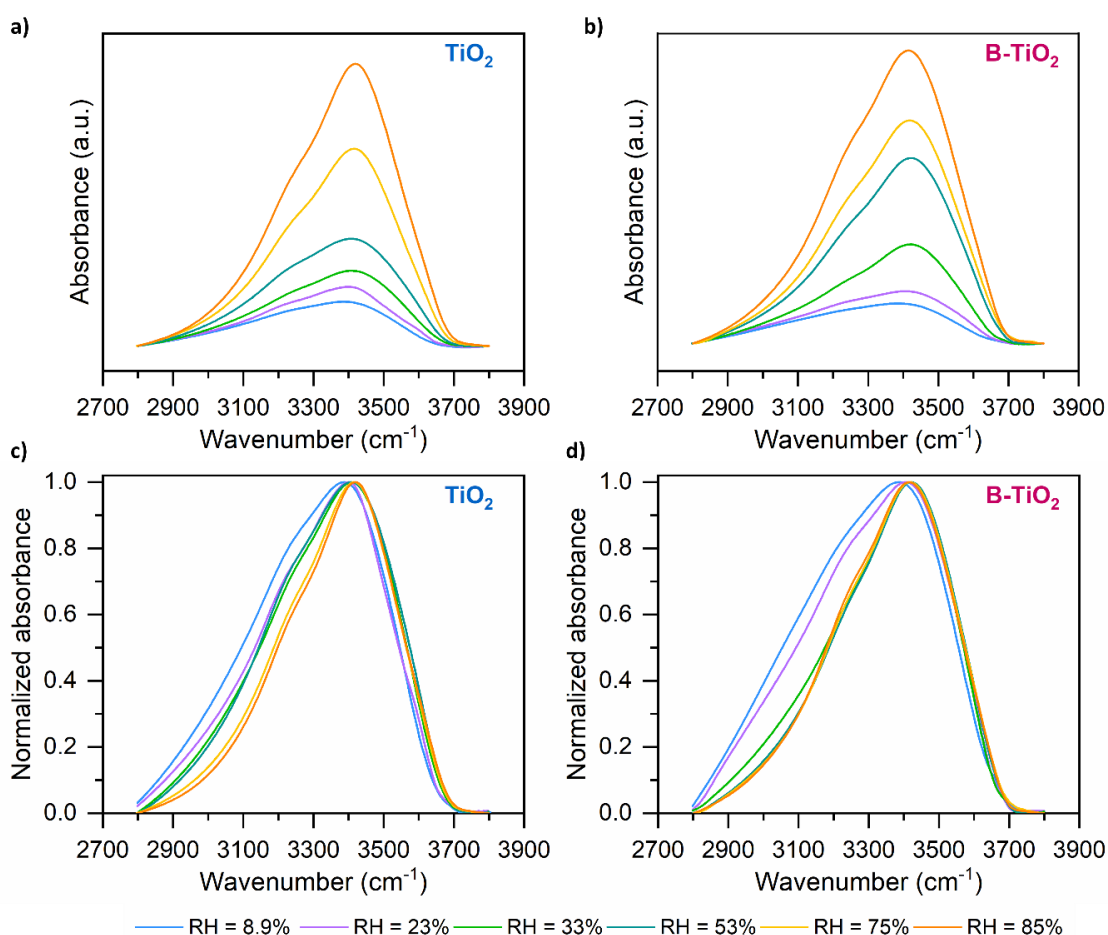
Figure 13 | FTIR spectrum in the OH stretching region at different values of RH of **a)** TiO_2/H_2O interface and **b)** B-TiO_2/H_2O interface. The corresponding normalized spectrum in **c)** and **d)**, respectively.

With the aim of providing a detailed description of the arrangement of interfacial water, the broad OH stretching band has been deconvoluted into five Gaussian components (two examples are shown in **Figures 14a,b**, the other results are shown in **Appendix A4**).
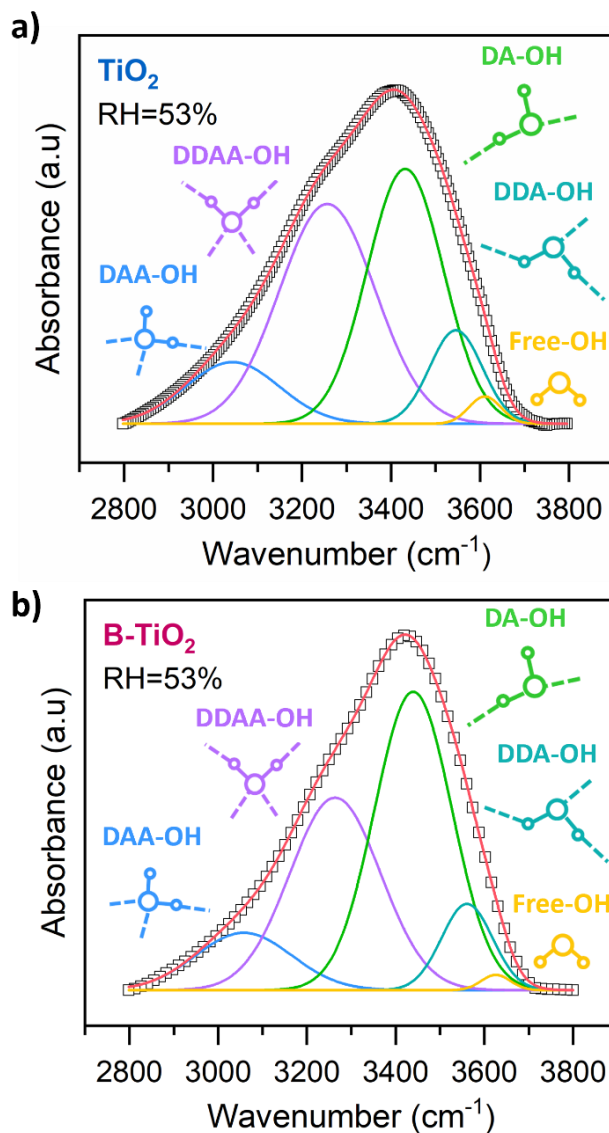
Figure 14 | Gaussian deconvolution of the OH stretching band of **a)** TiO_2 and **b)** B-TiO_2 samples at RH=53%.

These five contributions correspond to different OH symmetric stretching vibrations, including: i) single donor-double acceptor (DAA-OH, ~3040 cm^{-1}), ii) double donor-double acceptor (DDAA-OH, ~3220 cm^{-1}), iii) single donor-single acceptor (DA-OH, ~3430 cm^{-1}) and iv) double donor-single acceptor (DDA-OH, ~3570 cm^{-1}), describing fully or partly (defective topology) H-bonded water molecules, and v) free-OH vibrations (~3636 cm^{-1}) related to water molecules not involved in H-bonds.

In particular, significant insights into the organization of the H-bond network arise from the comparison of the relative areas (*i.e.,* the ratio between the area of a Gaussian subpeak and the total area of the OH stretching band) of these five spectral components (**Figures 15a-e**).
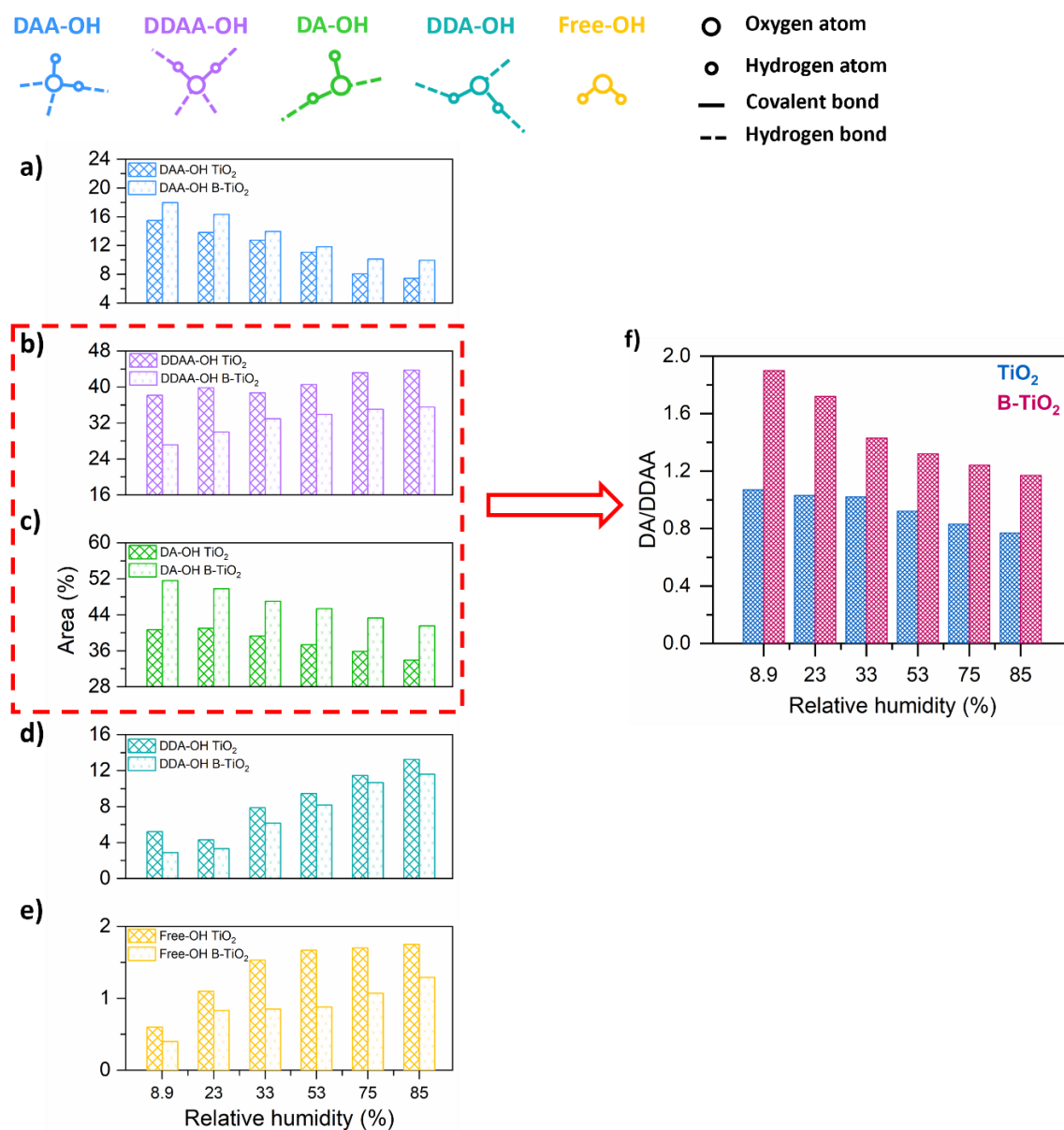
Figure 15| a-e) Changes with the relative humidity of the relative areas of the five spectral components obtained by the Gaussian deconvolution of the OH stretching band for both TiO_2/ and B-TiO_2/water interface. **f)** Mean H-bonding state of water in TiO_2 and B-TiO_2 samples.

For both samples, the main finding is that the DDAA and DA water molecules populations constitute the major contributions (more than 80%) of the whole OH stretching band (**Figures 15b,c**). Specifically, the most representative patterns at the interface with pure TiO_2

consist of fully tetrahedrally coordinated H-bonded water species (DDAA) along with some H-bond topological defects (under coordinated H_2O molecules) of the type DA. In contrast, the local environment of water molecules at the interface with B-TiO_2 is dominated by water dimers (DA species), especially for RH values below 75%, as shown in **Figure 15c**. Therefore, in agreement with mechanisms very recently proposed by Jiang et al. [72], the presence of B atoms hampers the percolation of tetrahedrally-coordinated water clusters and largely enhances the DA population, leading to the formation of chains of dimers. It is noteworthy that water dimers have been found to exhibit a higher photodissociation activity than larger clusters[73] and that defective H-bond networks are generally more effective for proton transfer processes[74].

Additionally, since the DDAA and the DA are the dominant water motifs involved in the H-bonding network at the interface with the studied systems, special attention was paid to the analysis of these contributions. Specifically, according to the criterion proposed by Choe et al., [75] the ratio between DA and DDAA components was calculated for assessing the hydrogen bonding state of water at the interface with the TiO_2 samples. The DA/DDAA water molecules species ratio for H_2O molecules adsorbed on the B-TiO_2 surface is greater compared to that on the TiO_2 surface, indicating a weaker H-bond network that exhibits larger fluctuations (**Figure 15f**). At the same time, this finding suggests a slightly more hydrophobic character of the B-TiO_2[76], as supported by the calculation of the average number of H-bond per water molecule as function of the RH for the two different system under investigation.

The schematic illustration of the organization of water molecules at the interface with TiO_2 and B-TiO_2 resulting from the FTIR analysis is shown in **Figures 16a,b**.
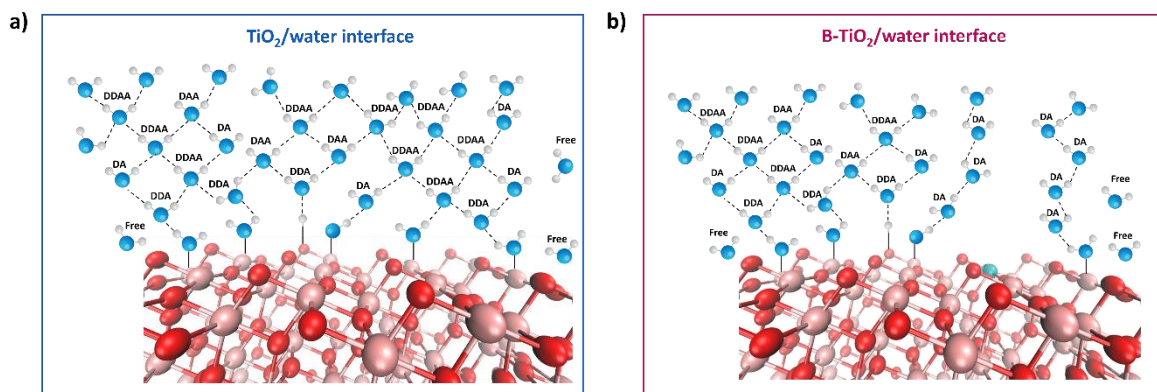
Figure 16| Schematic illustration of the H-bond network in **a)** TiO_2 and **b)** B-TiO_2 photocatalysts.

In conclusion, according to our FTIR results, the unexpected improved water splitting efficiency on the hydrophobic B-TiO$_2$ catalyst steams from the favourable arrangements of water mainly in chain of dimers. These experimental findings are very well supported by DFT-MD simulations. For more detail on water interactions with the titania surface by DFT-MD simulations see next chapter.

1.3 <u>Conclusion</u>

By comparing the physical chemical characteristics of TiO$_2$ and B-TiO$_2$ samples, it is inferred that the doping with a low amount of B (1%) does not significantly modify the intrinsic properties of titania. In the B-TiO$_2$ sample, about 30% of the B is present on the surface as well-dispersed boric acid (B$_2$O$_3$)-like species. The remaining B is hosted in the TiO$_2$ lattice, mainly as interstitial B. Nevertheless, from the Uv-vis analysis there is no evidence that the interstitial B induces a downward shift of electronic band edges, which could potentially justify an enhanced water-splitting activity[77].

Experimental characterisations (including XRD, micro-Raman, SEM-EDX and BET analysis) allow also to exclude that the enhanced performances of B-TiO$_2$ are related to other possible interpretations, such as the creation of heterojunctions or heterophases, or changes in the crystal facets, porosity or nanomorphology [78].

Additional electrochemical tests, including cyclic voltammetry (CV), chronoamperometry (CA) and electrochemical impedance spectroscopy (EIS), and steady-state photoluminescence (PL) measurements, were performed to rule out the possibilities of improved charge separation, charge stabilization, and the formation of intermediate states (*i.e.,* oxygen vacancies) as potential reasons for the enhanced activity of B-TiO$_2$ towards water splitting.

It is worth pointing out that the aim of this project is to clarify how the structural organisation of water at the interface with TiO$_2$ is linked with the water splitting ability of a semiconductor rather than improving the performances of the photocatalyst itself. For this reason, in the photocatalysts synthesis process, we did not intentionally add either metal nanoparticles or metal ions of Cu, Fe, noble metals and other metals (which may act as cocatalysts). Consequently, the lack of a cocatalyst, even at a trace level (as proven by chemical analysis) rules out the possibility that the improved ability towards water splitting of B-TiO$_2$ can be

related to this aspect[68]. For the same motivation, B doping amount was not optimized and was purposely kept at low level.

Fourier Transform Infrared (FTIR) measurements at different controlled relative humidity (RH) conditions reveal that the surface modification by doping profoundly affects the water structure at the interface, resulting in defective configurations of H-bonded water molecules. A significant population of single H-bond donor-acceptor H_2O species, instead of tetrahedrally coordinated ones, has been found at the B-doped TiO_2 surface. These experimental FTIR findings suggest that the surprising five-fold enhancement in the H_2 production rate achieved with the hydrophobic B-TiO_2 photocatalyst results from the advantageous arrangements of water molecules, predominantly forming chain of dimers

PROJECT 1

COMPUTATIONAL RESULTS

Chapter 2

DFT-MD simulations of (101) TiO$_2$/water interface and (101) B-TiO$_2$/water interface

Summary

This chapter deals with clarifying the structure of water and the organization of the H-bond network at the interface with TiO$_2$ and B-TiO$_2$ by exploiting Density Functional Theory molecular dynamics (DFT-MD) simulations. In this work, we overcome the limitations of most literature studies, which in general, when describing the solid/water interface, adopt only a water molecule or at the best a water monolayer in contact with the catalyst. Indeed, we provided a more realistic view of the interfacial water behaviour on the investigated surfaces by including an explicit liquid water slab (132 water molecules) in the simulation box.

This part of work has been carried out in collaboration with Dr. Fabrizio Marco Creazzo (Department of Chemistry, University of Zürich, Zürich, Switzerland) and Dr. Giuseppe Cassone (Institute for Chemical-Physical Processes, National Research Council of Italy (IPCF-CNR), Messina, Italy).

2.1 <u>Introduction</u>

Quantum-level computations based on Density Functional Theory (DFT) are a powerful tool to clarify the mechanistic interplay between the structure interfacial water and the titania surface activity. Previous computational investigations have been employed to study titania materials, focusing on improving their photocatalytic properties[79-86]. Most of these 'surface-science' calculations concern the surface structure, the formation of heterojunctions and heterostructures, and the surface reconstruction, adopting a static approach and an implicit solvent framework. However, the organisation of explicitly treated water (i.e., at the DFT level) at the interface (with a bulk density of 1 g cm^{-3}), its dynamics at finite temperature, and their impact on the surface properties of a (undoped or B-doped) titania catalysts remain elusive. Previous studies on the interaction of water with the titania surface were limited to the identification of chemisorbed species and, in some cases, the single or bi-layer organisation of water molecules on the surface of TiO_2[87-89]. Only a few computational attempts provided insights about the dynamical H-bond environment at the TiO_2-water interface[90-93].

What is not fully addressed yet, both theoretically and at an atomistic level, is how the modification of the surface properties (e.g., by doping), the reorganisation of the interfacial water environment as well as the surface ability of adsorbing/dissociating water molecules can affect the experimentally proven changes of the catalyst properties in the context of water splitting.

Intending to fill this lack of knowledge, in this chapter, we provide a detailed characterisation of not only the (101) undoped and B-doped anatase surfaces of titania but also of the dynamical finite-temperature behaviour of liquid water at the interface with the (101) TiO_2 and (101) B-TiO_2 by exploiting spin-polarised Density Functional Theory molecular dynamics (DFT-MD) simulations and an explicit water environment. We overcame the static DFT picture and the implicit solvent scheme of most previous studies. DFT-based calculations were also performed on bulk anatase TiO_2.

The description of the computational methods, titania surface modelling and the structural, electronic and mechanical properties of TiO_2 is detailed in **Appendix A5.**

2.2 (101) TiO$_2$ in contact with liquid water

Understanding and controlling the surface chemistry of TiO$_2$ is a key aspect in the field of photocatalysis to fine characterize and tune the surface chemical activity of TiO$_2$ towards water splitting[94, 95]. When the anatase TiO$_2$ bulk solid is cut along the (101) crystallographic symmetry plane (**Figure 1a**), under-coordinated Ti and O surface atoms are surface exposed. In particular, the (101) surface exposes Ti atoms which are coordinated to five (instead of six) O atoms, leading to the one-fold coordinatively unsaturated Ti atom (Ti$_{cus}$), see **Figure 1b**. Bridging oxygen atoms O$_{br}$, which are coordinated to two (rather than three) Ti atoms, are also present at the anatase (101) TiO$_2$ surface: O$_{br}$ binds two Ti atoms in a sort of oxygen bridge between them (Ti-O bond length $\sim$ 1.85 Å on average). Moreover, 3-fold surface oxygen atoms O$_{3f}$, (fully) coordinated to three surface Ti atoms, are still present in a planar-like geometry. The Ti-O bond length is in the range of $1.96 - 2.01$ Å.
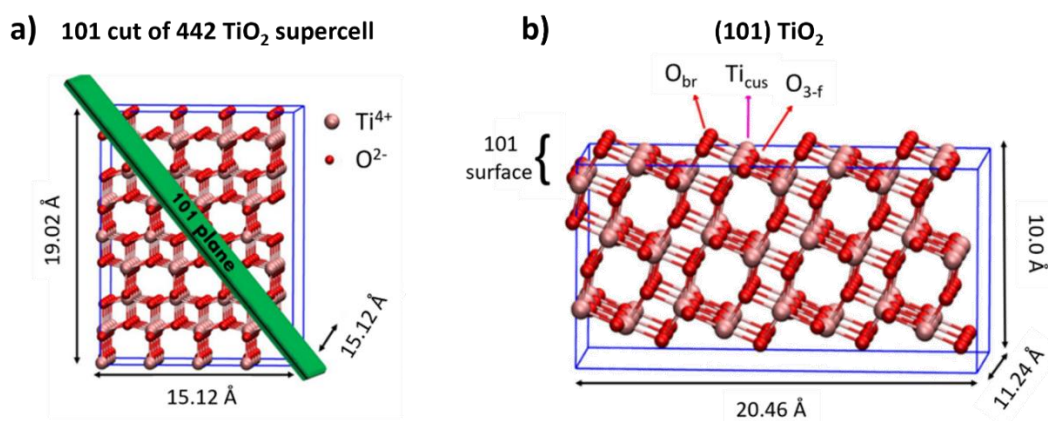
Figure 1| a) 442 supercell bulk structure of anatase TiO$_2$ is cut along the (101) crystallographic plane (in green). **b)** Composition and surface speciation of anatase-TiO$_2$ model after the (101) cut. This panel shows the 3 layers-thickness TiO$_2$ (216 atoms) in a stoichiometric slab model.

The B-doped TiO$_2$ have been constructed by replacing 2 surface Ti^{4+} atoms with 2 B^{3+} atoms. When surface Ti atoms are replaced by B atoms (*i.e.,* B^{3+} instead of Ti^{4+}), the "regular" crystalline surface geometry of TiO$_2$ (**Figure 2a**) is distorted locally with the formation of two surface bond-defects (**Figure 2b**). This is due to the fact that B^{3+} is (fully) saturated by 3 O atoms in a trigonal coordination geometry (instead of 5 O atoms as for surface Ti$_{cus}$).
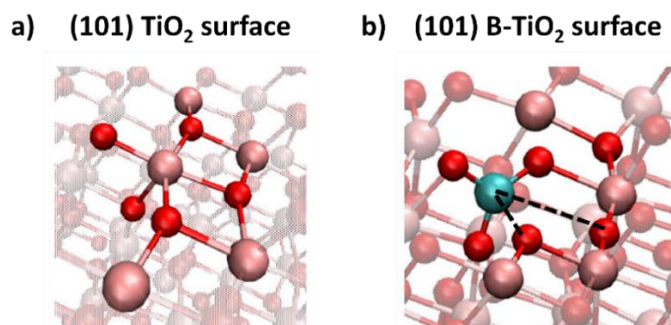
Figure 2| Zoom-in view of **a)** (101) TiO$_2$ surface: Ti$_{cus}$ atoms on the surface are coordinated to five O atoms in a pristine surface geometry and **b)** (101) B-TiO$_2$ surface: B atoms on the surface are coordinated to three O atoms. The two surface bond defects are highlighted in black dashed lines. Ti, O and B atoms are represented in pink, red ad cyan, respectively.

The undoped and B-doped (101) TiO$_2$ surfaces were put in contact with 132 water molecules (bulk liquid water environment, density ~1 g cm^{-3}), leading to the solid liquid interfaces shown in **Appendix A5**. During our 25-ps-long DFT-MD simulations, we observed that exposing the (101) TiO$_2$ surfaces to liquid water stabilises the unsaturated Ti$_{cus}$ and O$_{br}$ surface sites which absorb entire or dissociated water molecules (**Figures 3a,b**).
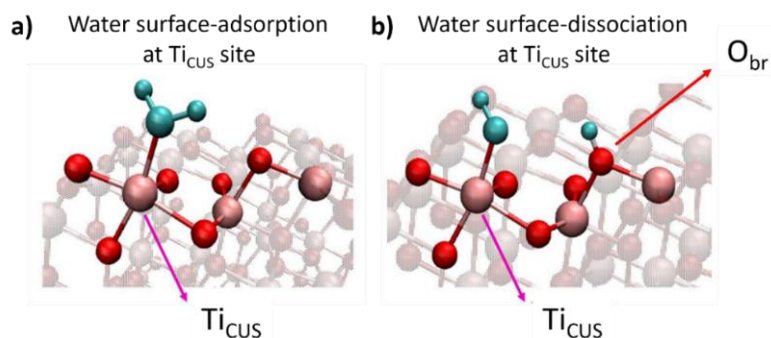
Figure 3| a) Water adsorption and **b)** surface dissociation mechanisms at the (101)-TiO$_2$ surface. Ti and O atoms are in pink and red color, respectively, while the water molecule is colored in cyan.

Detailed results are summarized below:

- (101) TiO$_2$: 10 entire and 2 dissociated water molecules are surface-adsorbed at the unsaturated Ti$_{cus}$ leading to a surface termination/speciation with 80% of μ_1-OH$_2$ and 20% of μ_1-OH exposed sites over Ti$_{cus}$ atoms, as depicted in **Figure 4**. The unsaturated O$_{br}$ surface sites receive the two protons (from the two dissociated water molecules at Ti$_{cus}$ sites), leading to 2 μ_2-OH exposed sites. Furthermore, 3-fold surface oxygen atoms O$_{3f}$ (12), (fully) coordinated to three surface Ti atoms in a planar arrangement, are still

present and not affected by the presence of water at the surface.
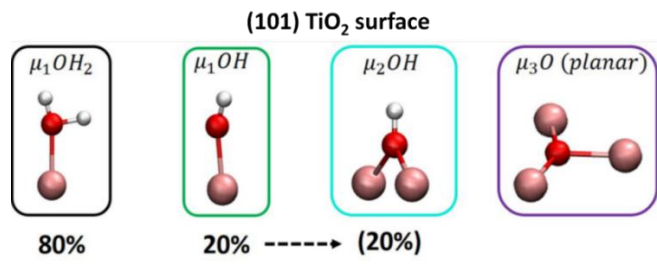
Figure 4| Equilibrium composition and speciation of the (101) TiO$_2$ surface in contact with liquid water. Ti, O and H atoms are in pink, red and white color, respectively.

- (101) B-TiO$_2$: over a total of 10 Ti$_{cus}$ surface sites, 8 are water-adsorption sites, whereas 2 Ti$_{cus}$ (20%) remain available over the simulation. In particular, 7 entire and 1 dissociated water molecules are surface-adsorbed over the 8 Ti$_{cus}$ surface sites, leading to 70% of μ_1-OH$_2$ and 10% of μ_1-OH exposed sites, as depicted in **Figure 5**. The unsaturated O$_{br}$ surface sites receive the dissociated proton leading to 1 μ_2-OH exposed site. Furthermore, 3-fold surface oxygen atoms O$_{3f}$ are still present and not affected.
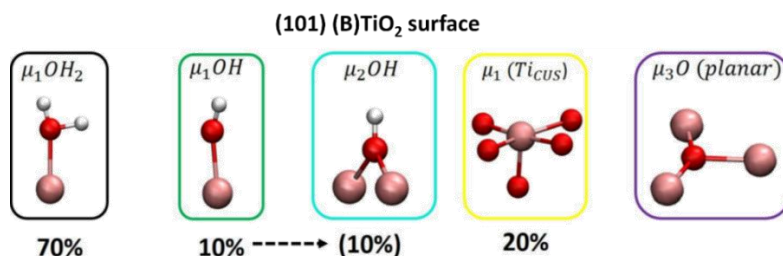
Figure 5| Equilibrium composition and speciation of the (101) B-TiO$_2$ surfaces in contact with liquid water. Ti, O and H atoms are in pink, red and white color, respectively.

Once elucidated the equilibrium composition between hydrated motif at the undoped and B-doped (101) TiO$_2$ surfaces in contact with liquid water, further analyses have been provided in order to investigate the solid-water H-bond interactions. The total number of μ_1, μ_2 and μ_3O surface terminations described above does not change during the simulation time. However, the dynamics of the interfacial water show proton hoppings/sharing between the (hydrated) catalyst surface and the water environment. In particular, from our DFT-MD, turns out that:

- For (101) TiO$_2$: all the μ_1-OH$_2$ (over Ti$_{cus}$) and μ_2-OH (over O$_{br}$) surface sites are H-bonded with water molecules, resulting in 70% of the water molecules, belonging to the interfacial water layer, H-bonded to the surface. The majority (*i.e.,* 80%) of these surface-water H-bonds are made by water molecules that are, at the same time, H-bond donor/acceptor towards the surface (**Figure 6**), with an average H-bond distance (between surface oxygen and water hydrogen) of ~1.6 Å: in particular, the H-bonded water molecules act as H-acceptor from the μ_1-OH$_2$ as well as H-donor to μ_2-O site, as depicted in **Figure 6**. The remainder 20% of H-bonded water molecules acts as H-donor to μ_2-O sites (over O$_{br}$). 3-fold surface oxygen atoms O$_{3f}$ are still present and unaffected by the interface's H-bond interactions.

- For (101) B-TiO$_2$: all the μ_1-OH$_2$, μ_2-OH and Ti$_{cus}$ surface sites are H-bonded with water molecules, resulting in 50% of water molecules at the interface being H-bonded to the surface (average H-bond distance ~ 1.6 Å). The majority (60%) of the H-bonded water molecules are H-acceptor from the μ_1-OH$_2$ as well as H-donor to μ_2-O site, as already shown in **Figure 6**. The other 40% of H-bonded water molecules are H-donor to μ_2-O sites (over O$_{br}$). 3-fold surface oxygen atoms O$_{3f}$ are still present and unaffected by the interface's H-bond environment.
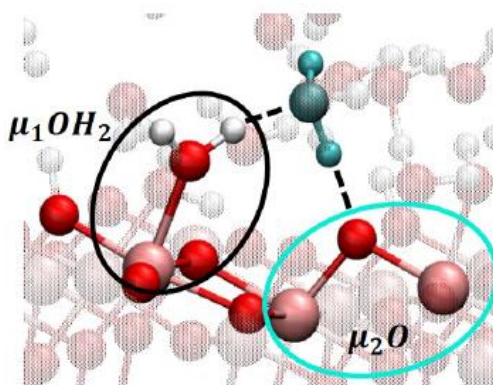
Figure 6 Magnification of the predominant surface-water H-bond pattern at the aqueous (101) TiO$_2$ interface. The H-bonded water molecule acts as an H-acceptor from the μ_1-OH$_2$ and as H-donor to the μ_2-O site. Ti and O atoms are pink and red, respectively, while the water molecule is cyan.

These computational results indicate that water adsorption phenomena and H-bond interactions show a slightly hydrophobic character in the case of the (101) B-doped TiO$_2$ surface, where only 50% of the interfacial water molecules are H-bonded at the surface.

Interestingly, the surface B sites at the (101) B-doped TiO_2 are not affected by water adsorption phenomena as well as by the interfacial H-bonds interactions, resulting in sites that are neither available for adsorbing/dissociating interfacial water nor for forming H-bonds. When B atoms replace surface Ti atoms, they systematically relax as inner sites compared to the surface Ti atoms, *i.e.,* B atoms move towards the solid sub-layer to fulfil their coordination (**Figure 2b**). This is further supported by the evaluation of the atomistic radial distribution functions (RDFs) (**Figure 7**).
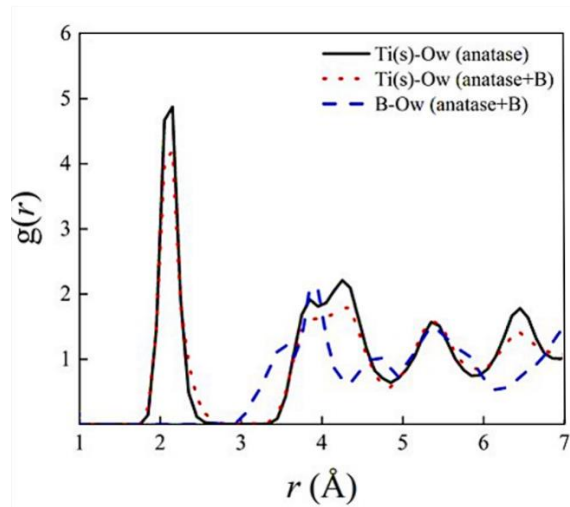
Figure X7| Ti(s)-O_w and B-O_w RDFs at the (undoped and doped) (101) TiO_2/water interfaces.

In fact, by comparing the RDF between titanium atoms Ti(s) at the surface and the water oxygen atoms O_w, and that between boron atoms B at the surface and the water oxygen atoms O_w shown in **Figure 7** (solid black and dashed blue curves, respectively) Ti(s) atoms are closer to water (exhibiting an average distance of $\sim$2.1 Å) than (inner-site) B atoms, which are on average at $\sim$3.9 Å from water.

In addition, the values of the work functions calculated for the (101) undoped and B-doped TiO_2 surfaces are shown in **Figure 8** and listed in **Table 1**.

The work function value is $\sim$ 5.1 eV (experimental values $\sim$ 4.8-5.2 eV[96, 97]) at the anatase (101) TiO_2 bare surface, and $\sim$ 1.8 eV when the anatase (101) TiO_2 surface is in contact with liquid water. For the B-doped anatase (101) TiO_2, the values of 4.8 eV and 1.7 eV have been obtained at the bare surface and at the water interfacial system, respectively. These results are in fairly good agreement with the experimental results present in the literature about bare

TiO$_2$ anatase surface[96, 97], confirming that the DFT-PBE+U representation and the computational setup are reliable in reproducing the work function values and its changes[98].
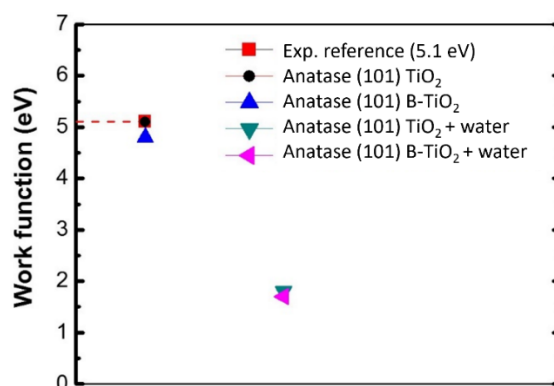
Figure 8| Work function (eV) calculated for the (101) TiO$_2$ and B-TiO$_2$ surfaces in direct contact with vacuum or with liquid water. The red square in the graph is the average work function experimental value for bare TiO$_2$ from Refs. [96, 97], equal to 5.1 eV.

System	Work function (eV)
(101) TiO$_2$	5.1
(101) TiO$_2$ + water	1.8
(101) B-doped TiO$_2$	4.8
(101) B-doped TiO$_2$ + water	1.7

Table 1| Calculated surface work function (eV) values.

Although these computational modelling neglects the effect of light irradiation (and related voltage application), they are in fairly good agreement with the experimental findings showing that in the B-doped TiO$_2$ sample, the enhanced water splitting activity is not due to a modification in the charge separation (no significant difference in the work function values of the undoped and doped TiO$_2$) or a change in terms of the water chemisorption sites given by the B presence. Instead, it is due to a local change in the structural organisation of the water molecules in contact with the solid surface. This is somehow related to the influence of doping on H-bonding and local electric fields. In fact, the presence of a Ti atom instead of a B one produces a local (within 3-4 Å) surface electric field intensity on the order of 0.10 V/Å oriented towards the water environment (i.e., isotropically outward the site), as shown in **Figure 9**.
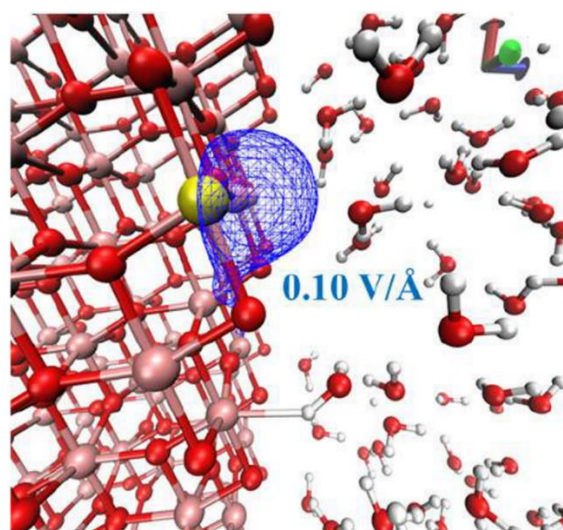
Figure 9| Local electric field determined as the difference of the isocontours between a system containing in the site colored in yellow of the TiO$_2$ surface a Titanium atom and a system containing a Boron atom in the same position for isovalues equal to 0.10 V/Å.

This local electric field, which is absent when B atoms replace the Ti ones, might be responsible for the more prominent hydrophilic character of neat TiO$_2$ with respect to its B-doped counterpart. In fact, it is well known that electric fields of this strength are capable of ordering the H-bond network of liquid water[71, 99], a circumstance rationalising the larger structuring of the local water environment at the non-doped TiO$_2$ surface. This way, the surface properties are modified upon doping and this induces a deeply different interfacial water arrangement. These aspects are crucial in charge transfers phenomena taking place at the interface, which depend on solvent reorganisations and local electric fields[100-102] and ultimately affect the water splitting activity.

2.3 **Conclusions**

DFT-MD simulations at the (101) TiO$_2$ and B-TiO$_2$ at the interface with liquid water support the FTIR experimental findings, showing that the DA population is the most representative in describing surface-water H-bond interactions at the B-TiO$_2$ surface. Moreover the computational results also confirm the slightly hydrophobic character of B-TiO$_2$. In a nutshell, water adsorption phenomena and H-bond interactions show that the (101) TiO$_2$ surface has a hydrophilic character, in which most of surface sites are adsorption sites, and the majority of interfacial water molecules are H-bonded to the surface. In contrast, a slightly hydrophobic character describes, the (101) B-TiO$_2$ surface, where only 50% of the interfacial

water molecules are H-bonded to the surface. Interestingly, the surface boron sites at the (101) (B)TiO$_2$ are not affected by water adsorption phenomena as well as by the interfacial H-bonds interactions, i.e. resulting in sites which are neither available for adsorbing/dissociating interfacial water nor for establishing H-bonds. When B atoms replace surface Ti atoms, they systematically relax as inner sites compared to the surface Ti atoms, i.e. B atoms move towards the solid sub-layer to fulfil their coordination. This fact is further supported by the evaluation of the atomistic radial distribution functions (RDFs). By comparing the RDF between titanium atoms Ti(s) at the surface and the water oxygen atoms O$_w$, and that between boron atoms B at the surface and the water oxygen atoms O$_w$ results that Ti(s) atoms are closer to water (exhibiting an average distance of ~2.1 Å) than (inner-site) B atoms, which are on average at ~3.9 Å from water. In our TiO$_2$ and (B)TiO$_2$ samples, the enhanced water splitting of the latter is not due to a modification in the charge separation or a change in terms of the water chemisorption sites given by the B presence. Instead, it is due to a local change in the structural organization of the water molecules in contact with the solid surface. This fact is somehow related to the influence of doping on H-bonding and local electric fields. The presence of a Ti atom instead of a B one produces a local (within 3-4 Å) surface electric field intensity on the order of 0.10 V/Å oriented towards the water environment (*i.e.,* isotropically outward the site). This local electric field, which is absent when B atoms replace the Ti ones, might be responsible for the more prominent hydrophilic character of neat TiO$_2$ with respect to its B-doped counterpart. Electric fields of this strength can order the H-bond network of liquid water[71, 99], a circumstance rationalising the larger structuring of the local water environment at the non-doped TiO$_2$ surface. This way, the surface properties are modified upon doping, which induces a deeply different interfacial water arrangement. These aspects are crucial in charge transfer phenomena at the interface, which depend on solvent reorganizations and local electric fields[100-102] and ultimately affect the water splitting activity.

PROJECT 2

Chapter 3

Ethanol oxidation reaction electrocatalysts

Summary

The work described in this chapter was conducted within the framework of the European Project DECADE (DistributEd Chemicals And fuels production from CO_2 in photoelectrocatalytic DEvices) and was carried out during an abroad research program (from March 2022 until August 2022) held at the Institut Català d'Investigació Quimìca (ICIQ, Tarragona, Spain) under the supervision of Professor José Ramón Galán-Mascarós. The main goal of the DECADE project is to develop an innovative photoelectrocatalytic (PEC) cell for CO_2 reduction by avoiding water oxidation as the anodic reaction. This new PEC device uses waste CO_2 and bio-ethanol as feedstocks for the cathodic and anodic parts, respectively. This approach can be employed to produce the same product *i.e.,* ethyl acetate both at the anodic side by oxidation of ethanol and at the cathodic side by reduction of CO_2.

Specifically, this chapter deals with the description of the development and optimization of a highly efficient and stable electrocatalyst for the EOR. To this end, the electrocatalyst material, deposition technique, and reaction medium, were all properly tailored to achieve the desired oxidation product. In particular, several bimetallic and trimetallic alloys based on Critical (PtSn) and Non Critical (CuSn and NiCuSn) Raw Materials were synthetized on a carbon cloth (CC) support through electrodeposition and impregnation methods. Moreover, concentrated ethanol (ethanol 96% with $LiClO_4$ 0.2 M) has been selected as reaction medium to push the selectivity towards ethyl acetate. At the time of submission of this thesis, the Decade project is still in progress.

3.1 <u>Introduction</u>

In the last decades, the release of millions of tons of carbon dioxide (CO_2) resulting from the widespread use of fossil fuels has raised serious environmental issues, such as atmospheric pollution and global warming. Consequently, finding an effective solution to capture and reduce the CO_2 emission is one of the foremost priority for the scientific community. In this context, by mimicking the natural photosynthesis, the photoelectrochemical (PEC) CO_2 reduction into high chemical fuels by using solar energy and water is a promising green approach tor resolve the aforementioned problems. [103, 104] However, the high overpotential required to carry out water oxidation reaction is the main limiting factor to PEC performance. [105] A potential alternative consists in coupling the CO_2 reduction reaction (CO_2RR) with the ethanol oxidation reaction (EOR). Coupling the selective EOR with the CO_2RR offers two advantages: i) the energy required for the EOR is lower than that needed for the oxygen evolution reaction (OER), enabling the overall reaction to occur at a more favourable applied potential[106], ii) the oxidation products, including acetic acid, acetaldehyde or ethyl acetate have a higher market value than oxygen[106]. However, such coupled systems still face the problems of the selectivity and separation of desired products. [107] To overcome this hurdle, a promising but challenging approach is to generate the same product at both the cathodic and anodic sides of a PEC device. In this scenario, the European Project DECADE (DistributEd Chemicals And fuels production from CO_2 in photoelectrocatalytic DEvices) aims to develop a new PEC device that uses waste CO_2 and bio-ethanol as inputs for the cathodic and anodic parts, respectively, to selectively produce ethyl acetate that can be used as green solvent or fuel additive. Specifically, on the anodic side bioethanol is oxidized to acetate which then reacts with ethanol to produce ethyl acetate. On the cathodic part, CO_2 is reduced into acetate which further reacts with ethanol to form ethyl acetate. An integrate PV module allows to drive the reaction by using sunlight.

This chapter is devoted to the description of the design and fabrication of the anodic side to selectively control the EOR. This was a non trivial task, as the number of existing literature studies for the oxidation and selective conversion of ethanol to ethyl acetate is very limited[108, 109]. Moreover, the few present works are mainly proposed for alkaline media (KOH 1 M and ethanol 1 M). In the Decade project in order to push the selectivity towards ethyl acetate and boost its production rate, concentrated ethanol 96%, with $LiClO_4$ 0.2 M (as

electrolyte to improve the ions conductivity), has been chosen as reaction medium[110-112]. In this regard, it is crucial to highlight that an high performing electrocatalyst in aqueous solution can be non active when working in the unusual and extreme conditions of the DECADE project[113].

After a wide screening of possible candidate electrocatalysts, the only ones that result to be active for the EOR in concentrated ethanol 96% are: pure metallic Pt, PtSn bimetallic sites, PtSn and CuSn bimetallic alloys and NiCuSn trimetallic alloy.

So far, pure Pt is the most efficient metal for catalyzing the EOR[114]. However, it is an expensive material and its active sites are vulnerable to poisoning by intermediate species, especially carbon monoxide (CO), that are generated during the EOR[115]. Consequently, in this work significant efforts have been made in order to: i) finely control the morphology of Pt nanoparticles (including dimension and shape) to design catalysts with a high number of exposed catalytic sites using a low amount of Pt[116, 117] and ii) reduce the poisoning issue by the addition of Sn[118].

The exclusion of critical raw material such as Pt from the anode design would be ideal for the fabrication of an electrochemical system based on cheap and abundant materials. For this reason, after the initial selection of CuSn and NiCuSn as promising candidates for EOR, several efforts have been made to optimize their activity and stability.

These electrocatalysts, must be deposited on a carbon cloth (CC) substrate, in order to find application as anodic part in a prototype of the proposed new PEC approach. In this work, the metallic electrocatalysts were or directly deposited on CC by electrodeposition method from aqueous solution containing the metallic precursor salts following two different pathways (co-electrodeposition and sequential electrodeposition). In alternative, the electrocatalysts have been first synthetized on carbon doped sulfur (C-S) support by impregnation method and then deposited in the form of an ink on the CC substrate by spray coating. The obtained materials were characterized by structural, morphological, elemental analysis and tested for the EOR using electrochemical techniques.

3.2 Pt containing catalysts

3.2.1 Electrodeposition

The electrodeposition method has been chosen for its scalability, the possibility to finely control the morphology (size and distribution) of the deposited materials by adjusting the deposition parameters and the assurance of a strong adhesion of the coating to the CC substrate.

In this regard, two different procedures were exploited:

- The co-deposition
- The sequential deposition

The co-electrodeposition allows to synthetize a PtSn alloy in which all the surface of the catalyst is active towards the EOR. However this single-step electrodeposition procedure is complex and challenging because of the redox potentials of the two metallic elements have different values.

The sequential electrodeposition consists of two simple electrodeposition steps and leads to the formation of bimetallic sites that turn out to be sufficient to catalyse the EOR, rather than a true alloy.

3.2.1.1 Co-electrodeposition

The co-electrodeposition of PtSn on CC support was performed from an aqueous solution containing both Pt and Sn salt precursors by using a pulsed technique with 3600 s current cycling at $-$ 40 mA cm^{-2}. Specifically, the PtSn precursor solution was prepared by dissolving in water first trisodium citrate ($Na_3C_6H_5O_7$) 50 mM, then tin (II) chloride ($SnCl_2$) 2 mM and finally chloroplatinic acid hexahydrate ($H_2PtCl_6 \cdot 6H_2O$) 2 mM. It should be pointed out that these three chemical components must be added in water by following the described sequence. In fact, $Na_3C_6H_5O_7$ plays a key role in avoiding the precipitation of $SnCl_2$ in water and thus in allowing the formation of an uniform film from through electrodeposition from the as-prepared solution[119].

The XRD analysis (Figure **1a**) of the deposited material identified the presence of a $Pt_{3.6}Sn_{0.4}$ phase, the other visible peak at $\sim 25°$ and the shoulder at $\sim 44°$ are ascribed to the CC substrate. In agreement, an atomic Pt/ Sn ratio of 19/1 (Pt 95%at and Sn 5%at) was found by EDX (**Figure 1b**). Moreover, as visible by the acquisition of SEM image (**Figure 1c**),

this protocol provides an homogenous coverage of the CC support.
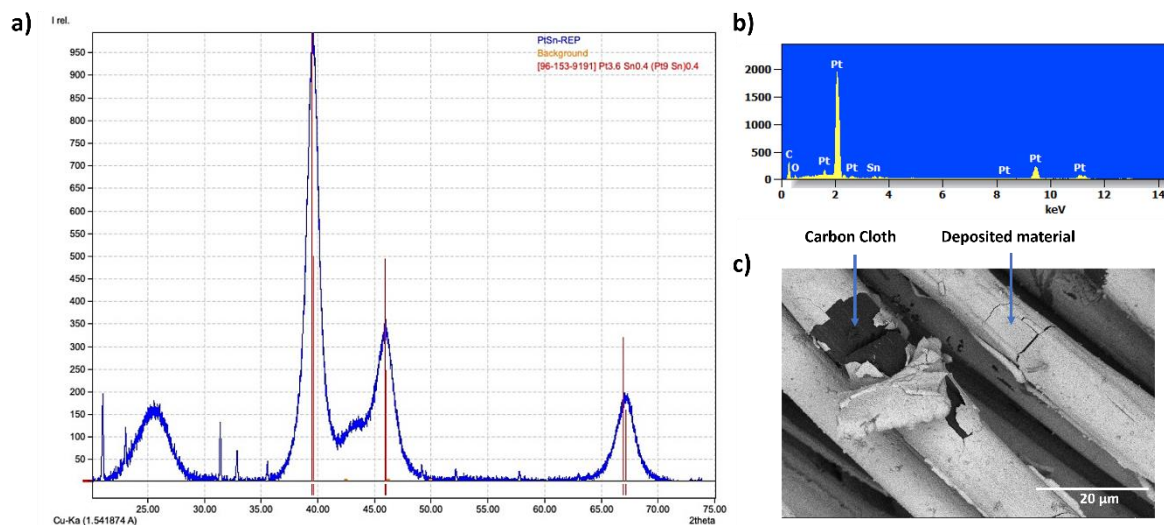
Figure1| a) XRD pattern, **b)** EDX elemental analysis spectrum and **c)** SEM image of the co-deposited PtSn alloy.

The EOR activity of the PtSn alloy supported on CC was evaluated by performing cyclic voltammetry (CV) and linear sweep voltammetry (LSV) characterizations (**Figure 2a**).

The CV and LSV were measured in a one pot container in 20 mL of ethanol 96% with LiClO$_4$ 0.2 M solution at a scan rate of 75 mV s^{-1} and 5 mV s^{-1}, respectively. The resistance was measured and corrected using the impedance spectroscopy technique. Specifically, the 85 % of the real component of the impedance measured at 100 kHz at the open circuit potential was used for the iR drop or voltage loss compensation.
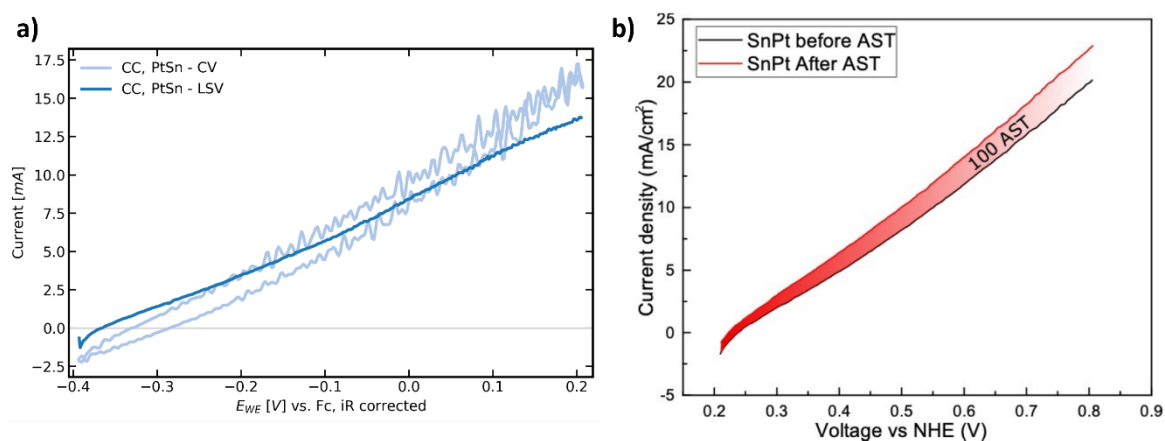
Figure 2| a) CV and LSV profiles of PtSn supported on CC in ethanol 96% with LiClO4 0.2 M at scan rate 75 mV s^{-1} and 5 mV s^{-1}, respectively, **b)** LSV accelerated stress test (AST) for the PtSn supported on CC.

As shown in **Figure 2a**, both CV and LSV profiles exhibit a high current which reaches

values of ~17.5 mA cm^{-2} and 14 mA cm^{-2}, respectively. Moreover the PtSn alloy supported on CC showed an excellent stability. Indeed, the electrode, after a LSV for 100 consecutive cycles (accelerated stress test, AST), exhibits an increase in the electrocatalytic activity (**Figure 2b**).

However, the co-deposition method is not trivial and, although promising for obtaining a true PtSn alloy with good performance and high stability, it suffers from low reproducibility. A critical factor is the stability of the electrolyte bath because of the possibility of reducing both Pt and Sn precursors to metallic Pt and metallic Sn, respectively. The values of the standard reduction potential (E°) with respect to the standard hydrogen electrode (SHE), at room temperature (25 °C) and pressure of 1 atm of the reactive species, are listed below[120]:

$$PtCl_6^{2-} + 2e^- \rightleftarrows PtCl_4^{2-} + 2\,Cl^- \qquad E^\circ = 0.68\,V$$
$$PtCl_4^{2-} + 2e^- \rightleftarrows Pt\,(s) + 4\,Cl^- \qquad E^\circ = 0.76\,V$$
$$Sn^{4+} + 2e^- \rightleftarrows Sn^{2+} \qquad E^\circ = 0.15\,V$$
$$Sn^{2+} + 2e^- \rightleftarrows Sn\,(s) \qquad E^\circ = -0.14\,V$$
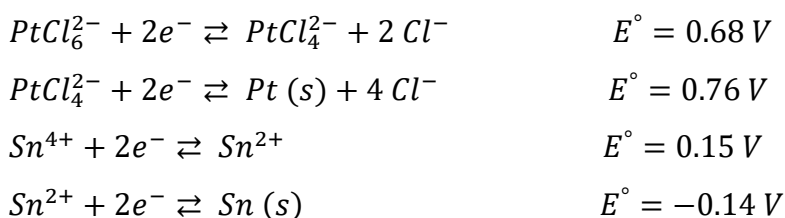
It is clear that during the co-electrodeposition process the probability of reducing Pt precursor to metallic Pt is thermodynamically favoured because of the higher E° values. For these reasons, we stopped optimizing this route and we attempted the sequential deposition in order to get a more reproducible and consistent method.

3.2.1.2 Sequential electrodeposition

A PtSn bimetallic catalytic system was prepared by firstly depositing a layer of Pt on the CC substrate and on top a layer of Sn. In this condition, the layer of Sn could completely cover and isolate the Pt active sites resulting in a catalysts with very low activity. However, we discovered that in the employed reaction medium (ethanol 96% with LiClO$_4$ 0.2 M), the metallic Sn gets corroded at the potential useful for the ethanol oxidation. As a result of this corrosion, only a tiny amount of Sn remains, which is sufficient to create the so-called bimetallic sites, *i.e.,* areas where both Pt and Sn atoms are in close proximity to each other.

The protocols followed for the electrodeposition of Pt and Sn, as well as the partial corrosion of Sn are described below.

Electrodeposition of platinum

The Pt electrodeposition on CC was carried out at room temperature with a Bio-Logic multichannel potentiostat in a one-pot three-electrodes electrochemical cell. Specifically, a CC, an aqueous Ag/AgCl electrode (3 M KCl) and a Pt mesh were employed as working electrode (WE), reference electrode (RE) and counter electrode (CE), respectively. The Pt precursor solution was prepared by dissolving sodium chloride (NaCl) 0.5 M and $H_2PtCl_6·6H_2O$ 3 mM in 20 mL of milliQ water under continuous stirring and bubbling with Ar in order to remove the oxygen. The Pt was deposited by applying 20 pulses at three different voltages, including -0.2, -0.3 and -0.4 V vs. aqueous Ag/AgCl RE for 10 s and 0.4 V for 5 s, respectively. Despite the CC is hydrophilic, it may still retain a residual hydrophobic character. This could result in regions on the surface of the CC substrate that are not sufficiently wet, commonly referred as dry spots. To avoid this issue, before the Pt electrodeposition process, it is necessary to wet the CC in a medium polarity solvent, for example methanol, ensuring in this way a homogenous deposition of the material on the substrate.

Electrodeposition and partial removal of tin

The electrodeposition of Sn was performed in a one-pot three electrodes cell in which a metallic Pt supported on CC, an aqueous Ag/AgCl (3M KCl) electrode and a Sn foil were used as WE, RE and CE, respectively. The Sn precursor solution was composed by $SnCl_2$ 0.2 M and ammonium citrate tribasic ($C_6H_{17}N_3O_7$) 0.33 M in 30 mL of milliQ water[121]. The solution was kept under an atmosphere of Ar in order to avoid the oxidation of Sn (II) to Sn (IV). Again, as already explained in the co-electrodeposition method, it is necessary to dissolve in water first the $C_6H_{17}N_3O_7$ and then $SnCl_2$[119, 122].

The Sn was deposited by applying of a sequence of -50 mA cm^{-2} per 2 ms (deposition pulse), 0 mA cm^{-2} for 17 ms (resting time) and 5 mA cm^{-2} for 1 ms (reverse current pulse) repeated for 10 minutes (3000 cycles). Depositing Sn from aqueous solution results in significant hydrogen production occurring at a lower potential than Sn deposition. Nevertheless, Sn is still deposited, albeit in small quantities. Then, most of the metallic Sn was on purpose rapidly corroded during the fabrication process by dipping the CC in KOH 1 M for one hour.

Catalyst characterization

The morphology and the elemental composition of the as-prepared catalysts were investigated by SEM and EDX analysis.

All the electrochemical tests were carried out in a one pot container in 20 mL of ethanol 96% with $LiClO_4$ 0.2 M under stirring at 600 rpm. A Pt mesh was used as CE and a non-aqueous $Ag/Ag+$ electrode filled with ethanol 96% with $LiClO_4$ 0.2 M and saturated with LiCl as RE. The medium inside the RE was kept as close as possible to the reaction medium in order to avoid the presence of junction potential or leakage of the internal electrolyte from the RE into the reaction environment. The RE was calibrated by measuring the ferrocene peaks by performing a CV from approximatively 0.2 to 0.8 V vs the reference potential at a scan rate of 100 mV s^{-1} for 40 cycles and without stirring. The measurement was performed in ethanol 96% with $LiClO_4$ 0.2 M and ferrocene 5mM by using a Pt foil as WE and a Pt mesh as CE. The ferrocene potential has been observed at 0.59 V vs our custom RE. The resistance was measured and corrected using the impedance spectroscopy technique. Specifically, the 85 % of the real component of the impedance measured at 100 kHz at the open circuit potential was used for the iR drop or voltage loss compensation.

Results

The electrodeposition technique allowed us to fine-tune the morphology of Pt nanoparticles by adjusting the electrodeposition parameters such as the cathodic potentials and the electrodeposition time. The effect of applying different cathodic potentials is shown in **Figures 3a-o** that display the SEM images of three different CC on which Pt was deposited by applying 20 pulses at -0.2, -0.3 and -0.4 V vs. aqueous Ag/AgCl RE for 10 s and 0.4 V for 5 s, respectively.

In particular, at -0.2 V smooth and globular Pt particles are uniformly distributed on the CC substrate (**Figures 3a-e**).

At more negative potentials, *i.e.,* -0.3 V (**Figures 3f-j**) and -0.4 V (**Figures 3k-o**) because as the hydrogen evolution reaction begins, the texture of Pt deposits becomes rougher. This is evident when comparing **Figure 3e**, which displays globular deposits, with **Figures 3j,o** where spiked structures are visible.

Additionally, at -0.4 V the production of hydrogen bubbles was clearly visible causing a high

heterogeneity of the Pt deposition. This non uniformity in the Pt deposition is visible comparing the low coverage in **Figure 3l** with the high coverage in **Figure 3n**.
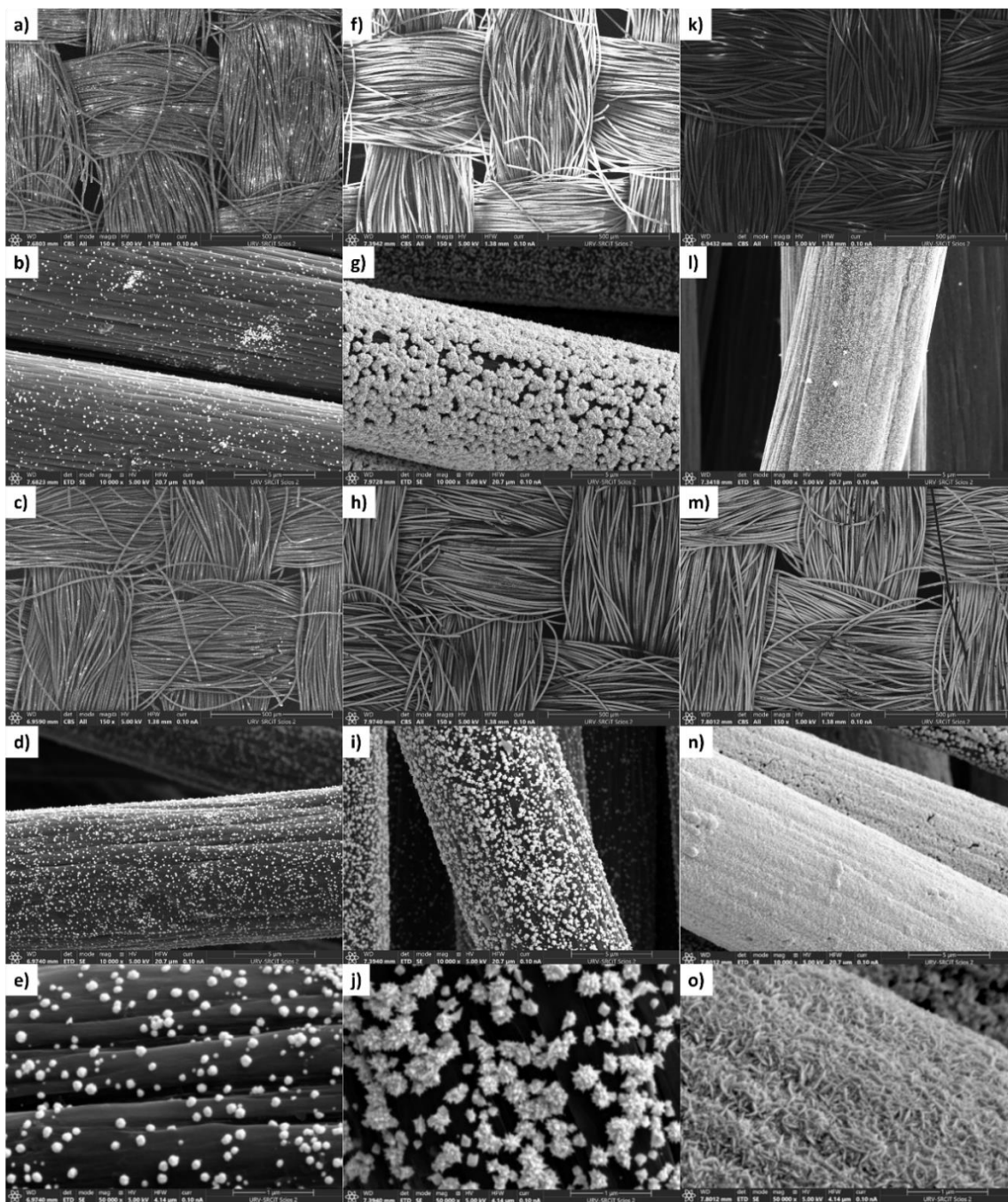
Figure 3: SEM images of Pt electrodeposited on unfunctionalized carbon cloth using pulses of different voltages: **a-e)** -0.2 V vs Ag/AgCl, **f-j)** -0.3 V vs Ag/AgCl, **k-o)** -0.4 V vs Ag/AgCl, respectively. **b)**, **g)** and **l)** Close-up images taken at the center position of **a)**, **f)** and **k)** respectively. **d,e)**, **i,j),** and **n,o)** Close-up images taken at the center position of **c)**, **h)** and **m)** respectively. The low magnification images have been taken with the backscattering detector (for highlighting the zones with and without Pt in light and dark color respectively), while the close up ones with the standard secondary electron detector (for highlighting the morphology).

The steps of Sn deposition and partial corrosion process observed at microscopic level are shown in **Figures 4b-c.** The SEM image of the same CC covered with only Pt (**Figure 4a**) is depicted as reference. In **Figures 4b-c**, together with a clear homogenous layer of Pt particles, we can observe the presence of small and dispersed gray areas indicating Sn deposits. In all the images, the black areas represent the uncoated CC.
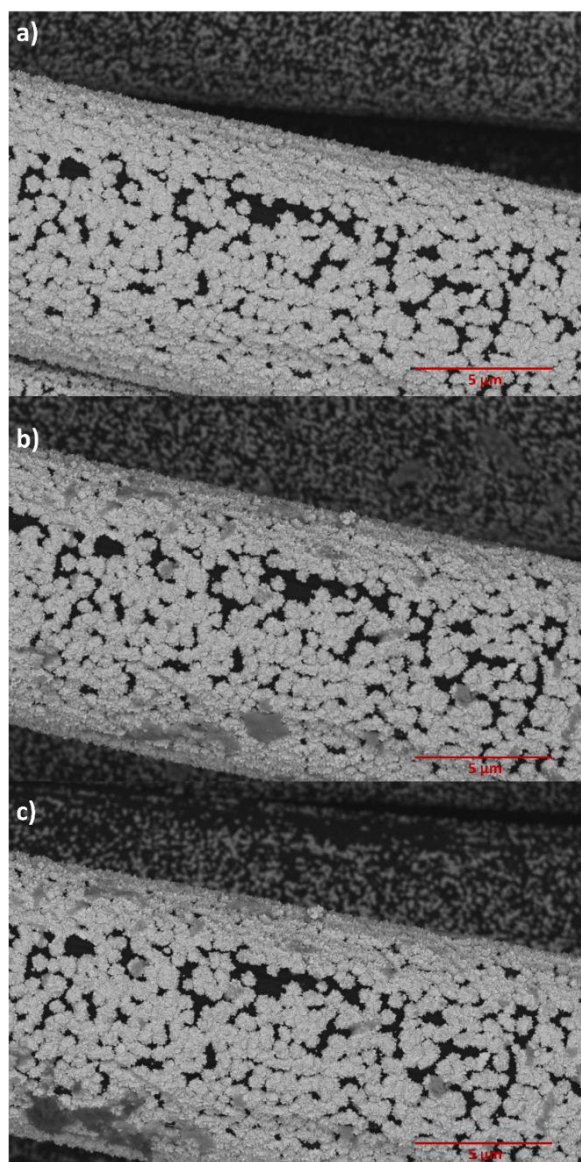
Figure 4 | SEM images of **a)** Pt deposited on carbon cloth with pulses of -0.3 V vs aqueous Ag/AgCl electrode, **b)** same zone after Sn electrodeposition from aqueous solution, **c)** same zone after the partial removal of Sn through immersion of the electrode in KOH 1 M for 1 h. A backscattering detector was used for highlighting the different composition of the material surface. The sample is the same reported in **Figure 3g.**

The EDX analysis of the PtSn layer supported on CC proved the presence of Pt and Sn both before and after the partial Sn removal (**Figures 5a,e**). Specifically, the atomic weight of Pt was 85% and 93% before and after the immersion of the electrode in KOH 1 M, respectively; while as expected, the atomic weight of Sn decreases from 15% to 7%. The EDX elemental mapping showed a homogenous distribution of Pt both before and after Sn corrosion (**Figures 5c,g**), while the distribution of Sn was lower than that of Pt in both cases (**Figures 5d,h**). Frome these observations, it is confirmed that Sn was successfully partially removed from the top of Pt.
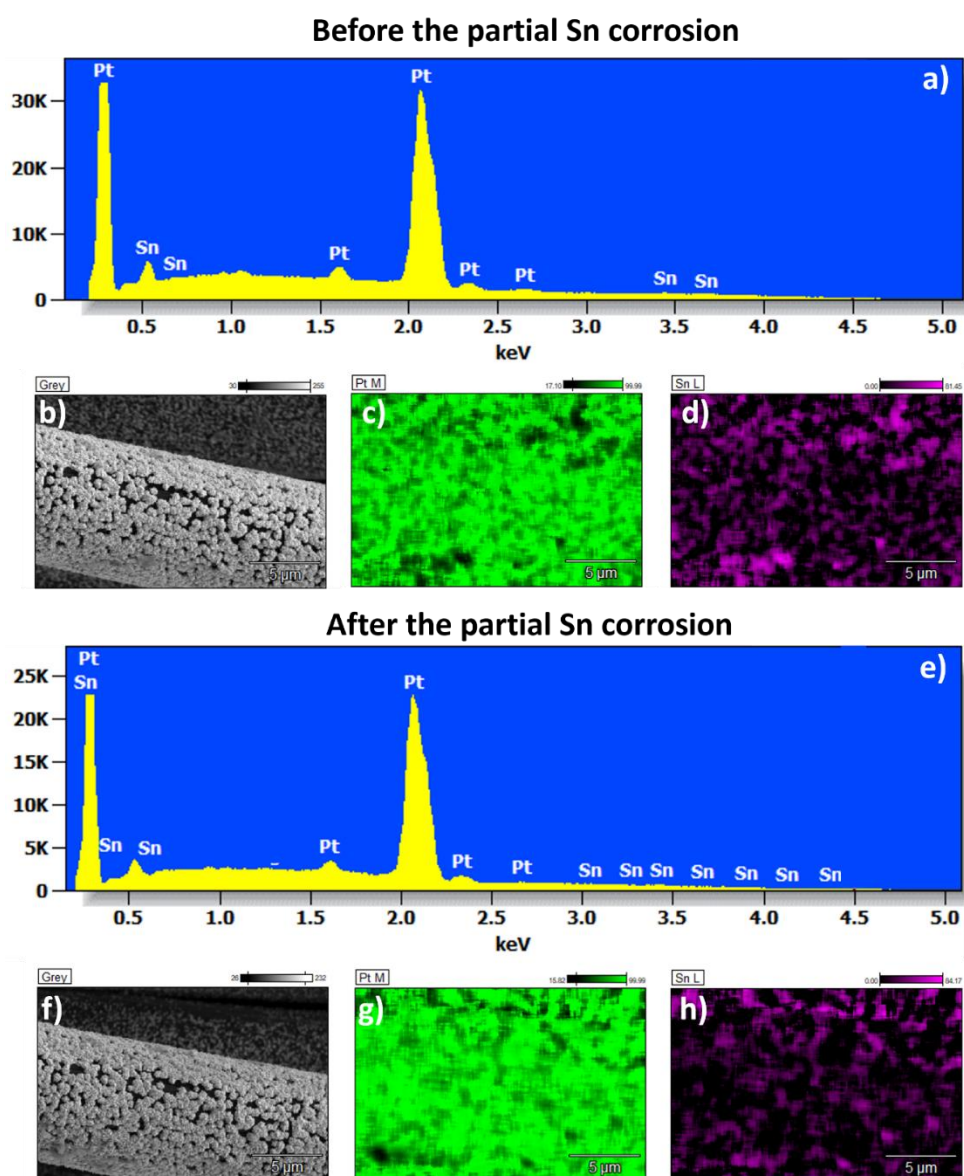
Figure 5| a) EDX elemental analysis spectrum of the PtSn alloy, **b-d)** EDX elemental mapping of **b)** PtSn alloy, **c)** Pt and **d)** Sn; before partial Sn removal. **e)** EDX elemental analysis spectrum of the PtSn alloy, **f-h)** EDX elemental mapping of **f)** PtSn alloy, **g)** Pt and **h)** Sn; after partial Sn removal.

Moreover, the robustness of the Pt electrodeposition process was demonstrated by using the SEM technique (**Figures 6a,b**). As shown in **Figure 6b**, the electrodeposited Pt remains perfectly attached to the CC substrate even after several processes (including ultrasonication, Sn electrodeposition, Sn corrosion and EOR activity testing). The SEM image of the same CC with only the fresh electrodeposited Pt (**Figure 6a**) is displayed as reference. The black areas in both images represent uncovered CC, the spiked clear deposits are Pt particles and the gray zones in **Figure 6b** are Sn deposits.
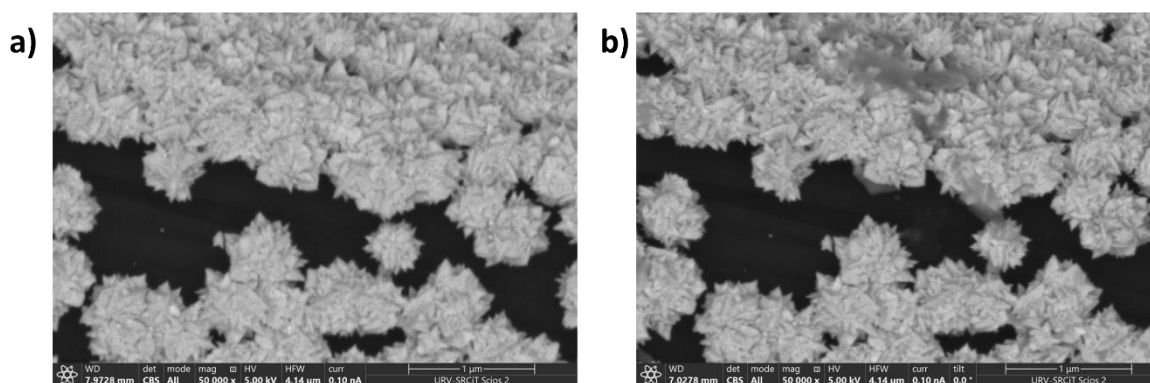
Figure 6| SEM backscattered electron images of electrodeposited Pt a) as prepared and b) after several processes.

The activity of the electrodes was measured after each fabrication step, including after Pt deposition, after Sn deposition and after Sn partial removal by performing CV and CA measurements

The CV curve were recorded from -0.1 to 0.6 V vs our custom RE at 100 mV s^{-1} for 20 cycles in order to assess the stability of the system. In the following results it is reported only the last cycle. The CA test has been performed by applying a series of steps at specific potential level of 0.2, 0.3, 0.4 and 0.5 V for 2 min and a last step at 0.6 V for 10 min. Prior to each step, a cleaning pulse of -0.1 V was applied for 5 s. The whole protocol has been repeated many times in order to certify the stability of the electrode.

Figure 7 shows the comparison of the CA profile of three different electrode with Pt deposited with voltages pulses of -0.2, -0.3 and -0.4 V vs. Ag/AgCl.
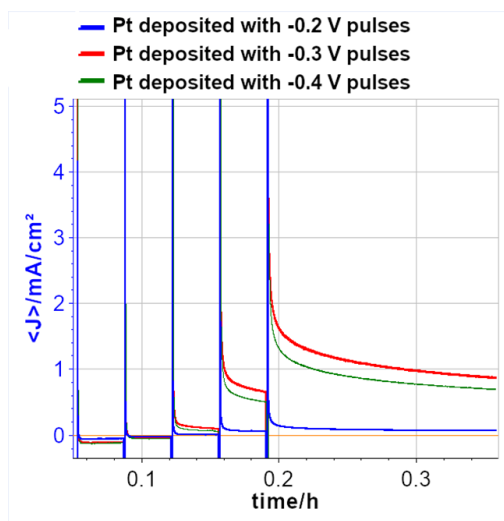
Figure 7| Chronoamperometry of the Pt electrodeposited NPs at different voltages.

It is evident that the electrode with Pt deposited at intermediate voltages exhibits the best activity. For this reason the Sn deposition and partial removal procedure described in this work were optimized on a Pt electrode prepared in this condition.

Figures 8a,b compare the electrode activity towards EOR of the electrode after the Pt electrodeposition (green line) and after the deposition and partial removal of Sn (blu line)- The activity of the bare CC support is also shown as reference. As expected, because of the formation of PtSn bimetallic sites the activity of the electrode is strongly enhanced.
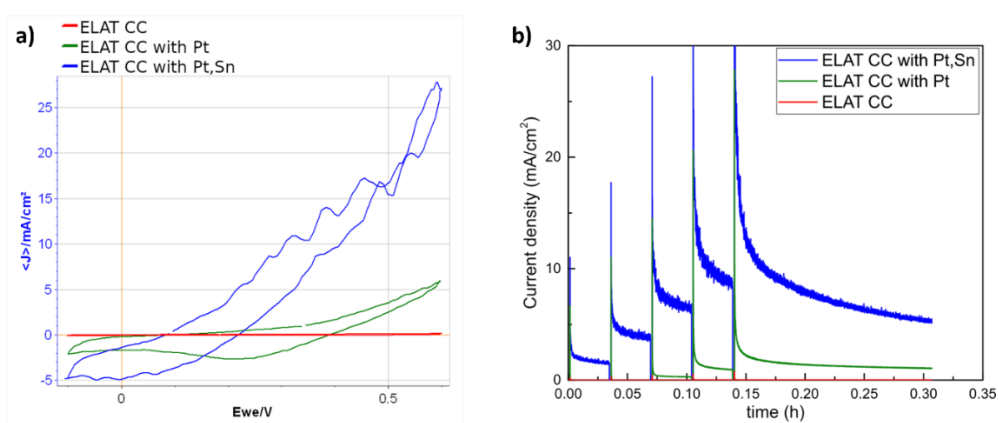
Figure 8| Comparison of the EOR activity of the CC substrate in its pristine form, after Pt deposition and after Sn deposition and partial corrosion. **a)** Stabilized CV profile measured at 100 mV s^{-1} in ethanol 96% with LiClO4 0.2 M, **b)** CA with stepped potentials.

3.2.2 <u>Impregnation</u>

As alternative to the co-electrodeposition method, we tried to synthetized a true PtSn alloy by impregnation method on C-S support by following a procedure already present in literature[123]. Specifically, H_2PtCl_6 and $SnCl_2$ (used as metal salt precursors of Pt and Sn, respectively) were mixed in 50 mL of deionized water and loaded in 50 mg of C-S support. The total metal loading was 20 wt%. The mixture was stirred for 6 h and dried at 60° C in vacuum. Finally, the dried powder was subjected to a thermal reduction treatment in H_2 (10% in Ar) atmosphere at 900° C for 6 h. Considering the last step of thermal reduction, on a common C support the high temperatures required for the formation of a highly ordered PtSn nanoparticles structure, inevitably accelerate the metal sintering, producing a material with poor crystallinity and low surface area. However, in this case the strong interaction between Pt and S suppresses the metal sintering process. Then, the as-prepared catalysts, were deposited in the form of an ink on the CC support by using the spray coating technique.

Results and discussion

The SEM image of the C-S support impregnated with PtSn is displayed in **Figure 9.** It can be observed that small metallic particles with a diameter <100 nm (the white dots in **Figure 9**) are well attached on the S-C substrate.
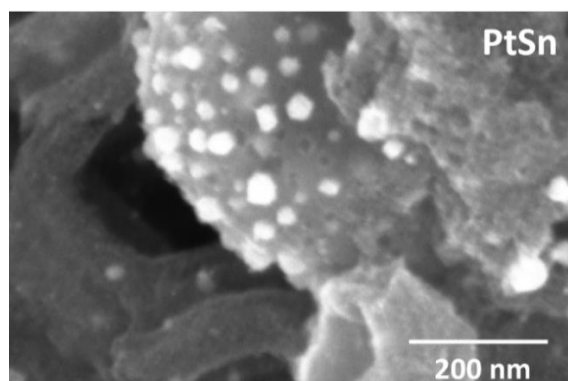
Figure 9| FESEM images of the PtSn alloy synthetized by C-S impregnation method.

The CV for the assessment of the activity towards the EOR of this PtSn electrocatalyst catalysts was performed in concentrated ethanol 96% with $LiClO_4$ 0.2 M. As shown in **Figure 10a**, the PtSn compound exhibits high performances with a current density reaching remarkably 30 mA cm^{-2} at 1.2 V vs NHE. Moreover, a CA was carried out at 1 V vs NHE

for 5 h (**Figure 10b**). We can observe that the current density is very low ~ 1.4 mA cm^{-2} and after an initial drop of about 64% reaches a value of 0.3 mA cm^{-2} that is maintained until the end of the test. These electrochemical characterization results suggest that the PtSn alloy synthetized by S-C impregnation method is a promising catalyst for the EOR, but maybe a higher metal loading is necessary to improve its performance.
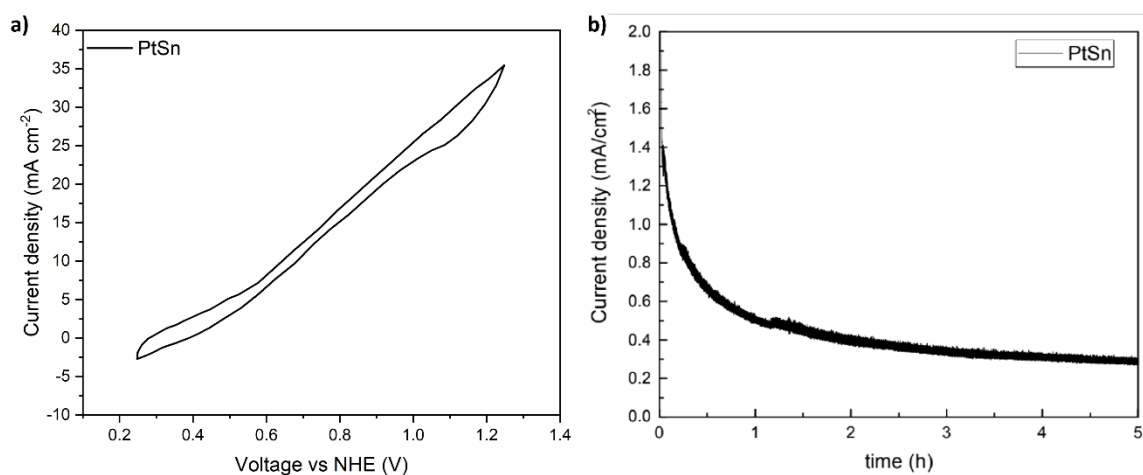
Figure 10| a) CV profiles and **b)** CA measurement at 1.0 V vs. NHE for 5 h of PtSn alloy synthesized by the S-C impregnation method.

3.3 <u>Non Pt containing catalysts</u>

3.3.1 <u>Electrodeposition</u>

An effective alloy based on non-PGM elements has been obtained by co-electrodeposition pulsed technique, from a solution containing both the desired metallic soluble precursors. Specifically, the CuSn alloy precursor solution was obtained by dissolving 12 mM of metallic chlorides in an aprotic solvent (a mixture of Dimethyl sulfoxide-DMSO and Acetonitrile-ACN) with the adding of LiClO$_4$ 0.2 M as electrolyte. The electrodeposition was performed by using a CC as WE, a carbon rod as CE and a saturated calomel electrode (SCE) as RE. The protocol followed for the electrodeposition involved the application of different cycles (450, 900 and 1800, respectively) of pulses of -2.1 V vs SCE for 0.5 s using a potentiostatic mode. After the electrodeposition process, the electrodes were rinsed in ethanol and dried at 60°C.

Using this methodology, we synthetized several catalysts with concentration of the two

metallic centers (*i.e.,* Sn and Cu) such as $Sn_{0.17}Cu_{0.83}$, $Sn_{0.34}Cu_{0.66}$, $Sn_{0.5}Cu_{0.5}$, $Sn_{0.67}Cu_{0.33}$, $Sn_{0.84}Cu_{0.16}$ and $Sn_{0.17}Cu_{0.83}$.

Additionally, we synthesized a trimetallic alloy by adding Nickel (Ni) with the aim of harnessing the synergy among the metals to boost the performances of the electrode. We chose to include Ni because it tends to undergo oxidation during the reaction, a factor that we believe can be useful in improving the activity of the catalyst.

Characterization

The following discussion is focused on the morphological and elemental characterization (**Figures 11a-g**) of the $Sn_{0.67}Cu_{0.33}$ compound as a representative sample for its superior performance during EOR (**Figure 14**), as shown in the following section.
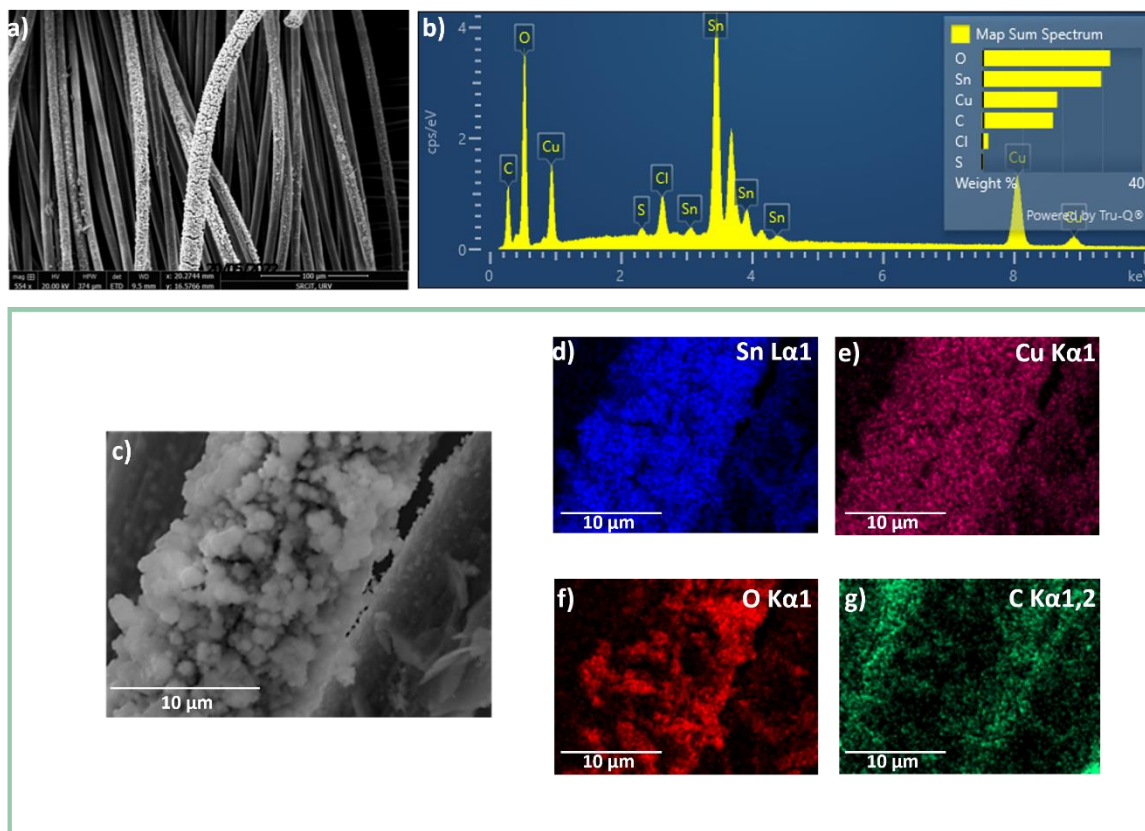
Figure 11| a) SEM electron microscopy and **b)** EDX elemental analysis spectrum of a $Sn_{0.67}Cu_{0.33}$ layer on carbon cloth, obtained by electrodeposition in aprotic medium, **c)** close up FESEM of the same sample, **d-f)** EDX elemental analysis mapping of the $Sn_{0.67}Cu_{0.33}$ alloy: **d)** Sn, **e)** Cu, **f)** O and **g)** C.

The SEM image (**Figure 11a**) shows that the CC substrate is uniformly covered by the electrodeposited material. Thee EDX spectrum (**Figure 11b**) confirmed the presence of

expected elements, *i.e.,* Sn and Cu with a weight percent of ~ 30 and 20 wt%, respectively. **Figure 11c** shows a close up SEM image of the decorated CC with the $Sn_{0.67}Cu_{0.33}$ alloy, revealing a rough surface characterized by aggregates of globular particles. Moreover the EDX elemental mapping reveals a uniform distribution of Sn and Cu together with other elements (C and O) on the CC support (**Figures 11d,e**).

Regarding the morphological characterization of the NiSnCu alloy, the SEM image (**Figure 12a**) displays a nodular surface with well-defined boundary between the nodules. The EDX elemental analysis spectrum (**Figure 12b**) confirmed the presence of the predicted component of the alloy, *i.e.,* Ni, Cu and Sn with the weight percent of ~ 10, 20 and 20 wt%, respectively.
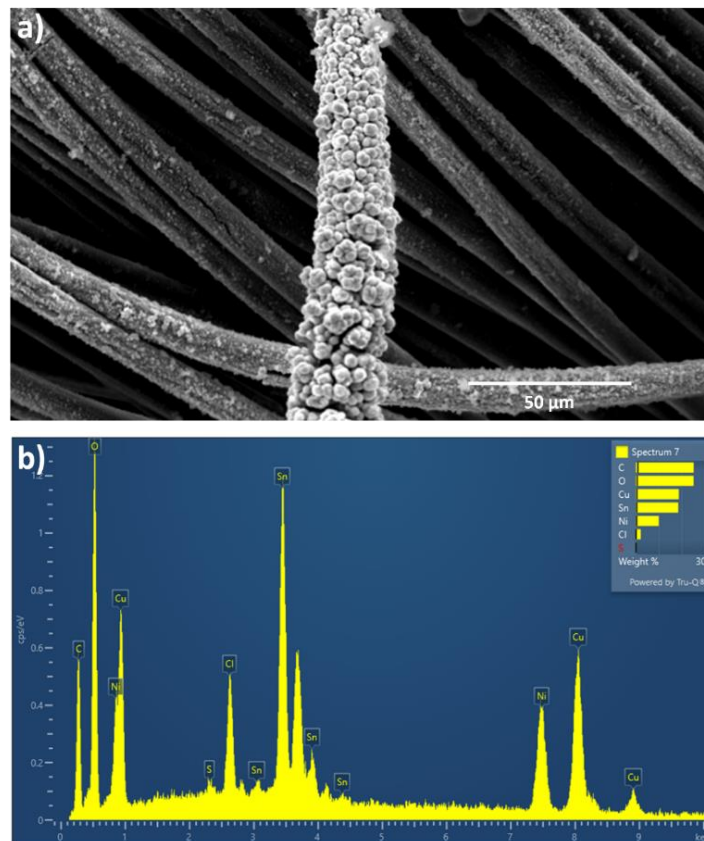
Figure 12| a) SEM image and **b)** EDX elemental analysis spectrum of a carbon cloth decorated with NiSnCu particles.

Information about the microstructure of both $Sn_{0.67}Cu_{0.33}$ and NiSnCu coating have been obtained by recording the XRD patterns (**Figure 13**).
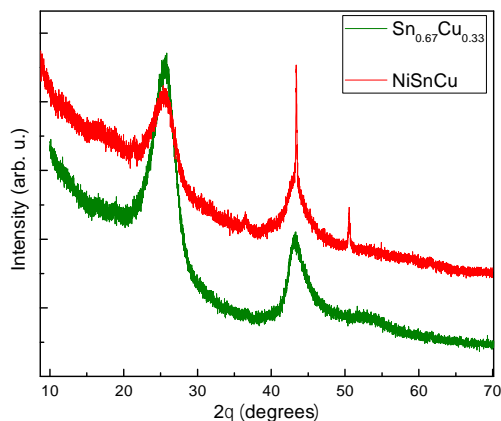
Figure 13| XRD pattern of a carbon cloth covered by $Sn_{0.67}Cu_{0.33}$ compound (green line) and NiSnCu (red line).

We can observe the presence of two main broad peaks at 25° and 44° associated to the CC support. Specifically, in the case of the $Sn_{0.67}Cu_{0.33}$, there are no distinct characteristic diffraction peaks, but rather a wide distribution between 50 and 60° and a small distribution around 35°. We believe that the signals from the alloy are hidden by the broad distributions from the CC substrate. Instead, the XRD pattern of the NiSnCu exhibits some typical diffraction peaks at the same angle as those of the CC support.

Results

Every electrode was evaluated for the EOR by performing CV measurements (**Figure 14**). The CV profiles were recorded from 0.2 to 1.4 V vs. NHE in ethanol 96% using $LiClO_4$ 0.2 M as electrolyte, a carbon rod as CE and a saturated calomel electrode as RE.
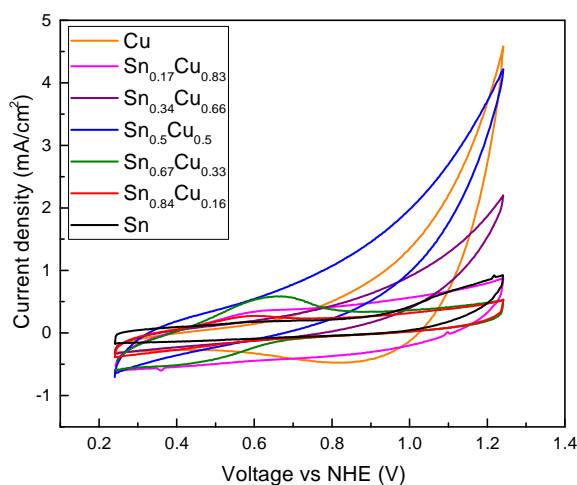
Figure 14| Stabilized cyclic voltammograms for several SnCu alloys synthetized with different concentration of the two metallic centers (Sn and Cu) measured in ethanol 96% with $LiClO_4$ 0.2 M.

We observe some catalytic waves in the range between 0.6-0.7 V vs NHE, that are related with ethanol oxidation ($E° = 0.66$ V vs NHE). This signal is more evident in the case of the $Sn_{0.67}Cu_{0.33}$ compound which maybe is more selective to the EOR. However, this electrode exhibits a very low current density of 0.34 mA cm^{-2} at 1 V vs NHE (**Figure 15a**). In addition, the CA test performed at 1.24 V vs NHE and conducted over 2 h reveals some deactivation effects already visible in the first 30 minutes (**Figure 15b**).
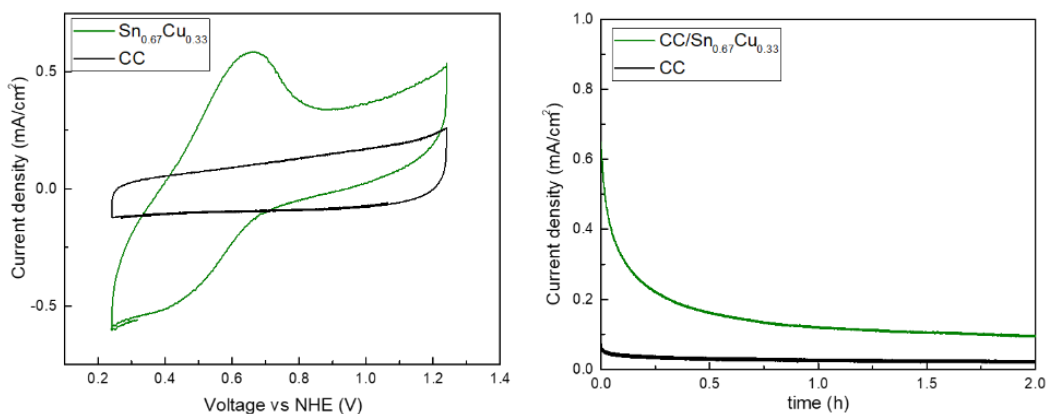
Figure 15| a) CV profile and **b)** CA stability test at 1.24 V vs NHE of the $Sn_{0.67}Cu_{0.33}$ supported on CC.

Considering the underperformance of the SnCu alloys and potential degradation effects during the EOR, we believed that the addition of Ni would be beneficial in preventing poisoning and deactivation during the oxidation process. Using different number of cycles during the electrodeposition we modulated the nanoparticle size and coverage of the CC support. **Figure 16** illustrates how these two variables significantly affect the performance of the EOR.
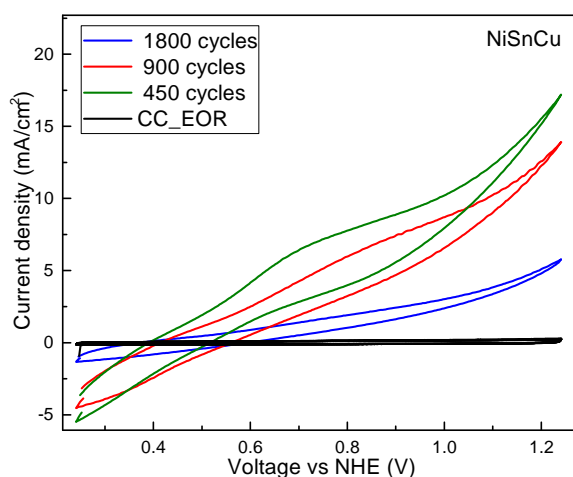
Figure 16| CV profile of the NiSnCu alloy electrodeposited on CC by applying different number of cycles.

The electrode realized by applying 450 cycles exhibits the best performances. This highlights how the combined effect of depositing small particles and the synergy between Ni and SnCu enhances the efficiency of the electrodeposited material during the EOR.

3.3.2 <u>Impregnation</u>

Bimetallic and trimetallic alloys based on non-critical raw materials such as CuSn and CuNiSn have been synthetized by C-S impregnation method following the same procedure described in section **3.2.2**.

<u>Results and discussion</u>

Figures 17a,b present the morphological characteristics of the CuSn and NiCuSn catalysts prepared by C-S impregnation method as analysed by SEM. Both catalysts show a fairly similar distribution of small metal particles (less than 100 nm in diameter) that have adhered well to the C-S support.
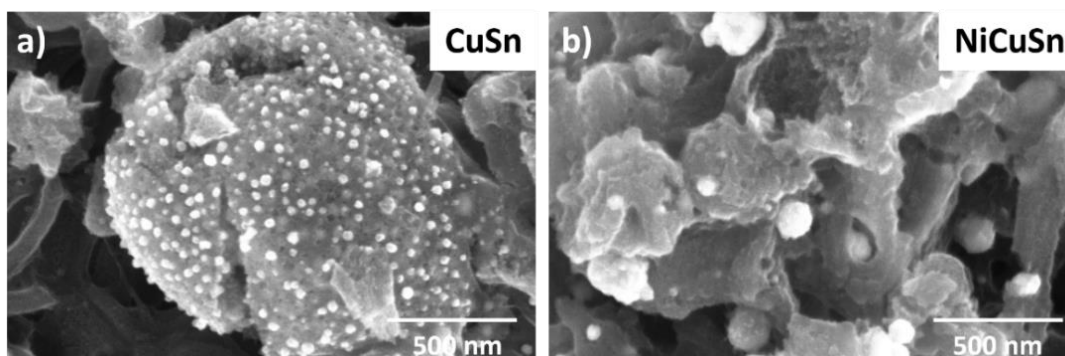
Figure 17| SEM images of the **a)** bimetallic CuSn and **b)** trimetallic NiCuSn alloy synthetized by C-S impregnation method.

The possible employment of these CuSn and NiCuSn catalysts for the EOR has bee assessed by performing CV measurements (**Figure 18**).
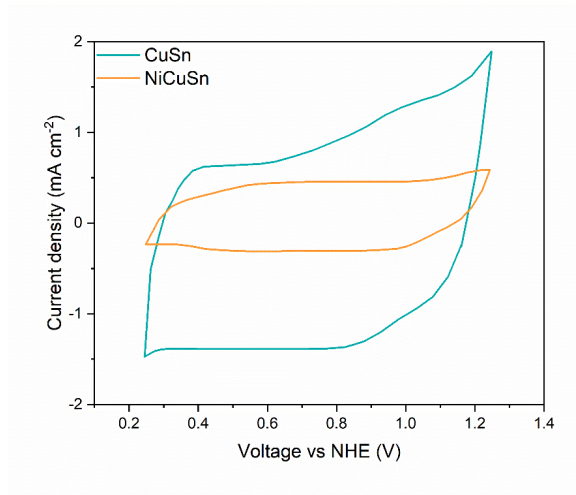
Figure18| CV profiles of bimetallic CuSn and trimetallic NiCuSn alloys synthesized by the C-S impregnation method.

In both cases, the current density was very low suggesting a negligible catalytic activity for EOR. Thus, the CuSn and NiCuSn catalysts synthetized by C-S impregnation method are not promising to carry out the EOR.

3.4 <u>Conclusions</u>

In summary, this work concerns the synthesis of a good catalysts with high activity and stability to carry out a selective ethanol oxidation reaction (EOR) in an uncommonly used electrolyte, *i.e.,* concentrated ethanol (96%). Specifically two different approaches, *i.e.,* electrodeposition and impregnation method on carbon doped sulfur (C-S) support were used to fabricate PtSn, CuSn and NiCuSn electrocatalysts in the form of bimetallic and trimetallic alloys or bimetallic active sites. Our results show that the PtSn electrocatalyst is the best candidate for realizing the EOR. In more detail, regarding the electrodeposition of PtSn, we followed two different protocols, the co-electrodeposition and the sequential electrodeposition. The co-electrodeposition of PtSn is very promising for obtaining the target alloy, but with low reproducibility due to the instability of the electrolytic deposition bath. Therefore, in order to get a more reproducible and consistent electrodeposition method, we attempted and optimized the sequential electrodeposition. The deposition of Pt was followed by the deposition and partial removal of Sn in order to create the so-called bimetallic sites, *i.e.,* areas where both Pt and Sn atoms are in close proximity to each other. The validity and

efficiency of this deposition method was confirmed by measuring the activity towards the EOR after each Pt and Sn deposition and Sn partial removal step. The enhanced activity after the partial removal step of Sn confirmed the successful formation of PtSn bimetallic sites. As an alternative to the co-electrodeposition we synthetized a true PtSn alloy by C-S impregnation method. In this case, despite the promising results, in order to obtain a highly performing and stable electrode the synthesis protocol must be optimized. As an alternative to PtSn, we have fabricated and tested the activity towards the EOR of bimetallic and trimetallic alloys based on non-critical raw materials. Both CuSn and NiCuSn alloys made by co-electrodeposition show encouraging activity towards the EOR but are less performing compared to PtSn. Moreover, also for these materials, due to reproducibility issues arising during the electrodeposition process, we tried to obtain a good catalyst by using C-S impregnation method. In this case, the catalitic activity towards EOR was very low, suggesting that the as-prepared CuSn and NiCuSn alloys are not good catalyst.

The analysis of the oxidation products of these samples is still in progress as well as the study of strategies to improve the performances and stability of these catalysts.

General Conclusion

This PhD thesis deals with two different projects about the improvement of the performance of two energy related reactions, that are the hydrogen production from water and the ethanol oxidation reaction (EOR).

In the first project, we aimed to shed light on a crucial aspect, generally not considered in the context of water splitting reaction, *i.e.,* the impact of the organization of water molecules on the semiconductor photocatalytic activity.

The behaviour of water is intimately interconnected to its hydrogen (H)-bond network[124, 125], which is characterised by a dynamic equilibrium where H-bonds break and reform cooperatively across water clusters[126]. When water establishes H-bonds with the surface of a material, this dynamic equilibrium and the average nature of water clusters change, influencing solvent reorganisation properties that, in turn, affect the rate of outer-sphere electron transfer according to Marcus theory and derived models[127]. Doping alters the interaction of water with a surface, potentially affecting the water's nature at the interface and the outer-sphere electron transfer. Despite their manifest relevance, these aspects have not been investigated in relation to water-splitting reactivity.

In this study, we designed an undoped and a B (1%)-doped TiO_2 (anatase)-based photocatalysts. The latter exhibited a five-fold enhancement in water-splitting activity compared to pure TiO_2. We used various characterisation techniques, including UV-visible diffuse reflectance, XRD, micro-Raman spctroscopy, XPS and SEM-EDX, to rule out that bandgap changes, creation of heterojunctions or heterophases, and alterations in crystal facets, nanomorphology, or nanodimension are responsible of the improved photocatalytic properties of B-TiO_2.

Additional electrochemical characterizations, including cyclic voltammetry (CV), chronoamperometry (CA) and electrochemical impedance spectroscopy (EIS), as well as steady-state photoluminescence (PL) measurements, were conducted to exclude enhanced charge separation, charge stabilization, and the creation of intermediate states as potential reasons for the improved properties of B-TiO_2. By performing Fourier Transform Infrared (FTIR) spectroscopic measurements under controlled relative humidity conditions, we demonstrated that the different water splitting activity of the investigated samples is

exclusively linked to a different water structure on their surface. Specifically in the B-TiO$_2$ sample, the water molecules are mainly organized in single H-bond donor-acceptor state, that is favourable for the water splitting reaction.

State-of-the-art spin-polarized Density Functional Theory molecular dynamics (DFT-MD) simulations were also performed to examine the water chemisorption at the surface of the titania samples, confirming the found experimental results. Indeed the simulation results show that B atoms do not chemisorb water; instead they reduce the amount of Ti$_{cus}$ sites (which commonly act as water absorption sites), inducing a slightly hydrophobic character on the titania surface, which is typically hydrophilic.

In conclusion, our study unequivocally demonstrates that the nature of water at the interface influences water-splitting performance. The water layer's nature at the interface is contingent on its H-bonding with the semiconductor surface, and doping influences this aspect. Understanding the impact of the surface in selecting specific H-bond motifs in the local water environment and its impact on electron transfers is vital for designing improved photocatalysts for water splitting.

The design of an highly performing electrocatalyst to realize the selective ethanol oxidation reaction (EOR) was the goal of second project discussed in this PhD thesis. This is a work package of the European Project DECADE (DistributEd Chemicals And fuels production from CO$_2$ in photoelectrocatalytic Devices) aiming to develop a new photoelectrochemical (PEC) cell for the conversion of CO$_2$ avoiding the water oxidation as anodic reaction. Namely, this device uses waste CO$_2$ and bio-ethanol as inputs to selectively produce the same product (*i.e.,* ethyl acetate) at both electrode sides.

Notably, in order to push the selectivity toward the ethyl acetate and increase the production rate, the reaction is carried out in extreme conditions (concentrate ethanol 96%). Due to this non common working requirement, the fabrication of the anodic side of the PEC cell is challenging.

Firstly, a wide screening of electrocatalysts generally working in aqueous solution has been made and only pure metallic Pt, PtSn bimetallic sites, PtSn and CuSn bimetallic alloys and NiCuSn trimetallic alloy were selected owing they were found to be active towards the EOR in our reaction medium (concentrated ethanol 96%).

As second step, these electrocatalysts were or directly deposited on carbon cloth (CC) substrate or synthetized by impregnation method on carbon doped sulfur (C-S) support and then tested for the EOR.

Among them the PtSn electrocatalyst realized by electrodeposition was found to be the most promising for the selective EOR, showing the highest efficiency and stability.

Nevertheless, the CuSn and NiCuSn alloys despite their low performances compared to PtSn electrocatalysts, are worthy to be considered because made with cheap and abundant materials. For this reason, different chemical and physical protocols will be investigated in the next future to improve their activity and stability.

Appendix

A1 <u>Photocatalysts synthesis</u>

Pristine and B-doped TiO_2 nanoparticles were synthesized through sol-gel method using tetrabutyl titanate (TBT) and boric acid (H_3BO_3) as precursor of titanium and boron, respectively. In the synthesis process, 12 ml of TBT was dissolved into 24 ml of ethanol (EtOH) to form a uniform solution. Subsequently, 0.5 g of polyethylene glycol with the molecular weight of 200 (PEG 200) was added to the solution under magnetic stirring at room temperature to obtain the sol. The obtained sol was continuously stirred for 2 h and aged for 96 h to form the gel. Then, the resulting gel was transferred in an autoclave and hydrothermally treated at 180 °C for 10 h to remove volatile solvents. Finally, the powder thus produced was calcined at 350 °C for 10 h. The B-doped TiO_2 sample was also synthesized by following the same the same procedure but with the addition of 3.1 g of H_3BO_3 in the precursor solution.

A2 <u>Set-up for photocatalytic water splitting test</u>

The photocatalytic-assisted water splitting tests were performed in a Pyrex photoreactor equipped with a quartz window for the irradiation of a photocatalytic area of about 10 cm^2. First of all, blank tests (without catalyst or light irradiation) were performed in order to ensure that the produced H_2 derives exclusively from the photocatalytic process. Then, 90 mg of sample were suspended into 150 ml of distilled water solution at normal pH under continuous stirring. The test were carried out at room temperature and normal atmospheric pressure. Before the testing, the oxygen and CO_2 dissolved in water were removed by flowing for 30 min with Ar as inert gas. After this initial pretreatment, the suspension was illuminated using a solar simulator (ORIEL, Xe-arc lamp, 300 W). The light source was equipped with lenses for collecting and focusing the light beam and a water filter to eliminate the infrared radiation. Moreover, the incident irradiance (i.e., the light energy incident to the photocatalyst surface) was measured by a spectroradiometer (Lot Oriel, model ILT950) and adjusted 1 SUN (100 mW cm^{-2}) by varying the distance of the photoreactor from the lamp. The rats of H_2 and O_2 production were monitored, every 4 min, by a Gas Chromatograph (MicroGC GCX Pollution Analytic Equipment) having a sensitivity of 1-2 ppm. After the

testing, the photocatalyst particles were separated by filtration and the water solution was analysed by atomic absorption spectroscopy to keep track of the eventual leaching yield of Ti or B. Finally, Then, after a drying procedure, the recovered photocatalyst was analysed to monitor any possible modifications and tested again to verify the reproducibility of the water splitting performances.

A3 Characterization techniques

A3.1 Uv-vis Diffuse Reflectance Spectroscopy

UV–vis Diffuse Reflectance Spectroscopy measurements were performed by a Thermo Fisher 220 Spectrophotometer equipped with an integrating sphere for solid samples, using barium sulfate ($BaSO_4$) as the reference and in air.

A3.2 X-ray diffraction

X-ray diffraction (XRD) analysis were done using a Bruker D2 Phaser diffractometer equipped with a Ni β-filtered Cu-kα radiation source (λ=1.54178 Å), operating at 30 kV and 10 mA. The data were collected in the 2θ range between 10° and 90° at a scanning rate of 0.04° s^{-1}.

A3.3 Micro-Raman Spectroscopy

Micro-Raman measurements were carried out using a LabRam HR800 Horiba spectrometer equipped with a confocal microscope and a liquid nitrogen cooled charge coupled device (CCD) detector. The spectra were acquired in the range between 30-800 cm^{-1} at room temperature and using a 1800 gr/mm diffraction grating. The samples were excited using a laser beam with a wavelength of 532 nm that was focused by a 50 X microscope objective. The applied laser power density was of 10 mW in order to avoid laser-induced thermal degradation or phase transitions of the TiO_2 samples.

A3.4 X-ray photoelectron spectroscopy

X-ray photoelectron spectroscopy (XPS) analysis was performed using a PHI Versa Probe II (Physical Electronics) equipped with an Al Kα (1486.6 eV) X-ray source with a beam size of 100 microns and operating at 25 W. The survey spectra were recorded with an analyser

energy path of 117 eV, while the O 1s, Ti 2p and B 1s core levels were collected at a passing energy of 23.5 eV. Prior to detecting the spectra, a charge neutralisation operation was performed by simultaneously irradiating the samples with a low-energy electron beam and an ion beam. The graphitic Carbon peak (284.80 eV) was used as reference for the position of the XPS peaks. Data analysis, including XPS peaks deconvolution and the background correction with the Shirley method, was carried out using the Multipack Data Reduction software (ULVAC-PHI, Inc).

A3.5 <u>Scanning Electron Microscopy and Energy Dispersive X-ray</u>

Scanning electron microscopy (SEM) images were acquired using a Phenom ProX Scanning Electron Microscope. An Energy Dispersive X-Ray Spectrometer (EDX) is also used to provide semiquantitative information of elemental composition.

A3.6 <u>Nitrogen physisorption</u>

Nitrogen (N_2) physisorption measurements at cryogenic temperature (-196°C, temperature of liquid nitrogen) were carried out by using an Autosorb IQ3 sorption analyser (Quantachrome). Before each textural analysis, the samples were outgassed for four hours under vacuum at ~ 573 K. The specific surface area (SA_{BET}) was determined by the Brunauer-Emmett-Teller (BET) method. The pore distribution, including total volume (V_{pore}) and diameter (D_{pore}), was assessed at a relative pressure (P/P_0) of 0.95 according to the Barrett-Joyner-Halenda (BJH) method using the desorption branch.

A3.7 <u>Photoelectrochemistry</u>

The electrochemical behaviour of TiO_2 and B-doped TiO_2 photocatalysts was valuated by performing cyclic voltammetry (CV), chronoamperometry (CA) and electrochemical impedance spectroscopy (EIS) analysis. For those tests, the photocatalysts were deposited on a conductive carbon-based gas diffusion layer (GDL, Sigracet 29 AA). In detail, a proper amount of TiO_2 (to achieve a final loading on the GDL of 1 mg cm^{-1}) was mixed with 25 mL of isopropanol and 50 μL of Nafion 10 wt% perfluorinated solution and sonicated until the formation of a stable solution (20 min). The produced ink was then deposited by spray-coating technique onto the heated (~ 80 °C) GDL to allow the evaporation of the organic solvent and uniformly fix the photocatalyst on the carbon-based substrate.

These measurements were carried out by using a home-made electrochemical cell (made of Pyrex) working for in a three electrode configuration. A quartz window allows allows the transmission of the light generated by a solar simulator (300 W Xe arc-lamp, Lot-oriel) and so the irradiation of the photocatalysts. The system was adjusted to work at 1 SUN (100 mW cm^{-2}) as described in the **Appendix A2**. Specifically, the TiO_2-based catalysts acted as the working electrode (WE, square dimension of 2 x 4 cm), a Pt wire as the counter electrode (CE) and an Ag/AgCl (3 M KCl) electrode (supplied by Amel) as the reference electrode (RE). A regular low flow (5 mL min^{-1}) of inert gas (N_2) was introduced into the cell to remove the oxygen. All the electrochemical characterizations were performed at room temperature in 1 M KOH aqueous solution using a potentiostat/galvanostat (Autolab Pgstat 204) as voltage supplier. All the applied potential values vs. Ag/AgCl electrode were converted into voltages referred to the reversible hydrogen electrode (RHE) according to the following equation:

$$E_{(RHE)} = E_{(Ag/AgCl)} + 0.059 \text{ pH} + 0.21 \tag{1}$$

In detail, the CV curves were recorded without and with illumination, at applied potentials ranging from 0.036 to 2.036 V vs RHE with a scan rate of 10 mV s^{-1}. The CA profiles were collected by performing six ON/OFF cycles of 30 seconds for each at an applied potential of 1.136 V vs RHE. Moreover, three different filters (AM 1.5 G, UVC and UVB/C blocking filters, **see Table A1**) were applied to evaluate the response of the TiO_2-based photoelectrodes in specific wavelength regions.

Type of blocking filter	Cut-off wavelength regions
AM 1.5 G	Direct light and diffused light by the atmosphere when the sun is at a zenith angle of 48°
UVC	280-4400 nm
UVB/C	320-480 nm, 700-4440 nm

Table A1| Light blocking filters with relative cut-off wavelength regions.

Finally, the EIS measurements were carried out with and without light irradiation in the frequency range from 10^5 to 0.1 Hz with an amplitude of 0.01 V_{RMS} with an applied potential ranging from 1.313 to 2.113 V vs RHE.

For all the applied potentials, the processes at the electrochemical interface with the TiO_2-based photoelectrodes were described by using a simple equivalent electric circuit, commonly known as Randles circuit (**Figure A1a**).
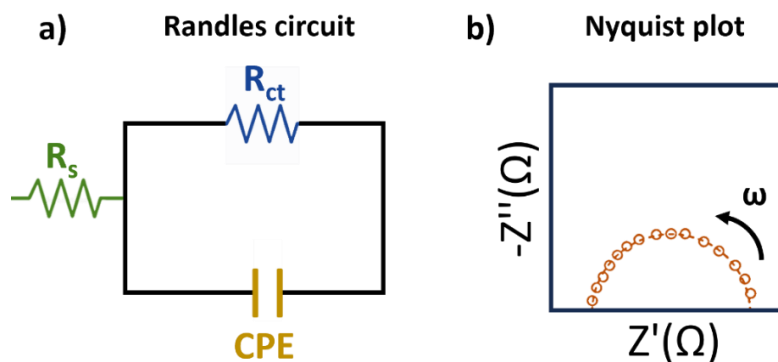
Figure A1| a) Randles equivalent circuit schematic diagram, **b)** Nyquist plot corresponding to the Randles.

It consists of an electrolyte resistance R_s connected in series with the parallel combination of the charge transfer resistance R_{ct} and the costant phase element CPE. In detail, R_s is the resistance related to the electrical connection of the cell and the gap between working and reference electrodes. The R_{ct} is ascribed to the whole electrochemical process (*i.e.,* both the half-reactions occurring on working and counter electrodes). The element CPE models the behavior of a double layer. The Nyquist plot of a Randles circuit is as semicircle (**Figure A1b**).

A3.8 Steady-state Photoluminescence

Steady-state photoluminescence (PL) spectra were recorded using an Horiba Jobin Yvon FluoroMax-P fluorimeter equipped with a Hamamatsu R3896 photomultiplier. The spectra were acquired on TiO_2 tablets operating with a 250 nm excitation wavelength and a high-pass filter with a cut-off of 370 nm.

A3.9 Fourier Transform Infrared spectroscopy under controlled relative humidity conditions

Fourier-transform infrared (FTIR) spectra were acquired in the frequency range from 4000 to 380 cm^{-1} (mid infrared region, MIR) using a Bruker Vertex 80V FTIR spectrometer. In order to obtain a good signal-to-noise ratio, each spectrum was collected at spectral resolution of 4 cm^{-1} with the co-adding and averaging of 128 scans. A background spectrum

(registered in absence of sample) was collected before each measurement and subtracted from the sample spectra in order to eliminate the instrumental and atmospheric moisture contributions. The control of the relative humidity (RH) was achieved by using the saturated salts solutions method (since a given saturated salt solution provides only one RH value at a specific temperature). Prior to each measurement, to be sure that the desired final hydration equilibrium state was achieved, the TiO_2-based photocatalysts were exposed to each saturated salt solution for 12 hours or more. The equilibrium RH value was reached when no significant variation of the shape and intensity of OH stretching band was observed over time.

In this work, six saturated salts solution of sodium hydroxide (NaOH), potassium acetate (CH_3COOK), magnesium chloride ($MgCl_2$), magnesium nitrate ($Mg(NO_3)_2$), sodium chloride (NaCl), and potassium chloride (KCl) were used in order to have RH values ranging from 8.9% to 85% . The equilibrium RH values at 25°C of each saturated salts solutions are reported in **Table A2**.

Salt	RH (%)
NaOH	8.9
CH_3COOK	23
$MgCl_2$	33
$Mg(NO_3)_2$	53
NaCl	75
KCl	85

Table A2| Saturated salt solutions and corresponding relative humidity values at 25°C.

Each solution was prepared by adding a great excess of chemically pure salts into a beaker of deionised water heated up to 70 °C, while stirring continuously until no more solute could be dissolved. Subsequently the solution was cooled down to room temperature. The acquisition of the IR spectra while changing the hydration level of the sample required the design of a proper cell (**Figures A2 a-c**).

Figures A2a,b show the frontal and lateral snapshots of the IR cell, while **Figure A2c** displays the exploded-view diagram of the cell with the different elements composing it.
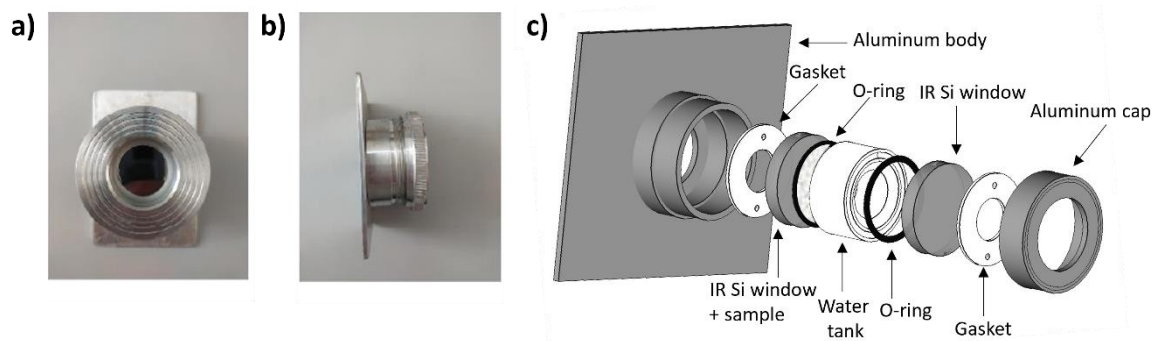
Figure A2 | a) Frontal and **b)** lateral snapshots of the IR cell, **c)** Exploded-view diagram of the IR cell.

Specifically, the cell is a modular system consisting of an aluminium body, two transparent IR windows and a Teflon water tank. Moreover a couple of gaskets and o-rings provide a good seal. All the components of the cell must be transparent to the infrared beam in the mid-IR range and compatible with our measurements under controlled RH conditions. For these reasons, Si offering a good transmission from 1.2 to 7 μm and being insoluble in water was the ideal material for the IR windows. The cell was assembled like a sandwich, with the sample deposited on a Si window at the front, the water tank containing the saturated salt solution in the middle and the second Si window at the back.

For the measurements, a thin film of the undoped or B-doped TiO_2 was formed on top of a Si window. Briefly, 40 mg of TiO_2 catalyst were mixed with 80 mL of distilled water and sonicated until the formation of a stable suspension. The resulting ink was deposited by spray-coating technique into the Si window (acting as substrate) heated up to 120° to allow the evaporation of the water and ensure the adhesion of the powder on the substrate.

A4 Further insights into the water structure at the interface with TiO_2 and B-TiO_2 through FTIR measurements

Figures A3, A4 show the IR spectra of water on the TiO_2 and B-TiO_2 surface, respectively at six different RH values. The spectra exhibit five distinct features between 2800 and 3800 cm^{-1} (OH stretching band) that reflect different OH symmetric stretching vibrations with distinguishable H-bond configuration including: i) single donor-double acceptor (DAA-OH, ~3040 cm^{-1}), ii) double donor-double acceptor (DDAA-OH, ~3220 cm^{-1}), iii) single donor-single acceptor (DA-OH, ~3430 cm^{-1}) and iv) double donor-single acceptor (DDA-OH, ~3570 cm^{-1}), describing fully or partly (defective topology) H-bonded water molecules, and v) free-OH vibrations (~3636 cm^{-1}) related to water molecules not involved in H-bonds.
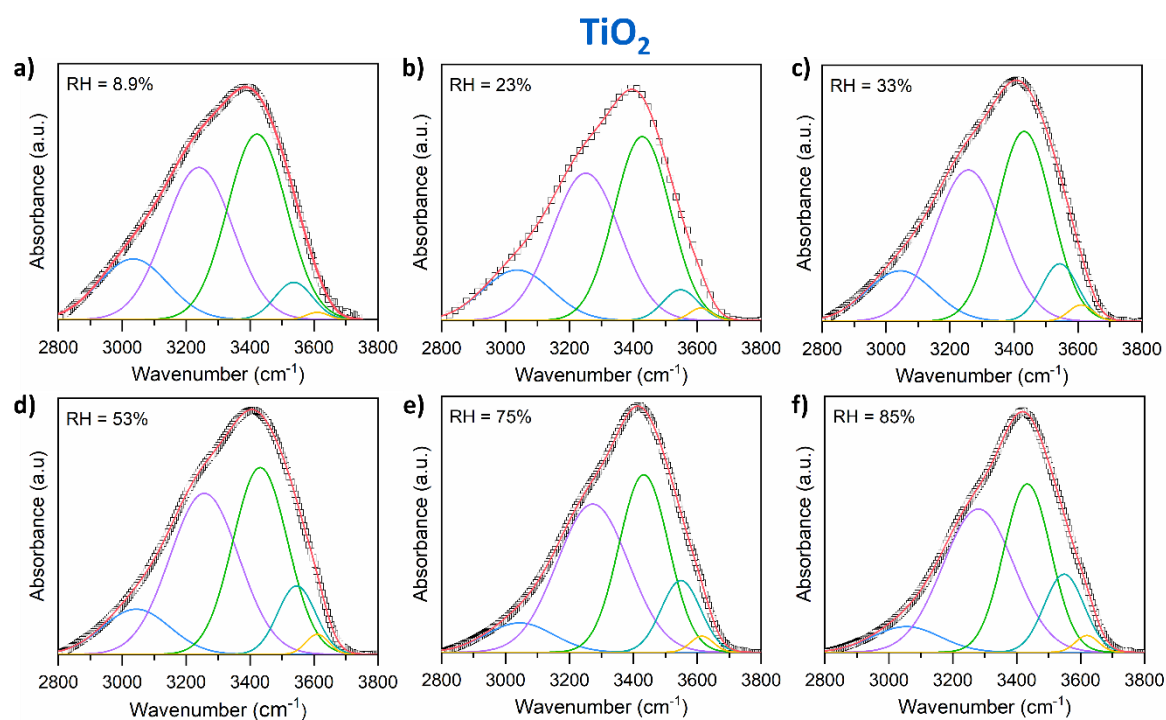
Figure A3 | Gaussian deconvolution of the OH stretching band of water on the TiO$_2$ surface at RH values of **a)** 8.9%, **b)** 23%, **c)** 33%, **d)** 53%, **e)** 75% and **f)** 85%.
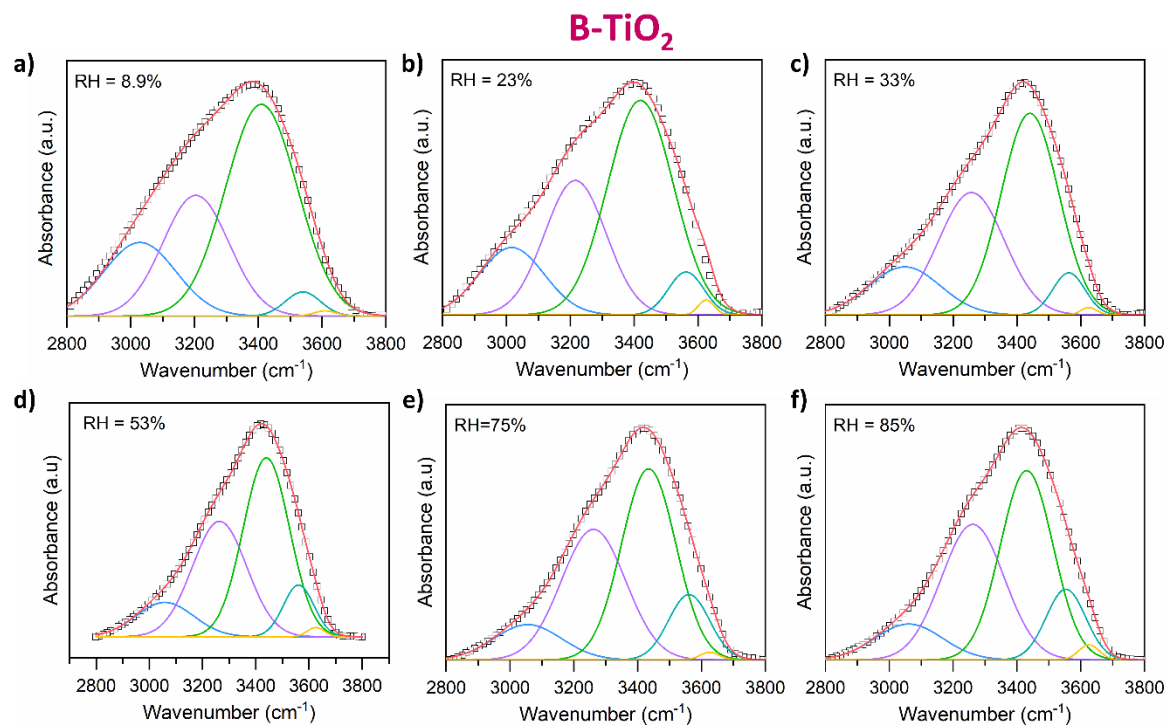
Figure A4 | Gaussian deconvolution of the OH stretching band of water on the B-TiO$_2$ surface at RH values of **a)** 8.9%, **b)** 23%, **c)** 33%, **d)** 53%, **e)** 75% and **f)** 85%.

Moreover, the average number of H-bonds (N_{OH}) per water molecule as a function of the RH for the different systems considered in this work was calculated according to the following equation proposed by Sun et al[128]:

$$N_{OH}= 4 \times A_{DDAA} + 3 \times A_{DDA} + 3 \times A_{DAA} + 2 \times A_{DA} \tag{2}$$

The results of this computational operation are summarized in **Table A3.**

RH (%)	TiO$_2$	B-TiO$_2$
	Average number of H-bonds	
8.9	2.9599	2.7429
23	2.9576	2.7746
33	2.9518	2.8614
53	2.9855	2.8687
75	3.0307	2.8861
85	3.0505	2.9036

Table A3| Average number of hydrogen bonds of water molecules in TiO$_2$ and B-TiO$_2$ samples at different RH values.

As expected for both systems, increasing RH causes an increase in the N_{OH}. Moreover, the data clearly show that N_{OH} is lower in B-TiO$_2$ with respect TiO$_2$. This finding confirms the hydrophobic character of B-TiO$_2$ surface and that the H-bonds strength of the water network at the interface with B-TiO$_2$ is weaker than that at the interface with TiO$_2$.

A5 Computational methods

A5.1 Fundamentals of Density Functional Theory molecular dynamics simulations

Spin-polarised Density Functional Theory molecular dynamics (DFT-MD) simulations on the bulk crystalline structure of TiO$_2$, on the (101) TiO$_2$/water interface and on the (101) B-doped TiO$_2$/water interface have been performed in the Born-Oppenheimer framework employing the CP2K software package. [129, 130] The Perdew-Burke-Ernzerhof (PBE) [131] functional, which in previous works[83, 87, 132, 133] provided a good description of the properties of titanium oxides and liquid water, was adopted in combination with mixed Gaussian-Plane Waves basis sets and Goedecker-Tetter-Hutter (GTH) pseudopotentials. [134] The PBE functional was supplemented with the Hubbard U parameter[135, 136] in order to circumvent over delocalization errors in the exchange and correlation of the Ti-3d orbitals (and the

consequent underestimation of the band gap). Although U is not universal and depends on the ab initio protocol (including DFT functional, pseudo-potentials, projection scheme, etc.), [137, 138] optimum U parameter values were seek and found for all the simulated systems, balancing geometric changes and electronic properties. Specifically, the value of U obtained for TiO_2 was 12 eV, confirming that TiO_2 is a semiconductor with a wide electronic bandgap.

The DZVP-MOLOPT-SR basis set[139] and a 400 Ry plane wave basis set were used, being a good compromise between computational cost and quantum-mechanical accuracy. Grimme's D2 dispersion corrections[140, 141] were employed. Periodic boundary conditions (PBC) were applied in all three spatial directions. DFT-MD simulations were performed in the NVT ensemble (~ 25 ps), where the temperature was kept constant at 300 K by a Nosé-Hoover chain thermostat[142], adopting the Velocity-Verlet algorithm[143] with a time step of 0.5 fs.

The TiO_2-anatase structure crystallizes in a tetragonal unit cell belonging to anatase-41/*amd* crystal symmetry space group, as depicted in **Figure A5a**. The unit cell consists in 13 Ti^{4+} and 17 O^{2-}, for a total of 30 atoms arranged in an optimised tetragonal lattice with a = b = 3.78 Å, c = 9.51 Å sides, where each Ti^{4+} is bonded to 6 O^{2-} in an octahedral geometry (**Figure A5b**) and each O^{2-} is bonded to 3 Ti^{4+} in a planar trigonal arrangement (**Figure A5c**). The primitive cell is composed of 12 atoms, 4 Ti^{4+} and 8 O^{2-}.
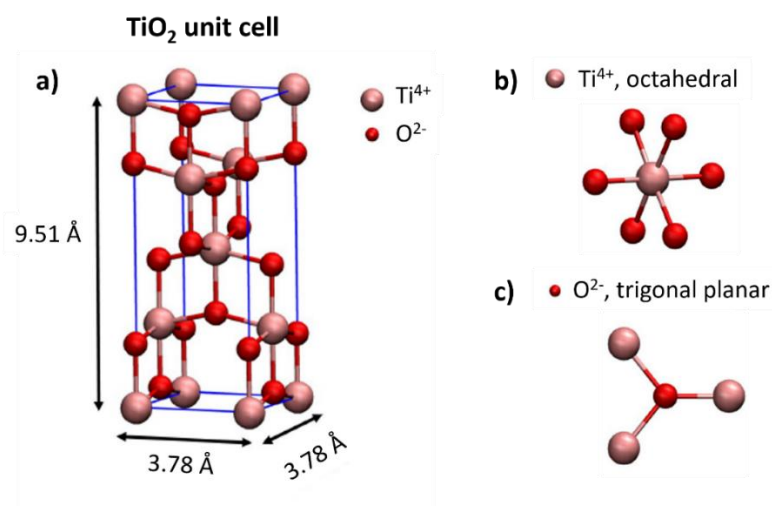
Figure A5| a) Tetragonal unit cell of TiO_2: 30 atoms in total, 13 Ti^{4+} and 17 O^{2-}. Bulk coordination geometry for **b)** Ti^{4+} and **c)** O^{2-} atoms.

All DFT calculations (including geometry optimization and molecular dynamic simulations) were done at the Γ point of the Brillouin zone for the electronic representation. This requires the use of a supercell, *i.e.,* a certain number of replicas of the unit cell in 3D space. To find the minimum number of replicas giving an accurate description of the bulk TiO_2 properties, convergence of lattice parameters of unit cell, bulk modulus, Maximally Localized Wannier Function (MLWF) and atom Projected Density-of-States (PDOS) have been monitored. To this end, full geometry optimizations (atom positions and cell vectors) were performed on the unit cell and on 222 (96 atoms), 332 (216 atoms), 442 (384 atoms), 552 (600 atoms) replica systems of the TiO_2-anatase unit cell. The optimisations started from experimental geometries[144, 145] as reference and conducted without imposing symmetry constraints. Afterwards, optimized bulk structure of TiO_2 (442 replica structure) is cut along the (101) crystallographic plane. For B-TiO_2, two surface Ti^{4+} titanium atoms were replaced with two B^{3+} boron atoms in surface positions as depicted in **Figure A6a**.

Then, both (101) TiO_2 and (101) B-TiO_2 were put in contact with a water environment made of 132 water molecules obtained from a liquid box separately thermally equilibrated with water density of 1 g cm^3. For the simulations of TiO_2/water interface and the B-TiO_2/water interface, a vacuum layer of 15.0 Å has been included above the liquid water in the vertical the z-direction (perpendicular to the surface). This choice was made in order to avoid to simulate confined water due to the PBC applied in the 3 directions while keeping the dimensions of the simulation box large enough in order to allow long time scales for DFT-MD. The simulation boxes and their dimensions for the DFT-MD of (101) TiO_2/liquid water and (101) B-TiO_2/liquid water interfaces are illustrated in **Figures A6b,c**.
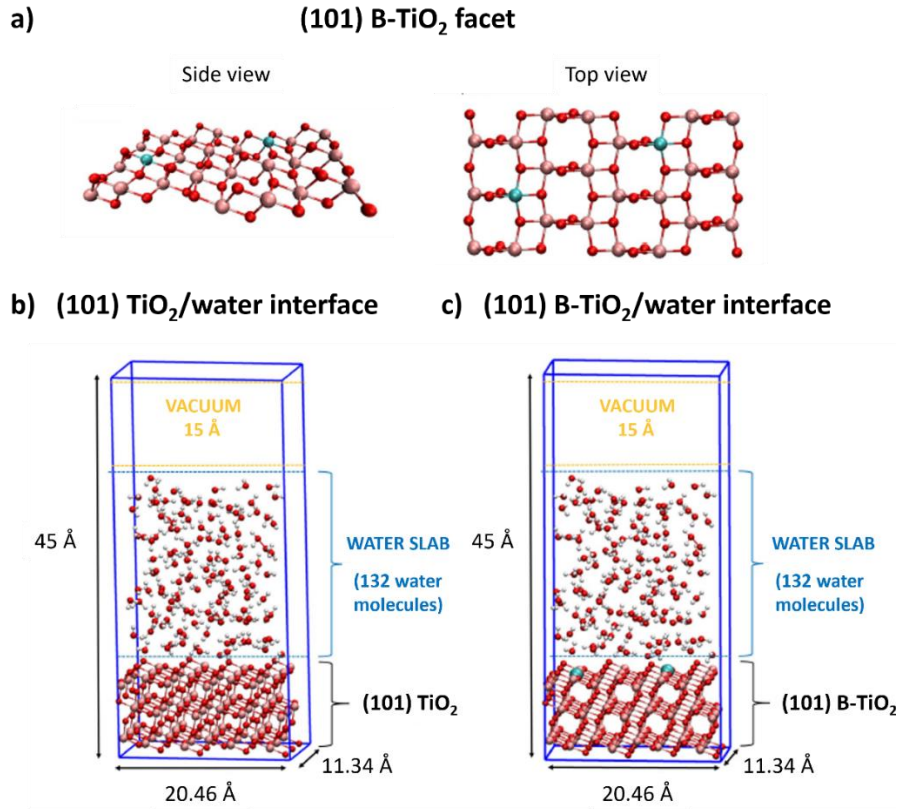
Figure A6| a) Side and top view of the (101) B-TiO$_2$ facet. Simulation boxes for the DFT-MD of **b)** (101) TiO$_2$/water interface and **c)** (101) B-TiO$_2$/water interface. 612 atoms: 216 solid atoms and 132 water molecules (236 atoms). A slab of 15.0 Å vacuum above the liquid water in the vertical z-direction is included to prevent the simulation of too confined water due to PBC. Only one surface (the upper) is in contact with liquid water in each simulation box. The bottom surface is in contact with vacuum.

Once TiO$_2$ is put in contact with water, adsorption of water molecules at the TiO$_2$ water exposed surface occurs. The water–water H-bonds (HBs) network is identified by the criteria proposed by Galli and coworkers[146]: O(-H)· · ·O distance ≤ 3.2 Å and O(-H)· · ·O angle in the range between 140-220°.

The equilibrium number of TiO$_2$ layers (along the z-direction) for the (101) TiO$_2$ slab model have been identified by calculating the surface energy according to equation (3): [132, 133]

$$E_S(n) = \frac{E_{slab}(n) - n \cdot E_{bulk}}{2 \cdot A} \tag{3}$$

where $E_{slab}(n)$ is the total energy of the optimized slab model with n number of TiO$_2$ layers (along the z-direction), E_{bulk} is the total energy of the bulk normalized to one TiO$_2$-unit, A is the area of the (101) TiO$_2$ exposed surface.

A5.2 Structural, electronic and mechanical properties of TiO$_2$

The PBE+U computational set up has ben assessed by calculating the TiO$_2$ solid bulk properties. The lattice parameters were optimized as a function of the simulation box size, *i.e.,* the number of replicas of the TiO$_2$ unit cell required to accurately reproduce the experimental values in the adopted supercell approach. To this end, fully geometry optimizations (atom positions and cell vectors) were performed on 222 (96 atoms), 332 (216 atoms), 442 (384 atoms) and 552 (600 atoms) replica systems.

It was found that the (442) supercell of TiO$_2$ (**Figure A7**) is large enough to converge (within the numerical error) the bulk lattice parameters to a = b = 3.78 Å, c = 9.51 Å side. These results agree very well agreement with previously published data from both experimental[144, 147, 148] and DFT[132, 145, 149, 150] studies.
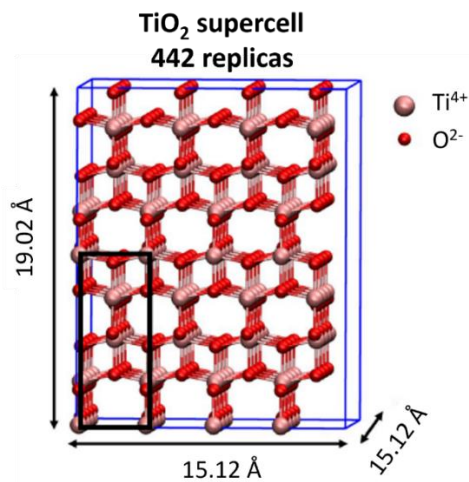
Figure A7| 442 supercell bulk structure of TiO$_2$.

Moreover, the total energies of the abovementioned supercell structures have been calculated according to the Murnaghan's equation of state as in Ref. [151]. In that way, for the (442) TiO$_2$ supercell a bulk modulus of 287 GPa has been calculated, confirming that the (442) supercell is the best compromise between the number of atoms (384), the simulation box size and reproduction of the expected TiO$_2$ bulk properties (such as lattice parameters and bulk modulus). The equilibrium lattice parameters and the total energies of the replica systems of the TiO$_2$ unit cell are listed in **Table A4**.

SYSTEM (number of replicas)	Lattice parameters (a; b; c) (Å)	Bulk modulus (GPa)
222	3.69; 3.69; 9.85	50
332	3.75; 3.75; 9.85	78.7
442	**3.78; 3.78; 9.51**	**287**
552	3.76; 3.76; 9.49	820.3

Table A4| List o the equilibrium lattice parameters and bulk modulus values calculated for 222, 332, 442, 552 supercell bulk structures of TiO_2.

Figure A8a shows the computed total DOS and PDOS obtained for the (442) supercells of bulk TiO_2 using PBE and PBE+U calculations.
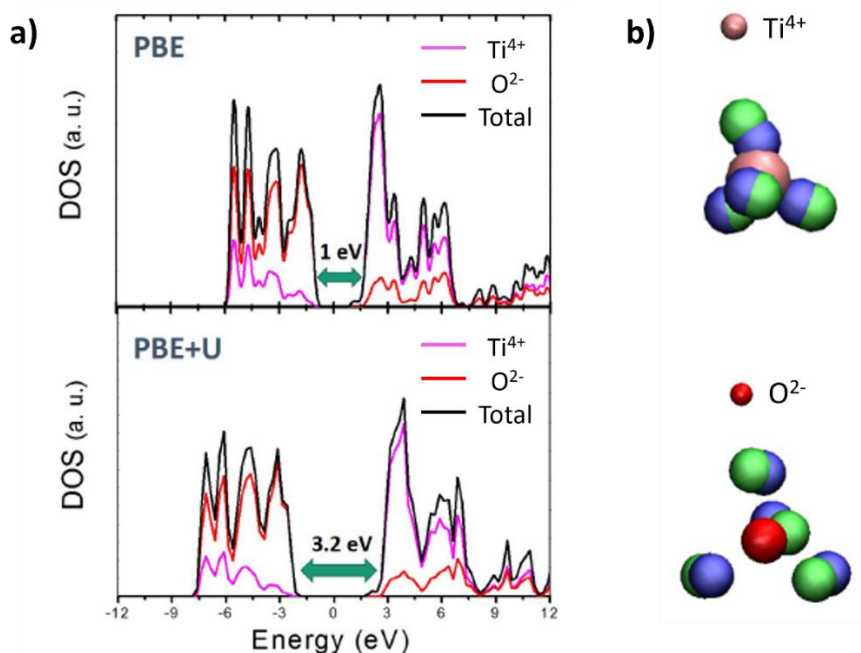
Figure A8| a) Total DOS and PDOS for the (442) TiO_2 supercell. Results from PBE and PBE+U (U=12 eV) calculations on top and bottom panel, respectively. The Fermi energy level is set to 0. The PBE-functional corrected by the Hubbard U term correctly reproduces the experimental band-gap energy value of 3.2 eV[149, 152]. **b)** Outer-shell electronic representation of Ti^{4+} and O^{2-} atoms from MLWF calculation performed on the (442) TiO_2 supercell: green and blue spheres represent spin-up electrons and spin-down electrons, respectively. Ti^{4+} outer-shell $3s^2$, $3p^6$: 8 e^- in total, 4 spin-up e^- and 4 spin-down e^-. O^{2-} outer-shell $2s^2$, $2p^6$: 8 e^- in total, 4 spin-up e^- and 4 spin-down e^-.

The comparison highlights that it is mandatory to take in account the Hubbard U parameter (U=12 eV) in order to correctly describe the electronic properties of the bulk TiO_2. When only the PBE functional is used, the electronic bandgap is underestimated (see top panel in

Figure A8a), whereas the PBE+U functional reproduces correctly the experimental band-gap energy value of 3.2 eV at room temperature (see bottom panel in **Figure A8a**).

References

(1) Perez, M.; Perez, R. Update 2022–A fundamental look at supply side energy reserves for the planet. *Solar Energy Advances* **2022**, *2*, 100014.

(2) Jin, S. What else can photoelectrochemical solar energy conversion do besides water splitting and CO2 reduction? ACS Publications: 2018; Vol. 3, pp 2610-2612.

(3) Romano, V.; D'Angelo, G.; Perathoner, S.; Centi, G. Current density in solar fuel technologies. *Energy & Environmental Science* **2021**, *14* (11), 5760-5787.

(4) Hisatomi, T.; Domen, K. Reaction systems for solar hydrogen production via water splitting with particulate semiconductor photocatalysts. *Nature Catalysis* **2019**, *2* (5), 387-399.

(5) Hisatomi, T.; Domen, K. Overall water splitting: What's next? *Next Energy* **2023**, *1* (1), 100006.

(6) Takanabe, K. Photocatalytic Water Splitting: Quantitative Approaches toward Photocatalyst by Design. *ACS Catalysis* **2017**, *7* (11), 8006-8022.

(7) Fujishima, A.; Honda, K. Electrochemical Photolysis of Water at a Semiconductor Electrode. *Nature* **1972**, *238* (5358), 37-38

(8) Zhang, X.; Zhang, S.; Cui, X.; Zhou, W.; Cao, W.; Cheng, D.; Sun, Y. Recent Advances in TiO2-based Photoanodes for Photoelectrochemical Water Splitting. *Chemistry – An Asian Journal* **2022**, *17* (20), e202200668.

(9) Puerres, J.; Polanía, S.; Pérez-Torres, A. s. F.; Erazo, E. A.; Cortés, M. T.; Ortiz, P. Reduced TiO2 Nanorods Decorated with Carbon Nanodots for Photoelectrochemical Water Oxidation. *ACS Applied Nano Materials* **2023**, *6* (15), 14029-14039.

(10) Lim, Y.; Lee, S. Y.; Kim, D.; Han, M.-K.; Han, H. S.; Kang, S. H.; Kim, J. K.; Sim, U.; Park, Y. I. Expanded solar absorption spectrum to improve photoelectrochemical oxygen evolution reaction: Synergistic effect of upconversion nanoparticles and ZnFe2O4/TiO2. *Chemical Engineering Journal* **2022**, *438*, 135503.

(11) Lu, R.-C.; Zhang, K.; Liu, X.-H.; Chen, Q.-Y.; Wang, Y.-H. Investigation of the charge transport kinetics and photoelectrochemical properties of CuInS2/R-TiO2 NTs heterostructures photoanode. *Applied Surface Science* **2022**, *585*, 152742.

(12) He, S.; Meng, Y.; Cao, Y.; Huang, S.; Yang, J.; Tong, S.; Wu, M. Hierarchical Ta-doped TiO2 nanorod arrays with improved charge separation for photoelectrochemical water oxidation under FTO side illumination. *Nanomaterials* **2018**, *8* (12), 983.

(13) Li, T.; Ding, D. Photoelectrochemical water splitting with black Ni/Si-doped TiO2 nanostructures. *International Journal of Hydrogen Energy* **2020**, *45* (41), 20983-20992.

(14) Cho, I. S.; Chen, Z.; Forman, A. J.; Kim, D. R.; Rao, P. M.; Jaramillo, T. F.; Zheng, X. Branched TiO2 nanorods for photoelectrochemical hydrogen production. *Nano letters* **2011**, *11* (11), 4978-4984.

(15) Yang, J.-S.; Lin, W.-H.; Lin, C.-Y.; Wang, B.-S.; Wu, J.-J. n-Fe2O3 to N+-TiO2 heterojunction photoanode for photoelectrochemical water oxidation. *ACS Applied Materials & Interfaces* **2015**, *7* (24), 13314-13321.

(16) Liu, C.; Chen, L.; Su, X.; Chen, S.; Zhang, J.; Yang, H.; Pei, Y. Activating a TiO2/BiVO4 film for photoelectrochemical water splitting by constructing a heterojunction interface with a uniform crystal plane orientation. *ACS Applied Materials & Interfaces* **2021**, *14* (1), 2316-2325.

(17) Basavarajappa, P. S.; Patil, S. B.; Ganganagappa, N.; Reddy, K. R.; Raghu, A. V.; Reddy, C. V. Recent progress in metal-doped TiO2, non-metal doped/codoped TiO2 and TiO2 nanostructured hybrids for enhanced photocatalysis. *International journal of hydrogen energy* **2020**, *45* (13), 7764-7778.

(18) Cano-Casanova, L.; Ansón-Casaos, A.; Hernández-Ferrer, J.; Benito, A. M.; Maser, W. K.; Garro, N.; Lillo-Rodenas, M. A.; Román-Martínez, M. d. C. Surface-Enriched Boron-Doped TiO2 Nanoparticles as Photocatalysts for Propene Oxidation. *ACS Applied Nano Materials* **2022**, *5* (9), 12527-12539.

(19) Patel, N.; Dashora, A.; Jaiswal, R.; Fernandes, R.; Yadav, M.; Kothari, D. C.; Ahuja, B. L.; Miotello, A. Experimental and Theoretical Investigations on the Activity and Stability of Substitutional and Interstitial Boron in TiO2 Photocatalyst. *The Journal of Physical Chemistry C* **2015**, *119* (32), 18581-18590.

(20) Zhao, W.; Ma, W.; Chen, C.; Zhao, J.; Shuai, Z. Efficient degradation of toxic organic pollutants with Ni2O3/TiO2-x B x under visible irradiation. *Journal of the American Chemical Society* **2004**, *126* (15), 4782-4783.

(21) Chen, D.; Yang, D.; Wang, Q.; Jiang, Z. Effects of boron doping on photocatalytic activity and microstructure of titanium dioxide nanoparticles. *Industrial & Engineering Chemistry Research* **2006**, *45* (12), 4110-4116.

(22) Zaleska, A.; Grabowska, E.; Sobczak, J. W.; Gazda, M.; Hupka, J. Photocatalytic activity of boron-modified TiO2 under visible light: The effect of boron content, calcination temperature and TiO2 matrix. *Applied Catalysis B: Environmental* **2009**, *89* (3-4), 469-475.

(23) Niu, P.; Wu, G.; Chen, P.; Zheng, H.; Cao, Q.; Jiang, H. Optimization of boron doped TiO2 as an efficient visible light-driven photocatalyst for organic dye degradation with high reusability. *Frontiers in Chemistry* **2020**, *8*, 172.

(24) Feng, N.; Liu, F.; Huang, M.; Zheng, A.; Wang, Q.; Chen, T.; Cao, G.; Xu, J.; Fan, J.; Deng, F. Unravelling the Efficient Photocatalytic Activity of Boron-induced Ti3+ Species in the Surface Layer of TiO2. *Scientific Reports* **2016**, *6* (1), 34765.

(25) Wang, Z.; Li, C.; Domen, K. Recent developments in heterogeneous photocatalysts for solar-driven overall water splitting. *Chemical Society Reviews* **2019**, *48* (7), 2109-2125.

(26) Ren, W.; Cheng, C.; Shao, P.; Luo, X.; Zhang, H.; Wang, S.; Duan, X. Origins of electron-transfer regime in persulfate-based nonradical oxidation processes. *Environmental Science & Technology* **2021**, *56* (1), 78-97.

(27) Payne, T. E.; Brendler, V.; Ochs, M.; Baeyens, B.; Brown, P. L.; Davis, J. A.; Ekberg, C.; Kulik, D. A.; Lutzenkirchen, J.; Missana, T. Guidelines for thermodynamic sorption modelling in the context of radioactive waste disposal. *Environmental modelling & software* **2013**, *42*, 143-156.

(28) de Aguirre, A.; Funes-Ardoiz, I.; Maseras, F. Computational Characterization of Single-Electron Transfer Steps in Water Oxidation. In *Inorganics*, 2019; Vol. 7.

(29) López-Estrada, O.; Laguna, H. G.; Barrueta-Flores, C.; Amador-Bedolla, C. Reassessment of the Four-Point Approach to the Electron-Transfer Marcus–Hush Theory. *ACS Omega* **2018**, *3* (2), 2130-2140.

(30) Toney, M. F.; Howard, J. N.; Richer, J.; Borges, G. L.; Gordon, J. G.; Melroy, O. R.; Wiesler, D. G.; Yee, D.; Sorensen, L. B. Voltage-dependent ordering of water molecules at an electrode–electrolyte interface. *Nature* **1994**, *368* (6470), 444-446.

(31) Toney, M. F.; Howard, J. N.; Richer, J.; Borges, G. L.; Gordon, J. G.; Melroy, O. R.; Wiesler, D. G.; Yee, D.; Sorensen, L. B. Distribution of water molecules at Ag (111)/electrolyte interface as studied with surface X-ray scattering. *Surface Science* **1995**, *335*, 326-332.

(32) Schweighofer, K. J.; Xia, X.; Berkowitz, M. L. Molecular dynamics study of water next to electrified Ag (111) surfaces. *Langmuir* **1996**, *12* (16), 3747-3752.

(33) Raghavan, K.; Foster, K.; Motakabbir, K.; Berkowitz, M. Structure and dynamics of water at the Pt (111) interface: Molecular dynamics study. *The Journal of chemical physics* **1991**, *94* (3), 2110-2117.

(34) Spohr, E. Computer simulation of the water/platinum interface. *The Journal of Physical Chemistry* **1989**, *93* (16), 6171-6180.

(35) Yeh, I.-C.; Berkowitz, M. Structure and dynamics of water at water| Pt interface as seen by molecular dynamics computer simulation. *Journal of Electroanalytical Chemistry* **1998**, *450* (2), 313-325.

(36) Antony, A. C.; Liang, T.; Akhade, S. A.; Janik, M. J.; Phillpot, S. R.; Sinnott, S. B. Effect of surface chemistry on water interaction with Cu (111). *Langmuir* **2016**, *32* (32), 8061-8070.

(37) Izvekov, S.; Voth, G. A. Ab initio molecular dynamics simulation of the Ag (111)-water interface. *The Journal of Chemical Physics* **2001**, *115* (15), 7196-7206.

(38) Fumagalli, L.; Esfandiar, A.; Fabregas, R.; Hu, S.; Ares, P.; Janardanan, A.; Yang, Q.; Radha, B.; Taniguchi, T.; Watanabe, K. Anomalously low dielectric constant of confined water. *Science* **2018**, *360* (6395), 1339-1342.

(39) Itoh, H.; Sakuma, H. Dielectric constant of water as a function of separation in a slab geometry: A molecular dynamics study. *The Journal of Chemical Physics* **2015**, *142* (18).

(40) Bonn, M.; Nagata, Y.; Backus, E. H. Molecular Structure and Dynamics of Water at the Water–Air Interface Studied with Surface-Specific Vibrational Spectroscopy. *Angewandte Chemie International Edition* **2015**, *54* (19), 5560-5576.

(41) Osawa, M.; Tsushima, M.; Mogami, H.; Samjeské, G.; Yamakata, A. Structure of Water at the Electrified Platinum−Water Interface: A Study by Surface-Enhanced Infrared Absorption Spectroscopy. *The Journal of Physical Chemistry C* **2008**, *112* (11), 4248-4256.

(42) Rao, R. R.; Kolb, M. J.; Hwang, J.; Pedersen, A. F.; Mehta, A.; You, H.; Stoerzinger, K. A.; Feng, Z.; Zhou, H.; Bluhm, H.; et al. Surface Orientation Dependent Water Dissociation on Rutile Ruthenium Dioxide. *The Journal of Physical Chemistry C* **2018**, *122* (31), 17802-17811.

(43) Cassone, G.; Giaquinta, P. V.; Saija, F.; Saitta, A. M. Effect of Electric Field Orientation on the Mechanical and Electrical Properties of Water Ices: An Ab-initio Study. *The Journal of Physical Chemistry B* **2014**, *118* (44), 12717-12724.

(44) Creazzo, F.; Pezzotti, S.; Bougueroua, S.; Serva, A.; Sponer, J.; Saija, F.; Cassone, G.; Gaigeot, M.-P. Enhanced conductivity of water at the electrified air–water interface: a DFT-MD characterization. *Physical Chemistry Chemical Physics* **2020**, *22* (19), 10438-10446.

(45) Rey, R.; Møller, K. B.; Hynes, J. T. Hydrogen bond dynamics in water and ultrafast infrared spectroscopy. *The Journal of Physical Chemistry A* **2002**, *106* (50), 11993-11996.

(46) Petit, T.; Lounasvuori, M.; Chemin, A.; Bärmann, P. Nanointerfaces: Concepts and Strategies for Optical and X-ray Spectroscopic Characterization. *ACS Physical Chemistry Au* **2023**.

(47) Pennington, A. M.; Okonmah, A. I.; Munoz, D. T.; Tsilomelekis, G.; Celik, F. E. Changes in Polymorph Composition in P25-TiO2 during Pretreatment Analyzed by Differential Diffuse Reflectance Spectral Analysis. *The Journal of Physical Chemistry C* **2018**, *122* (9), 5093-5104.

(48) Yang, K.; Dai, Y.; Huang, B. Origin of the photoactivity in boron-doped anatase and rutile Ti O 2 calculated from first principles. *Physical Review B* **2007**, *76* (19), 195201.

(49) Foo, C.; Li, Y.; Lebedev, K.; Chen, T.; Day, S.; Tang, C.; Tsang, S. C. E. Characterisation of oxygen defects and nitrogen impurities in TiO2 photocatalysts using variable-temperature X-ray powder diffraction. *Nature Communications* **2021**, *12* (1), 661. DOI: 10.1038/s41467-021-20977-z.

(50) Liu, G.; Yang, H. G.; Wang, X.; Cheng, L.; Lu, H.; Wang, L.; Lu, G. Q.; Cheng, H.-M. Enhanced Photoactivity of Oxygen-Deficient Anatase TiO2 Sheets with Dominant {001} Facets. *The Journal of Physical Chemistry C* **2009**, *113* (52), 21784-21788.

(51) Hosseini-Sarvari, M.; Valikhani, A. Boron-doped TiO2 (B-TiO2): visible-light photocatalytic difunctionalization of alkenes and alkynes. *New Journal of Chemistry* **2021**, *45* (28), 12464-12470.

(52) Quesada-González, M.; Boscher, N. D.; Carmalt, C. J.; Parkin, I. P. Interstitial Boron-Doped TiO2 Thin Films: The Significant Effect of Boron on TiO2 Coatings Grown by Atmospheric Pressure Chemical Vapor Deposition. *ACS Applied Materials & Interfaces* **2016**, *8* (38), 25024-25029.

(53) Pan, X.; Yang, M.-Q.; Fu, X.; Zhang, N.; Xu, Y.-J. Defective TiO2 with oxygen vacancies: synthesis, properties and photocatalytic applications. *Nanoscale* **2013**, *5* (9), 3601-3614.

(54) Frank, O.; Zukalova, M.; Laskova, B.; Kürti, J.; Koltai, J.; Kavan, L. Raman spectra of titanium dioxide (anatase, rutile) with identified oxygen isotopes (16, 17, 18). *Physical Chemistry Chemical Physics* **2012**, *14* (42), 14567-14572.

(55) Abramo, F. P.; De Luca, F.; Passalacqua, R.; Centi, G.; Giorgianni, G.; Perathoner, S.; Abate, S. Electrocatalytic production of glycolic acid via oxalic acid reduction on titania debris supported on a TiO2 nanotube array. *Journal of Energy Chemistry* **2022**, *68*, 669-678.

(56) Wang, X.; Wang, K.; Wang, H.; Wang, Z.; Chen, X.; Dai, W.; Fu, X. H2-oxidation driven by its behavior of losing an electron over B-doped TiO2 under UV irradiation. *Physical Chemistry Chemical Physics* **2021**, *23* (1), 186-195.

(57) Zhang, M.; Dai, Y.; Zhang, S.; Chen, W. Highly efficient photocatalytic activity of boron-doped TiO2 for gas phase degradation of benzene. *Rare Metals* **2011**, *30* (1), 243-248.

(58) In, S.; Orlov, A.; Berg, R.; García, F.; Pedrosa-Jimenez, S.; Tikhov, M. S.; Wright, D. S.; Lambert, R. M. Effective Visible Light-Activated B-Doped and B,N-Codoped TiO2 Photocatalysts. *Journal of the American Chemical Society* **2007**, *129* (45), 13790-13791.

(59) Feng, N.; Zheng, A.; Wang, Q.; Ren, P.; Gao, X.; Liu, S.-B.; Shen, Z.; Chen, T.; Deng, F. Boron Environments in B-Doped and (B, N)-Codoped TiO2 Photocatalysts: A Combined Solid-State NMR and Theoretical Calculation Study. *The Journal of Physical Chemistry C* **2011**, *115* (6), 2709-2719.

(60) Li, L.; Meng, F.; Hu, X.; Qiao, L.; Sun, C. Q.; Tian, H.; Zheng, W. TiO2 Band Restructuring by B and P Dopants. *PLOS ONE* **2016**, *11* (4), e0152726.

(61) Ansón-Casaos, A.; Sampaio, M. J.; Jarauta-Córdoba, C.; Martínez, M. T.; Silva, C. G.; Faria, J. L.; Silva, A. M. T. Evaluation of sol–gel TiO2 photocatalysts modified with carbon or boron compounds and crystallized in nitrogen or air atmospheres. *Chemical Engineering Journal* **2015**, *277*, 11-20.

(62) Dozzi, M. V.; Artiglia, L.; Granozzi, G.; Ohtani, B.; Selli, E. Photocatalytic Activity vs Structural Features of Titanium Dioxide Materials Singly Doped or Codoped with Fluorine and Boron. *The Journal of Physical Chemistry C* **2014**, *118* (44), 25579-25589.

(63) Jeong, J.-H.; Jung, D.-w.; Shin, E. W.; Oh, E.-S. Boron-doped TiO2 anode materials for high-rate lithium ion batteries. *Journal of Alloys and Compounds* **2014**, *604*, 226-232.

(64) Thommes, M.; Kaneko, K.; Neimark, A. V.; Olivier, J. P.; Rodriguez-Reinoso, F.; Rouquerol, J.; Sing, K. S. W. Physisorption of gases, with special reference to the evaluation

of surface area and pore size distribution (IUPAC Technical Report). **2015**, *87* (9-10), 1051-1069.

(65) Odier, P.; Lecomte, J.; Loup, J. P. Effect of non-stoichiometry on the sintering of doped TiO2. *Journal of Materials Science* **1988**, *23* (12), 4547-4553.

(66) Liang, Q.; Brocks, G.; Bieberle-Hütter, A. Oxygen evolution reaction (OER) mechanism under alkaline and acidic conditions. *Journal of Physics: Energy* **2021**, *3* (2), 026001.

(67) Tang, J.; Durrant, J. R.; Klug, D. R. Mechanism of Photocatalytic Water Splitting in TiO2. Reaction of Water with Photoholes, Importance of Charge Carrier Dynamics, and Evidence for Four-Hole Chemistry. *Journal of the American Chemical Society* **2008**, *130* (42), 13885-13891.

(68) Ma, X.; Shi, Y.; Liu, J.; Li, X.; Cui, X.; Tan, S.; Zhao, J.; Wang, B. Hydrogen-Bond Network Promotes Water Splitting on the TiO2 Surface. *Journal of the American Chemical Society* **2022**, *144* (30), 13565-13573.

(69) Mansingh, S.; Das, K. K.; Behera, A.; Subudhi, S.; Sultana, S.; Parida, K. Bandgap engineering via boron and sulphur doped carbon modified anatase TiO2: a visible light stimulated photocatalyst for photo-fixation of N2 and TCH degradation. *Nanoscale Advances* **2020**, *2* (5), 2004-2017.

(70) Bertie, J. E.; Lan, Z. Infrared intensities of liquids XX: The intensity of the OH stretching band of liquid water revisited, and the best current values of the optical constants of H 2 O (l) at 25 C between 15,000 and 1 cm-1. *Applied Spectroscopy* **1996**, *50* (8), 1047-1057.

(71) Cassone, G.; Sponer, J.; Trusso, S.; Saija, F. Ab initio spectroscopy of water under electric fields. *Physical Chemistry Chemical Physics* **2019**, *21* (38), 21205-21212.

(72) Jiang, E.; Guo, C.; Zhao, X.; Chao, Y.; Ma, D.; Huo, P.; Yan, Y.; Zhou, P.; Yan, Y. Nanochannel-Induced Efficient Water Splitting at the Superhydrophobic Interface. *ACS nano* **2023**.

(73) Yang, W.; Wei, D.; Jin, X.; Xu, C.; Geng, Z.; Guo, Q.; Ma, Z.; Dai, D.; Fan, H.; Yang, X. Effect of the hydrogen bond in photoinduced water dissociation: A double-edged sword. *The Journal of Physical Chemistry Letters* **2016**, *7* (4), 603-608.

(74) Agmon, N.; Bakker, H. J.; Campen, R. K.; Henchman, R. H.; Pohl, P.; Roke, S.; Thämer, M.; Hassanali, A. Protons and hydroxide ions in aqueous systems. *Chemical reviews* **2016**, *116* (13), 7642-7672.

(75) Choe, C.; Schleusener, J.; Lademann, J.; Darvin, M. E. Age related depth profiles of human Stratum Corneum barrier-related molecular parameters by confocal Raman microscopy in vivo. *Mechanisms of ageing and development* **2018**, *172*, 6-12.

(76) Sun, Q. The effects of dissolved hydrophobic and hydrophilic groups on water structure. *Journal of Solution Chemistry* **2020**, *49* (12), 1473-1484.

(77) Liu, G.; Pan, J.; Yin, L.; Irvine, J. T. S.; Li, F.; Tan, J.; Wormald, P.; Cheng, H.-M. Heteroatom-Modulated Switching of Photocatalytic Hydrogen and Oxygen Evolution Preferences of Anatase TiO2 Microspheres. *Advanced Functional Materials* **2012**, *22* (15), 3233-3238.

(78) Eidsvåg, H.; Bentouba, S.; Vajeeston, P.; Yohi, S.; Velauthapillai, D. TiO2 as a Photocatalyst for Water Splitting—An Experimental and Theoretical Review. In *Molecules*, 2021; Vol. 26.

(79) Li, B.; Wu, S.; Gao, X. Theoretical calculation of a TiO2-based photocatalyst in the field of water splitting: A review. **2020**, *9* (1), 1080-1103.

(80) Nunzi, F.; De Angelis, F. Modeling titanium dioxide nanostructures for photocatalysis and photovoltaics. *Chemical Science* **2022**, *13* (33), 9485-9497.

(81) Nam, Y.; Lim, J. H.; Ko, K. C.; Lee, J. Y. Photocatalytic activity of TiO2 nanoparticles: a theoretical aspect. *Journal of Materials Chemistry A* **2019**, *7* (23), 13833-13859.

(82) Edelmannová, M.; de los Milagros Ballari, M.; Přibyl, M.; Kočí, K. Experimental and modelling studies on the photocatalytic generation of hydrogen during water-splitting over a commercial TiO2 photocatalyst P25. *Energy Conversion and Management* **2021**, *245*, 114582.

(83) Lazzeri, M.; Vittadini, A.; Selloni, A. Structure and energetics of stoichiometric TiO 2 anatase surfaces. *Physical Review B* **2001**, *63* (15), 155409.

(84) Sanjinés, R.; Tang, H.; Berger, H.; Gozzo, F.; Margaritondo, G.; Lévy, F. Electronic structure of anatase TiO2 oxide. *Journal of Applied Physics* **1994**, *75* (6), 2945-2951.

(85) Berardo, E.; Zwijnenburg, M. A. Modeling the Water Splitting Activity of a TiO2 Rutile Nanoparticle. *The Journal of Physical Chemistry C* **2015**, *119* (24), 13384-13393.

(86) Li, R.; Weng, Y.; Zhou, X.; Wang, X.; Mi, Y.; Chong, R.; Han, H.; Li, C. Achieving overall water splitting using titanium dioxide-based photocatalysts of different phases. *Energy & Environmental Science* **2015**, *8* (8), 2377-2382.

(87) Calegari Andrade, M. F.; Ko, H.-Y.; Car, R.; Selloni, A. Structure, Polarization, and Sum Frequency Generation Spectrum of Interfacial Water on Anatase TiO2. *The Journal of Physical Chemistry Letters* **2018**, *9* (23), 6716-6721.

(88) Wang, H.-L.; Hu, Z.-P.; Li, H. Dissociation of liquid water on defective rutile TiO2 (110) surfaces using ab initio molecular dynamics simulations. *Frontiers of Physics* **2018**, *13* (3), 138107.

(89) Zhou, G.; Liu, C.; Huang, L. Molecular Dynamics Simulation of First-Adsorbed Water Layer at Titanium Dioxide Surfaces. *Journal of Chemical & Engineering Data* **2018**, *63* (7), 2420-2429.

(90) Sheng, H.; Zhang, H.; Song, W.; Ji, H.; Ma, W.; Chen, C.; Zhao, J. Activation of Water in Titanium Dioxide Photocatalysis by Formation of Surface Hydrogen Bonds: An In Situ IR Spectroscopy Study. *Angew Chem Int Ed Engl* **2015**, *54* (20), 5905-5909.

(91) Margineda, J.; English, N. J. Dynamical and structural properties of adsorbed water molecules at the TiO2 anatase-(1 0 1) surface: Importance of interfacial hydrogen-bond rearrangements. *Chemical Physics Letters* **2020**, *743*, 137164.

(92) Kumar, N.; Neogi, S.; Kent, P. R. C.; Bandura, A. V.; Kubicki, J. D.; Wesolowski, D. J.; Cole, D.; Sofo, J. O. Hydrogen Bonds and Vibrations of Water on (110) Rutile. *The Journal of Physical Chemistry C* **2009**, *113* (31), 13732-13740.

(93) Mattioli, G.; Filippone, F.; Caminiti, R.; Amore Bonapasta, A. Short Hydrogen Bonds at the Water/TiO2 (Anatase) Interface. *The Journal of Physical Chemistry C* **2008**, *112* (35), 13579-13586.

(94) Tachikawa, T.; Yamashita, S.; Majima, T. Evidence for crystal-face-dependent TiO2 photocatalysis from single-molecule imaging and kinetic analysis. *Journal of the American Chemical Society* **2011**, *133* (18), 7197-7204.

(95) Li, Y.-F.; Selloni, A. Pathway of photocatalytic oxygen evolution on aqueous TiO2 anatase and insights into the different activities of anatase and rutile. *ACS Catalysis* **2016**, *6* (7), 4769-4774.

(96) Kashiwaya, S.; Morasch, J.; Streibel, V.; Toupance, T.; Jaegermann, W.; Klein, A. The work function of TiO2. *Surfaces* **2018**, *1* (1), 73-89.

(97) Mansfeldova, V.; Zlamalova, M.; Tarabkova, H.; Janda, P.; Vorokhta, M.; Piliai, L.; Kavan, L. Work function of TiO2 (anatase, rutile, and brookite) single crystals: effects of the environment. *The Journal of Physical Chemistry C* **2021**, *125* (3), 1902-1912.

(98) Groß, A. The virtual chemistry lab for reactions at surfaces: Is it possible? Will it be useful? *Surface science* **2002**, *500* (1-3), 347-367.

(99) Cassone, G. Nuclear quantum effects largely influence molecular dissociation and proton transfer in liquid water under an electric field. *The journal of physical chemistry letters* **2020**, *11* (21), 8983-8988.

(100) Barthel, E. R.; Martini, I. B.; Schwartz, B. J. How Does the Solvent Control Electron Transfer? Experimental and Theoretical Studies of the Simplest Charge Transfer Reaction. *The Journal of Physical Chemistry B* **2001**, *105* (49), 12230-12241.

(101) Creazzo, F.; Luber, S. Water-Assisted Chemical Route Towards the Oxygen Evolution Reaction at the Hydrated (110) Ruthenium Oxide Surface: Heterogeneous Catalysis via DFT-MD and Metadynamics Simulations. *Chemistry–A European Journal* **2021**, *27* (68), 17024-17037.

(102) Huang, J.; Jiang, Y.; An, T.; Cao, M. Increasing the active sites and intrinsic activity of transition metal chalcogenide electrocatalysts for enhanced water splitting. *Journal of Materials Chemistry A* **2020**, *8* (48), 25465-25498.

(103) Zhang, M.; Lu, M.; Lang, Z. L.; Liu, J.; Liu, M.; Chang, J. N.; Li, L. Y.; Shang, L. J.; Wang, M.; Li, S. L. Semiconductor/covalent-organic-framework Z-scheme heterojunctions for artificial photosynthesis. *Angewandte Chemie* **2020**, *132* (16), 6562-6568.

(104) Kumar, A.; Hasija, V.; Sudhaik, A.; Raizada, P.; Van Le, Q.; Singh, P.; Pham, T.-H.; Kim, T.; Ghotekar, S.; Nguyen, V.-H. Artificial leaf for light-driven CO2 reduction: Basic concepts, advanced structures and selective solar-to-chemical products. *Chemical Engineering Journal* **2022**, *430*, 133031.

(105) Gao, L.; Cui, X.; Sewell, C. D.; Li, J.; Lin, Z. Recent advances in activating surface reconstruction for the high-efficiency oxygen evolution reaction. *Chemical Society Reviews* **2021**, *50* (15), 8428-8469.

(106) Liu, Q.; Lin, J.; Cheng, H.; Wei, L.; Wang, F. Simultaneous co-Photocatalytic CO2 Reduction and Ethanol Oxidation towards Synergistic Acetaldehyde Synthesis. *Angewandte Chemie* **2023**, *135* (13), e202218720.

(107) Kumaravel, V.; Bartlett, J.; Pillai, S. C. Photoelectrochemical conversion of carbon dioxide (CO2) into fuels and value-added products. *ACS Energy Letters* **2020**, *5* (2), 486-519.

(108) Langer, S. H.; Card, J. C. Electrocatalytic activity of sulfur-modified platinum electrodes: selective electrogenerative oxidation of ethanol to ethyl acetate. *Journal of molecular catalysis* **1987**, *42* (3), 331-336.

(109) Dai, L.; Qin, Q.; Zhao, X.; Xu, C.; Hu, C.; Mo, S.; Wang, Y. O.; Lin, S.; Tang, Z.; Zheng, N. Electrochemical partial reforming of ethanol into ethyl acetate using ultrathin Co3O4 nanosheets as a highly selective anode catalyst. *ACS central science* **2016**, *2* (8), 538-544.

(110) Rodriguez-Gomez, A.; Dorado, F.; de Lucas-Consuegra, A.; de la Osa, A. R. Additional pathways for the ethanol electro-reforming knowledge: The role of the initial concentration on the product yields. *Fuel Processing Technology* **2021**, *222*, 106954.

(111) Kawaguchi, D.; Ogihara, H.; Kurokawa, H. Upgrading of Ethanol to 1, 1-Diethoxyethane by Proton-Exchange Membrane Electrolysis. *ChemSusChem* **2021**, *14* (20), 4431-4438.

(112) Serra, D.; Correia, M. C.; McElwee-White, L. Iron and ruthenium heterobimetallic carbonyl complexes as electrocatalysts for alcohol oxidation: Electrochemical and mechanistic studies. *Organometallics* **2011**, *30* (21), 5568-5577.

(113) Centi, G.; Perathoner, S.; Genovese, C.; Arrigo, R. Advanced (photo) electrocatalytic approaches to substitute the use of fossil fuels in chemical production. *Chemical Communications* **2023**, *59* (21), 3005-3023.

(114) Liu, D.; Huang, H.-Z.; Zhu, Z.; Li, J.; Chen, L.-W.; Jing, X.-T.; Yin, A.-X. Promoting the electrocatalytic ethanol oxidation activity of pt by alloying with cu. *Catalysts* **2022**, *12* (12), 1562.

(115) Zheng, Y.; Wan, X.; Cheng, X.; Cheng, K.; Dai, Z.; Liu, Z. Advanced catalytic materials for ethanol oxidation in direct ethanol fuel cells. *Catalysts* **2020**, *10* (2), 166.

(116) Luo, X.; Fu, C.; Shen, S.; Luo, L.; Zhang, J. Free–templated synthesis of N–doped PtCu porous hollow nanospheres for efficient ethanol oxidation and oxygen reduction reactions. *Applied Catalysis B: Environmental* **2023**, *330*, 122602.

(117) He, Z.; Duan, Q.; Liao, L.; Wang, C. Surface strain-regulated twin-rich Au-Pt bimetallic nanowire for highly efficient alcohol oxidation reaction. *Chemical Engineering Journal* **2023**, *468*, 143411.

(118) Abraham, B. G.; Bhaskaran, R.; Chetty, R. Electrodeposited bimetallic (PtPd, PtRu, PtSn) catalysts on titanium support for methanol oxidation in direct methanol fuel cells. *Journal of the Electrochemical Society* **2020**, *167* (2), 024512.

(119) Han, C.; Liu, Q.; Ivey, D. G. Kinetics of Sn electrodeposition from Sn (II)–citrate solutions. *Electrochimica Acta* **2008**, *53* (28), 8332-8340.

(120) Lide, D. R. Physical constants of organic compounds. *CRC handbook of chemistry and physics* **2005**, *89*, 3-1.

(121) He, A.; Liu, Q.; Ivey, D. G. Electrodeposition of tin: a simple approach. *Journal of Materials Science: Materials in Electronics* **2008**, *19*, 553-562.

(122) Walsh, F. C.; Low, C. T. J. A review of developments in the electrodeposition of tin. *Surface and Coatings Technology* **2016**, *288*, 79-94.

(123) Yang, C.-L.; Wang, L.-N.; Yin, P.; Liu, J.; Chen, M.-X.; Yan, Q.-Q.; Wang, Z.-S.; Xu, S.-L.; Chu, S.-Q.; Cui, C. Sulfur-anchoring synthesis of platinum intermetallic nanoparticle catalysts for fuel cells. *Science* **2021**, *374* (6566), 459-464.

(124) Ramírez, B.; Benito, R.; Torres-Arenas, J.; Benavides, A. Water phase transitions from the perspective of hydrogen-bond network analysis. *Physical Chemistry Chemical Physics* **2018**, *20* (44), 28308-28318.

(125) Gao, Y.; Fang, H.; Ni, K. A hierarchical clustering method of hydrogen bond networks in liquid water undergoing shear flow. *Scientific Reports* **2021**, *11* (1), 9542.

(126) Gao, Y.; Fang, H.; Ni, K.; Feng, Y. Water clusters and density fluctuations in liquid water based on extended hierarchical clustering methods. *Scientific Reports* **2022**, *12* (1), 8036.

(127) Hartnig, C.; Koper, M. T. M. Molecular dynamics simulations of solvent reorganization in electron-transfer reactions. *The Journal of Chemical Physics* **2001**, *115* (18), 8540-8546.

(128) Sun, Q. Local statistical interpretation for water structure. *Chemical Physics Letters* **2013**, *568*, 90-94.

(129) Hutter, J.; Iannuzzi, M.; Schiffmann, F.; VandeVondele, J. cp2k: atomistic simulations of condensed matter systems. *WIREs Computational Molecular Science* **2014**, *4* (1), 15-25,

(130) VandeVondele, J.; Krack, M.; Mohamed, F.; Parrinello, M.; Chassaing, T.; Hutter, J. Quickstep: Fast and accurate density functional calculations using a mixed Gaussian and plane waves approach. *Computer Physics Communications* **2005**, *167* (2), 103-128.

(131) Perdew, J. P.; Burke, K.; Ernzerhof, M. Generalized Gradient Approximation Made Simple. *Physical Review Letters* **1996**, *77* (18), 3865-3868.

(132) Gurdal, Y.; Luber, S.; Hutter, J.; Iannuzzi, M. Non-innocent adsorption of Co-pyrphyrin on rutile(110). *Physical Chemistry Chemical Physics* **2015**, *17* (35), 22846-22854.

(133) Esch, T. R.; Gadaczek, I.; Bredow, T. Surface structures and thermodynamics of low-index of rutile, brookite and anatase – A comparative DFT study. *Applied Surface Science* **2014**, *288*, 275-287.

(134) Goedecker, S.; Teter, M.; Hutter, J. Separable dual-space Gaussian pseudopotentials. *Physical Review B* **1996**, *54* (3), 1703-1710.

(135) Hubbard, J.; Flowers, B. H. Electron correlations in narrow energy bands. *Proceedings of the Royal Society of London. Series A. Mathematical and Physical Sciences* **1997**, *276* (1365), 238-257.

(136) Anisimov, V. I.; Zaanen, J.; Andersen, O. K. Band theory and Mott insulators: Hubbard U instead of Stoner I. *Physical Review B* **1991**, *44* (3), 943-954.

(137) Hu, Z.; Metiu, H. Choice of U for DFT+U Calculations for Titanium Oxides. *The Journal of Physical Chemistry C* **2011**, *115* (13), 5841-5845.

(138) German, E.; Faccio, R.; Mombrú, A. W. A DFT + U study on structural, electronic, vibrational and thermodynamic properties of TiO2 polymorphs and hydrogen titanate: tuning the Hubbard 'U-term'. *Journal of Physics Communications* **2017**, *1* (5), 055006.

(139) VandeVondele, J.; Hutter, J. Gaussian basis sets for accurate calculations on molecular systems in gas and condensed phases. *J Chem Phys* **2007**, *127* (11), 114105.

(140) Grimme, S. Accurate description of van der Waals complexes by density functional theory including empirical corrections. *Journal of Computational Chemistry* **2004**, *25* (12), 1463-1473.

(141) Grimme, S. Semiempirical GGA-type density functional constructed with a long-range dispersion correction. *Journal of Computational Chemistry* **2006**, *27* (15), 1787-1799.

(142) Evans, D. J.; Holian, B. L. The Nose–Hoover thermostat. *The Journal of Chemical Physics* **1985**, *83* (8), 4069-4074.

(143) Verlet, L. Computer" experiments" on classical fluids. I. Thermodynamical properties of Lennard-Jones molecules. *Physical review* **1967**, *159* (1), 98.

(144) Kavan, L.; Grätzel, M.; Gilbert, S. E.; Klemenz, C.; Scheel, H. J. Electrochemical and Photoelectrochemical Investigation of Single-Crystal Anatase. *Journal of the American Chemical Society* **1996**, *118* (28), 6716-6723.

(145) Mo, S.-D.; Ching, W. Y. Electronic and optical properties of three phases of titanium dioxide: Rutile, anatase, and brookite. *Physical Review B* **1995**, *51* (19), 13023-13032.

(146) White, J. A.; Schwegler, E.; Galli, G.; Gygi, F. The solvation of Na+ in water: First-principles simulations. *The Journal of Chemical Physics* **2000**, *113* (11), 4668-4673.

(147) Burdett, J. K.; Hughbanks, T.; Miller, G. J.; Richardson Jr, J. W.; Smith, J. V. Structural-electronic relationships in inorganic solids: powder neutron diffraction studies of the rutile and anatase polymorphs of titanium dioxide at 15 and 295 K. *Journal of the American Chemical Society* **1987**, *109* (12), 3639-3646.

(148) Howard, C.; Sabine, T.; Dickson, F. Structural and thermal parameters for rutile and anatase. *Acta Crystallographica Section B: Structural Science* **1991**, *47* (4), 462-468.

(149) Glassford, K. M.; Chelikowsky, J. R. Structural and electronic properties of titanium dioxide. *Physical Review B* **1992**, *46* (3), 1284.

(150) Liu, X.; Fu, J. Electronic and elastic properties of the tetragonal anatase TiO2 structure from first principle calculation. *Optik* **2020**, *206*, 164342.

(151) Mikami, M. M. M.; Nakamura, S. N. S.; Kitao, O. K. O.; Arakawa, H. A. H.; Gonze, X. G. X. First-principles study of titanium dioxide: rutile and anatase. *Japanese Journal of Applied Physics* **2000**, *39* (8B), L847.

(152) Sanjines, R.; Tang, H.; Berger, H.; Gozzo, F.; Margaritondo, G.; Levy, F. Electronic structure of anatase TiO2 oxide. *Journal of Applied Physics* **1994**, *75* (6), 2945-2951.

ATTENDANCE IN NATIONAL AND INTERNATIONAL CONFERENCES

- **Poster** presentation: **Unravelling the Interaction of Water with Titanium Dioxide by FTIR Spectroscopy, R. Verduci,** G. Centi, S. Perathoner, G. D'Angelo, Materials for Sustainable Development Conference (MAT-SUS), nanoGe Fall Meeting, World Trade Center Barcelona, Barcelona, Spain, 24-28 October 2021.

- **Oral** contribution as **INVITED SPEAKER: The Role of Water at the Interface with TiO$_2$ for H$_2$ Photoproduction, R. Verduci,** F. Creazzo, G. Cassone, F. Tavella, C. Ampelli, S. Luber, S. Perathoner, G. Centi, Giovanna D'Angelo, Photonics and Electromagnetics Research Symposium (PIERS 2023), Prague Congress Center, Prague, Czech Republic, 3-6 July 2023.
- **Oral** contribution**: The Role of Water at the Interface with TiO$_2$ for H$_2$ Photoproduction, R. Verduci,** G. D'Angelo S. Perathoner, G. Centi, 109° Congresso Nazionale della Società Italiana di Fisica (SIF), Dipartimento di Fisica dell'Università di Salerno, Fisciano (Salerno), Italia, 11-15 September 2023.

PUBLICATION LIST

Published

1. **R. Verduci**, A. Agresti, V. Romano, G. D'Angelo, **Interface Engineering for Perovskite Solar Cells Based on 2D-Materials: A Physics Point of View**. *Materials* **2021**, 14, 5843. DOI: https://doi.org/10.3390/ma14195843

2. **R. Verduci**, V. Romano, G. Brunetti, N. Yaghoobi Nia, A. Di Carlo, G. D'Angelo, C. Ciminelli, **Solar energy in space applications: review and technology perspectives**. *Advanced Energy Materials* **2022**, 12, 2200125.
   DOI: https://doi.org/10.1002/aenm. 202200125

3. V. Romano, A. Agresti, **R. Verduci**, G. D'Angelo, **Advances in perovskites for photovoltaic applications in space**. *ACS Energy Letters* **2022**,7,2490-2514.
   DOI: https://doi.org/10.1021/acsenergylett.2c01099

Submitted

R. Verduci, F. Creazzo, J. Sponer, F. Tavella, S. Abate, C. Ampelli, S. Luber, S. Perathoner, G. Cassone, G. Centi, G. D'Angelo, **Structuring of water at the TiO$_2$ interface boosts solar-driven water-splitting performances.**